Excited Hadrons in Two-Flavor Lattice QCD

Dissertation
zur Erlangung des akademischen Grades
Doktor der Naturwissenschaften (Dr. rer. nat.)

Eingereicht von
Georg P. Engel

Angefertigt am Institut für Physik
der Karl-Franzens-Universität Graz

Betreuer und Gutachter
Univ.Prof. Dr. Christian B. Lang

Zweitgutachter
Prof. Dr. Sasa Prelovsek

Mai 2012

Präambel

Ich bestätige, dass es sich bei der hier vorgelegten Dissertation um eine Originalarbeit handelt, die von mir selbstständig angefertigt und abgefasst wurde.

. . . .

(Georg P. Engel)

To Anna

Abstract. The majority of the experimental knowledge about QCD observables is contained in the excited hadron spectrum. The present thesis provides an ab-initio, non-perturbative determination of the excited meson and baryon spectrum, using the lattice regularization of QCD. We use a Hybrid Monte Carlo algorithm to generate seven ensembles with two flavors of dynamical Chirally Improved quarks. The advantages of the improved action lie in small discretization effects and frequent tunneling of topological sectors, reducing autocorrelation. The pion masses are in the range of 250 to 600 MeV, the results are extrapolated to the physical pion mass. Three further ensembles are generated to investigate finite volume effects and to perform the infinite volume limit for specific observables. The strange hadron spectrum is accessed using partial quenching for the strange quark. The variational method is applied to access excited states and also to investigate the content of the physical states. The latter applies in particular to the approximate C-parity of strange mesons, the singlet/octet mixing of Λ baryons and the octet/decuplet mixing of Σ and Ξ baryons. The construction of interpolators is discussed for specific cases. In some baryon channels, Fierz identities force point-like interpolators to vanish exactly. We show that interpolators can be constructed nevertheless and propose two strategies, based on quark smearing and the Rarita-Schwinger condition, respectively. In general, our results compare nicely with experiment, and we even predict some new states and allow for insights concerning the content of the physical states. Part of the work has been published in [1–6], and further publications are in preparation.

Zusammenfassung. Aus dem Experiment wissen wir, dass fast alle Hadronen angeregte Zustände sind. Die vorliegende Dissertation liefert eine ab-initio, nicht-perturbative Bestimmung des angeregten Meson- und Baryonspektrum unter Verwendung der Gitter-Regularisierung von QCD. Mit Hilfe eines Hybrid Monte Carlo Algorithmus werden sieben Ensembles mit zwei dynamischen Chirally Improved Quarks erzeugt. Die Vorteile der verbesserten Wirkung liegen in kleinen Diskretisierungseffekten und häufigem Tunneln der topologischen Sektoren, was eine geringe Autokorrelation zur Folge hat. Die Pionmassen in der vorgelegten Arbeit liegen im Bereich von 250 bis 600 MeV, die Resultate werden zur physikalischen Pionmasse extrapoliert. Drei weitere Ensembles für unterschiedliche Gittergrößen werden erzeugt um Effekte des endlichen Volumens zu untersuchen und um den Limes zu unendlichem Volumen für bestimmte Observablen durchzuführen. Strange Quarks werden durch Partial Quenching eingeführt. Mit Hilfe der sogenannten Variationsmethode studieren wir angeregte Zustände und erforschen den Inhalt der physikalischen Zustände. Insbesondere untersuchen wir die C-Parität von strange Mesonen, das Mischen von Singlet und Oktett in Λ Baryonen und das Mischen von Oktett und Dekuplet in Σ und Ξ Baryonen. Die Konstruktion von Interpolatoren wird explizit für bestimmte Fälle diskutiert. In einigen Baryon Kanälen erzwingen Fierz-Identitäten ein exaktes Verschwinden von punktförmigen Interpolatoren. Wir zeigen, dass dennoch Interpolatoren konstruiert werden können, und schlagen zwei Strategien dafür vor, welche sich auf ausgedehnte Quarkquellen bzw. die Rarita-Schwinger Bedingung stützen. Im Allgemeinen zeigen unsere Resultate gute Übereinstimmung mit dem Experiment. Darüber hinaus können wir auch einige Vorhersagen machen und finden Einblicke in den Inhalt der physikalischen Zustände. Teile der Arbeit wurden in [1–6] publiziert, und weitere Publikationen sind in Vorbereitung.

Contents

List of Figures

List of Tables

Chapter 1

Introduction

The proton is known as a part of the nuclei since 1919, when Rutherford showed that oxygen can be produced by shooting alpha-particles at a target of nitrogen. In the following decades, many further "elementary particles" were discovered, which lead to the so-called "particle zoo" [7]. To understand this extensive list of particles, it was conjectured in 1964 that the proton itself is not an elementary particle, but a bound state of *quarks* [8, 9]. A new force binding the quarks was introduced and called *strong interactions*, with *gluons* being the transmitter of this force. A quantum gauge field theory with three different kinds of charges (*colors*) was suggested in 1973, named *Quantum Chromodynamics* (QCD) [10]. This theory has only very few parameters, can be formulated in a very compact and elegant way, and is expected to predict the proton and the entire hadronic part of the particle zoo.

However, despite the beauty of the theory, one encounters tremendous difficulties when trying to calculate predictions for Nature. An analytic solution is not found so far and hope disappears that it will ever be. The traditional instrument to deal with a quantum field theory, perturbation theory in the coupling, fails to describe the generation of hadrons, the bound states of quarks. The origin of its failure lies in its crucial dependence on small couplings, whereas strong interactions show a strong coupling at the typical scale of hadrons.

There was significant progress in understanding QCD through the development of Chiral Perturbation Theory, which is an expansion in low momenta and small quark masses [11, 12]. It was found that most of the proton mass is generated dynamically through strong interactions. One mechanism of dynamical generation of masses has been known already since 1961 and relies on dynamical symmetry breaking [13, 14]. However, all those approaches do not use quarks and gluons as fundamental degrees of freedom, but start from an effective description which ignores the gauge symmetry of color.

In 1974, the lattice regularization of QCD was introduced by Kenneth G. Wilson [15]. So far, it provides the only known way to perform ab-initio calculations starting from quarks and gluons. Furthermore, it is assumed to provide an interacting constructive quantum field theory in four dimensions with a rigorously valid mathematical foundation. However, any calculation of observables in lattice QCD requires a profound theoretical setup, sophisticated algorithms and extensive computer resources. Concerning the theoretical setup, for example chiral symmetry is an obstacle, since it is broken by the discretization of spacetime explicitely [16]. This causes serious concerns, since it impedes the dynamical breaking of chiral symmetry which contributes significantly to the mass generation of hadrons.

Using renormalization group methods, it was observed in 1981 that a solution might be Dirac operators obeying a non-linear relation, the so-called Ginsparg-Wilson (GW) condition [17]. By now we know several Dirac operators obeying that condition. One of them, the overlap operator [18, 19], has an explicit construction based on a domain-wall approach [20, 21] in the limit of infinite extent of a fifth dimension. Another formulation, the perfect action, is formally exact [22], but can be constructed only approximately [23]. Finally it was found that there exists an exact version of chiral symmetry on the lattice, which, however, is much more complicated than its continuum counterpart [24]. Thus, Dirac operators supporting exact chiral symmetry on the lattice are numerically expensive to construct but they also show nice properties like protection from additive mass renormalization or automatic $\mathcal{O}(a)$ improvement. In general, simulations with dynamical GW-fermions are about two orders of magnitude more expensive than simulations with the simple, improved Wilson fermions.

The so-called Chirally Improved (CI) Dirac operator, used in this work, is an approximate solution of the Ginsparg-Wilson equation [25, 26]. It is constructed by inserting a formal parameterization of the Dirac operator in the GW-equation and solving it after truncation. This fermion action has been investigated and used extensively in simulations by the BGR-collaboration [1–6, 25–48]. It was found that at least in quenched simulations the discretization errors of order $\mathcal{O}(a^2)$ for baryon masses are small [29] and that renormalization constants behave similar to an exact chirally symmetric action [33]. The numerical costs are between the one of improved Wilson and exact GW-actions, which is adequate considering the improved chiral properties.

The present thesis focuses on the excited hadron spectrum obtained from two flavors of dynamical Chirally Improved quarks. The main motivation for this work lies in the fact that most of the experimental knowledge about QCD observables is contained in the excited hadron spectrum. Thus, an ab-initio calculation of them starting only from the QCD Lagrangian is highly desirable. Only in recent years there have been lattice calculations with dynamical quark masses close to their physical values, most calculations still rely on extrapolations from unphysically heavy quarks. A reliable determination of the excited states still remains a hard challenge.

We present results for ground states as well as for excited states of mesons and baryons, making use of the variational method [49, 50]. We generate seven ensembles with pion masses in the range of 250 to 600 MeV. Motivated by leading order Chiral Perturbation Theory, the extrapolation to the physical pion mass is performed using a fit linear in the pion mass squared. In addition to the light (dynamical and valence) quarks we also consider another, heavier valence (strange) quark and include the strange mesons and baryons in our analysis. Whenever accessible, we extract information about the content of states from the variational analysis. This applies for example to the Dirac content, the approximate C-parity of strange mesons, the singlet/octet mixing of Λ baryons and the octet/decuplet mixing of Σ and Ξ baryons. The construction of interpolators is discussed for specific cases. Due to limited computational resources, we do not perform a continuum limit. This may be justified considering the small discretization errors of the used action. Non-negligible finite volume effects are expected in some of our ensembles. These are discussed for specific observables using lattices of different volumes. Part of the work has already been presented in [1–6], and further publications are in preparation.

Recent results on light and strange hadron spectroscopy with focus on excited states following different approaches can be found in [51–71]. Recent proceeding articles related to plenary talks about hadron spectroscopy on the lattice are found in [72, 73].

In continuum quantum field theory there has been recent progress in investigations of the hadron spectrum using truncations of the Schwinger-Dyson equations, the Bethe-Salpeter equation and the Fadeev equation, as well as effective field theories (see for examples Refs. [74–84]).

All results for the hadron spectrum presented in this work refer to the discrete spectrum of the Hamiltonian. Very recently, there is also significant progress in determining properties of resonances in the infinite system from simulations using finite lattices. Corresponding results are found in [85–96]. Methods for determining resonance parameters from finite lattices have been introduced and discussed in [97–107].

Finally, we stress that the present thesis discusses only the implications of the QCD Lagrangian with two light mass-degenerate quarks on a finite lattice. Electroweak dynamics, isospin breaking corrections, further sea quarks and discretization effects are neglected. We discuss finite volume effects for specific observables but we do not determine properties of resonances in the infinite system.

This thesis is organized as follows. We briefly introduce the continuum formulation of QCD in Chapter 2. Some important aspects of the lattice regularization of QCD are reviewed in Chapter 3. Next, the setup of our simulation is detailed in Chapter 4. Chapter 5 briefly discusses the properties of the simulation. The scale and low energy parameters are determined in Chapter 6. The results for the meson and baryon spectrum in finite lattices are presented in Chapters 7 and 8, respectively. Finite volume and other systematic effects are discussed in Chapter 9. Finally, we conclude in Chapter 10. Appendix A includes details about the Chirally Improved Dirac operator. Discussion and tables of meson and baryon interpolators are found in Appendices B and C, respectively. Tables with energy levels and χ^2 of fits are collected in Appendix D.

Chapter 2

QCD in the Continuum

Quantum Chromodynamics (QCD) is the quantum field theory describing the interaction of quarks and gluons [10]. It is very rich in phenomena, asymptotically free, and a number of arguments suggest that it is a strictly confining theory, even though a rigorous proof is yet missing. The interaction is determined by the gauge symmetry principle with the color gauge group SU(3). This means that at each space-time point, there is a local symmetry transformation with eight local parameters, describing rotations in an internal color space.

While the first formulation of a quantum field theory used the canonical quantization of fields, the functional integral representation became popular in recent decades. In this formalism, the fields are represented by numbers, not by operators. Nevertheless, with an abuse of notation, we will use the notion of operator as well, switching between the two pictures occasionally.

In the functional integral, the central object is the partition sum Z, obtained by integrating over all fields with a weight factor given by the action. For QCD, this reads

$$Z = \int \mathcal{D}\big[A_\mu\big]\mathcal{D}\big[\psi\big]\mathcal{D}\big[\bar{\psi}\big]\mathrm{e}^{i\int d^4x \mathcal{L}[A_\mu,\psi,\bar{\psi}]} \ , \tag{2.1}$$

where A_μ is the gauge field, ψ ($\bar{\psi}$) the quark (antiquark) field, and $D[.]$ the integration measure of the respective fields. $\mathcal{L}$ is the QCD Lagrangian density (which will be referred to just as Lagrangian), given by

$$\begin{aligned}
\mathcal{L}[A_\mu,\psi,\bar{\psi}] &= \sum_{f=1}^{N_f} \overline{\psi}^{(f)}(x)\big[i\gamma^\mu D_\mu(x) - m^{(f)}\big]\psi^{(f)}(x) \\
&\quad -\frac{1}{2g^2}\,\mathrm{tr}\big[F^{\mu\nu}(x)F_{\mu\nu}(x)\big] &(2.2)\\
D_\mu(x) &= \partial_\mu - iA_\mu(x) \\
F_{\mu\nu}(x) &= i\big[D_\mu(x), D_\nu(x)\big] \\
&= \partial_\mu A_\nu(x) - \partial_\nu A_\mu(x) + i\big[A_\mu(x), A_\nu(x)\big] \ , &(2.3)
\end{aligned}$$

where f denotes the flavor and matrix/vector notation is used for color and spinor components. γ_μ are the Dirac matrices, $m^{(f)}$ are the quark masses and g is the QCD coupling constant. Since SU(3) is a non-abelian Lie group, the commutator in Eq. (2.3) does not vanish, giving rise to gluonic self-interaction already at tree-level.

In general, the integral Eq. (2.1) is divergent for several reasons. Due to the gauge symmetry, the integral over the fields contains infinitely many gauge copies with the same physical content. This can be overcome by fixing the gauge. However, on a finite lattice with a compact gauge group, the integral over the copies converges. If one is interested in gauge-invariant observables only, one can calculate them on the lattice without fixing the gauge. This path is pursued in the present work.

Further divergencies appear from the quantum fluctuations in interacting quantum field theories. The solution to this problem was found in regularization of the functional integral combined with a renormalization of the parameters of the Lagrangian. The parameters show a scale dependence, a prominent representative of which is the running coupling. In this way, the quantum fluctuations create a scale for the theory, which lies at the heart of the dynamical mass generation of hadrons.

For a long time, perturbation theory was the standard tool to investigate quantum field theories. However, from simple models, it is expected that the mechanism of mass generation is intrinsically non-perturbative. Thus, one needs non-perturbative tools when trying to discuss hadrons using quarks and gluons as elementary degrees of freedom. The lattice is a non-perturbative regulator, which is introduced in the next Chapter.

Finally, we stress that chiral symmetry is an important property of QCD. Many features, like the appearance of Nambu-Goldstone bosons or the mass generation of hadrons, are expected to be strongly related to spontaneous chiral symmetry breaking [13, 14, 108, 109]. In the present work, we use a discretization of the Dirac operator with improved chiral properties. The resulting action is used to investigate the dynamical mass generation of hadrons in various channels.

Chapter 3

QCD on the Lattice

In this chapter, we briefly review the fundamental properties of lattice field theory. In Section 3.1, its first formulation is introduced. Secion 3.2 discusses physics and symmetries on the lattice and finally also the connection to physical observables.

3.1 The Lattice Regulator

The lattice was introduced as a regulator for the ultraviolet divergencies in quantum field theories by Kenneth G. Wilson [15]. Euclidean spacetime is discretized by defining a minimum distance, the lattice spacing a. Consequently, there is a hard momentum cutoff and the Poincaré group is broken to a discrete subgroup. There are further consequences, which will be discussed later. By now, there is a number of excellent books on lattice field theory [110–118].

An important feature of lattice gauge theory is that the construction is such that the gauge symmetry is preserved. This is achieved by putting the quarks on the sites of the lattice, while identifying the gluons with the links connecting these sites (see Figure 3.1). The gluons are group-valued objects and identical to the gauge-transporters, which allow for a construction of spatially extended gauge-invariant terms.

The continuum theory is recovered by taking the continuum limit of the lattice theory. Due to asymptotic freedom of QCD, the continuum limit is obtained by sending the coupling to zero: $g \to 0$. However, the rigorous proof of existence of this limit is still missing.

A senseful lattice gauge action can be obtained by a naïve discretization of the continuum gauge action (see Eq. (2.2)). The resulting Wilson gauge action reads

$$S_G = \frac{\beta}{3} \sum_n \sum_{\mu<\nu} \mathrm{Re}\,\mathrm{tr} \left[\mathbb{1} - U_{\mu\nu}(n) \right] , \tag{3.1}$$

with the inverse coupling $\beta = 6/g^2$, the plaquette

$$U_{\mu\nu}(n) = U_\mu(n) U_\nu(n+\hat{\mu}) U_\mu(n+\hat{\nu})^\dagger U_\nu(n)^\dagger , \tag{3.2}$$

and the gauge fields U, color indices being implicit. $\hat{\mu}$ denotes a vector in μ direction with the length of one lattice unit. The naïve discretization of the fermion action,

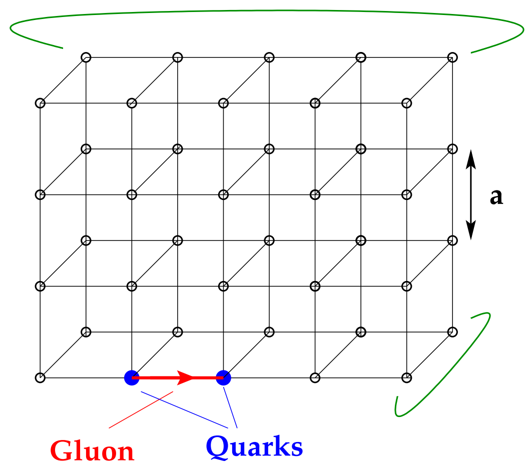

Figure 3.1: The lattice regulator. Quarks sit on the sites, gluons on the links. The green curves represent the closed boundary conditions and a denotes the lattice spacing.

however, runs into the so-called doubling problem. Quantizing a theory with one fermion in four Euclidean dimensions, one ends up with a total of sixteen fermions. This doubling is related to the fermionic dispersion relation and chiral symmetry, expressed in the celebrated No-Go Theorem for regularizing chiral fermions by Nielson and Ninomiya [16]. The doublers can be removed by adding the Wilson-term, which consequently breaks chiral symmetry explicitely. The resulting Wilson fermion action reads

$$S_F = a^4 \sum_{n,m} \sum_{f} \overline{\psi}^{(f)}(n)\, D^{(f)}(n,m)\, \psi^{(f)}(m) \,, \tag{3.3}$$

with the quarks ψ, antiquarks $\overline{\psi}$, and the Wilson Dirac operator

$$D_W^{(f)}(n,m) = \left(m^{(f)} + \frac{4}{a}\right) \delta_{n,m} - \frac{1}{2a} \sum_{\mu=\pm 1}^{\pm 4} \left(1 - \gamma_\mu\right) U_\mu(n)\, \delta_{n+\hat{\mu},m} \,, \tag{3.4}$$

where f denotes the flavor, $\gamma_{-\mu} \equiv -\gamma_\mu$ are Dirac matrices, and color and spinor indices are implicit.

The Wilson action is only one of many possible lattice actions, which are all expected to lie in the same universality class, i.e., to make the same predictions for physical observables as $a \to 0$. Including further terms in the action, it is possible to improve the scaling behavior and to reduce discretization errors. The Symanzik improvement program [119, 120] provides a systematic tool for this goal. Symanzik effective theory is a continuum theory with a parametrization of discretization effects. This parametrization can be influenced by tuning the construction of the lattice operators. In particular, lattice operators can be improved by including higher dimensional terms, with coefficients such that the parametrization of discretization effects in Symanzik effective theory approaches zero. In principle, improvement is possible to arbitrary order. However, experience shows that the additional costs due to improvement are of the same order of magnitude as the savings stemming from simulating at coarser lattices. Therefore, in most cases, one is satisfied with $\mathcal{O}(a)$ improvement, leaving only the smaller $\mathcal{O}(a^2)$ discretization errors. Another reason is that $\mathcal{O}(a^2)$ improvement is rather difficult to achieve in the fermionic sector, since it requires evaluations corresponding to tetraquark operators.

3.2 Physics on the Lattice

In this section, we discuss discretized physics and its connection to continuum physics. Section 3.2.1 investigates chiral symmetry on the lattice, in Section 3.2.2, the issue of Poincaré symmetry is explored. Finally, Sections 3.2.3 and 3.2.4 deal with the relation between lattice physics and continuum phenomenology.

3.2.1 Chiral Symmetry

As already mentioned in Chapter 2, chiral symmetry is a very important property of QCD. Unfortunately, on the lattice, chiral symmetry is intimately connected with the appearance of doublers [16]. In the continuum limit, chiral symmetry is well recovered. Nevertheless, at presence, lattice simulations are performed at lattice spacings far from the continuum limit, where the symmetry is absent.

However, also at finite lattice spacing, an exact chiral symmetry can be established on the lattice, provided the Dirac operator obeys the non-linear Ginsparg-Wilson (GW) equation [17]

$$D\,\gamma_5 + \gamma_5\,D \;=\; a\,D\,\gamma_5\,D\,. \tag{3.5}$$

The corresponding lattice chiral symmetry transformation then reads [24]

$$\psi' = \mathrm{e}^{i\alpha\gamma_5 T_i\left(\mathbb{1}-\frac{a}{2}D\right)}\psi\,, \qquad \overline{\psi}' = \overline{\psi}\mathrm{e}^{i\alpha T_i\left(\mathbb{1}-\frac{a}{2}D\right)\gamma_5}\,, \tag{3.6}$$

with generators T_i and a parameter α. In the continuum limit, this transformation converges to the usual chiral symmetry transformation. Note that the symmetry transformation involves the Dirac operator and therefore is different on different gauge configurations.

Several exact and approximate solutions to Eq. (3.5) have been found. The first ansatz for chiral symmetry on the lattice was to introduce a fifth dimension, such that in the effective theory of the four-dimensional subspace a chiral symmetry appears [20, 21]. In actual simulations this is only an approximate solution, since it becomes exact only in the limit of an infinite extent of the fifth dimension. This limit has been performed analytically, leading to the overlap operator [18, 19], of which an explicit construction is known. Perfect fermions have been introduced using the renormalization group [22]. Formally, they solve the GW equation exactly, but only an approximate version can be constructed explicitely [23]. The Chirally Improved Dirac operator [25] is another approximate solution and will be discussed in detail in Section 4.1.

3.2.2 Poincaré Symmetry

The lattice breaks the Poincaré group to a discrete subgroup with a finite number of irreducible representations (irreps). The discrete translational group nicely converges to its continuum version. In particular, the number of irreducible representations, the Fourier modes, become dense and thus span a continuous space in the limit $a \to 0$.

The discretization of the rotational group SU(2) leads to its subgroup ${}^2O$, which is the universal covering of the octahedral (also called cubic) group O. Most continuum irreducible representations (all spins $J \geq 2$) become reducible when the symmetry is restricted to this subgroup. The resulting irreducible representations and their coupling to the continuum spin states have been worked out [121], given in Table 3.1. These irreducible representations are completely independent of the

Irrep of ${}^2O$	Dim. of irrep	Continuum spin J
A_1	1	0,4...
A_2	1	3,6...
E	2	2,4,5...
T_1	3	1,3,4,5...
T_2	3	2,3,4,5...
G_1	2	$\frac{1}{2}, \frac{7}{2}, \frac{9}{2}, \frac{11}{2} \ldots$
G_2	2	$\frac{5}{2}, \frac{7}{2}, \frac{11}{2} \ldots$
H	4	$\frac{3}{2}, \frac{5}{2}, \frac{7}{2}, \frac{9}{2}, \frac{11}{2} \ldots$

Table 3.1: Irreducible representations (irreps) of the rotational group ${}^2O$ on the lattice, given in the first column. Their dimension and the lowest continuum spin states they couple to are given in the second and third column, respectively.

lattice spacing. Consequently, the continuum irreducible representations (spin) are not recovered in a trivial way as we take $a \to 0$.

However, each spin state has a unique degeneracy pattern of the lattice irreps.

This is obvious from the different dimensionality of the irreps. Following all energy levels of the theory to the continuum limit, there is thus, in principal, a way to uniquely assign a continuum spin to a given lattice state, by analyzing the degeneracy of different lattice irreps. Unfortunately, this procedure does not work in practice. The spectrum of QCD is too rich, and, presently, the statistics of the simulations too weak, to allow for a precise statement about degeneracies of the energy levels. Recently, there is also another, more pragmatic suggestion for spin assignment [122]. One constructs several operators in the same lattice irrep with different spin in the naïve continuum limit. Their different couplings to a considered state, and in particular the continuum limit of these couplings can be interpreted as information about the spin content of the state.

In the present work, we construct only interpolators with a naïve continuum limit of the smallest spin for a given lattice channel. Correspondingly, all results are expected to assign to the smallest continuum spin in each given lattice channel. Nevertheless, contributions from higher spin states cannot be excluded and appear in particular at large lattice spacings.

3.2.3 Observables and Euclidean Correlators

In quantum field theory, many observables are extracted from correlation functions. In the Euclidean formulation (obtained from the Minkowskian theory after Wick-rotation to imaginary time) and at zero temperature, a correlator of two operators $\hat{O}_1,\ \hat{O}_2$, behaves as a sum of exponentials

$$\langle \hat{O}_2(t)\hat{O}_1(0)\rangle = \sum_n \langle 0|\hat{O}_2|n\rangle\langle n|\hat{O}_1|0\rangle \mathrm{e}^{-tE_n}\ , \tag{3.7}$$

which can easily be shown by insertion of a complete set of eigenstates $|n\rangle$ of the Hamiltonian. E_n denote eigenvalues of the Hamiltonian, t denotes Euclidean time. In the functional integral approach, this correlator is given by

$$\langle \hat{O}_2(t)\hat{O}_1(0)\rangle \;=\; \frac{1}{Z}\int \mathcal{D}\big[U\big]\mathcal{D}\big[\bar{\psi},\psi\big]\mathrm{e}^{-S_G[U]}\mathrm{e}^{-S_F[\psi,\bar{\psi},U]}O_2(t)O_1(0)\,, \tag{3.8}$$

where S_G and S_F are the gauge and the fermion action, and the gluon and (anti)quark fields are integrated over. Note that the right hand side of this equation is expressed in a language without operators. Due to the simple Grassmannian calculus, the fermionic integration can be carried out analytically. Consider, for instance, an isovector meson correlator of the simple interpolator $\hat{O} = \overline{d}\Gamma u$, then fermionic integration yields

$$\langle \hat{O}(t)\hat{O}^\dagger(0)\rangle \;=\; \pm\frac{1}{Z}\int \mathcal{D}\big[U\big]\mathrm{e}^{-S_G[U]}[\det(D)]^{n_f}\ \mathrm{tr}\left[D^{-1}(0,t)\Gamma D^{-1}(t,0)\Gamma\right]\ , \tag{3.9}$$

where the sign depends on the choice of Γ, and n_f is the number of mass-degenerate flavors (simulation of non-mass-degenerate dynamical flavors is possible but not considered in this work). This expression can be evaluated numerically on the lattice. The integration over the gauge fields is performed using Monte Carlo methods, where the gauge action and the fermion determinant enter the importance sampling (see Section 4.2). The remaining trace over the quark propagators is calculated on each configuration.

Finally, the energy levels E_n and overlap factors $\langle n|\hat{O}|0\rangle$ are obtained from a fit according to Eq. (3.7). A sophisticated method to extract excited states will be discussed in Section 4.3.5. We stress that since the time t is accessible only in lattice units a, also the energy levels can be extracted only in units of $1/a$ in the first place.

3.2.4 Setting the Scale

In lattice simulations, all observables are dimensionless. Thus, one input observable is needed to set the scale, which then enters all dimensionful predictions from the lattice. In general, the scale is not defined a priori in renormalizable quantum field theories. In pure gauge theory there is a one-to-one mapping of this scale to the only one parameter, the running coupling.

Doing light and strange hadron spectroscopy, under the assumption of isospin symmetry, three parameters enter the simulation: the light quark mass parameter m_l, the strange quark mass parameter m_s and the inverse coupling β. Therefore, three inputs from experiment are needed to make predictions at the physical point.

In general, varying the three parameters, one obtains a three-dimensional hypersurface. The physical point is one point lying in this hypersurface, which can be found by intersecting the hypersurface with a curve. In some cases a much easier procedure is available, given by setting one parameter after the other. This will be discussed in more detail in Sections 4.4.1 and 6.

Chapter 4

Setup of the Simulation

In this chapter, the setup of our simulation is described. In Section 4.1, we discuss the lattice action of choice. Section 4.2 introduces the numerical evaluation of the functional integral using Monte Carlo techniques. Then, in Section 4.3, several common methods of hadron spectrosopy are presented. Finally, Section 4.4 discusses the connection of lattice results to Nature, with emphasis on hadron phenomenology.

4.1 Action

4.1.1 The Improved Gauge Action

As already discussed, discretization effects can be reduced following Symanzik's improvement program [119,120]. In the gauge sector, some constraints on the improved action can be relaxed if only spectral quantities are of interest. This simplifies the construction and reduces computational costs, leading to the Lüscher-Weisz gauge action [123, 124], which is used in all simulations discussed in this thesis,

$$S_G = -\beta_1 \sum_{\mathrm{pl}} \frac{1}{3} \mathrm{Re}\,\mathrm{tr}\, U_{\mathrm{pl}} - \beta_2 \sum_{\mathrm{re}} \frac{1}{3} \mathrm{Re}\,\mathrm{tr}\, U_{\mathrm{re}} - \beta_3 \sum_{\mathrm{tb}} \frac{1}{3} \mathrm{Re}\,\mathrm{tr}\, U_{\mathrm{tb}}\ . \tag{4.1}$$

U_{pl} is the standard plaquette, U_{re} is a planar rectangular (2×1)-plaquette and U_{tb} is a closed loop of length 6 along the edges of a 3-cube, called twisted bent (see Figure 4.1). β_1 is the independent leading gauge coupling. The couplings β_2 and β_3 can be determined from tadpole-improved perturbation theory [125]. Using

$$u_0 = \left(\frac{1}{3} \mathrm{Re}\,\mathrm{Tr}\, \langle U_{\mathrm{pl}} \rangle \right)^{1/4} \quad , \quad \alpha = -\frac{1}{3.06839} \log u_0^4\ , \tag{4.2}$$

one obtains

$$\beta_2 = \frac{\beta_1}{20 u_0^2} (1 + 0.4805\, \alpha)\ , \quad \beta_3 = \frac{\beta_1}{u_0^2}\, 0.03325\, \alpha\ . \tag{4.3}$$

In principle, u_0 is a function of the expectation value of the plaquette, and thus the parameters β_2 and β_3 themselves are expectation values of the simulation. This requires a self-consistent calculation of these couplings. In practice one makes an

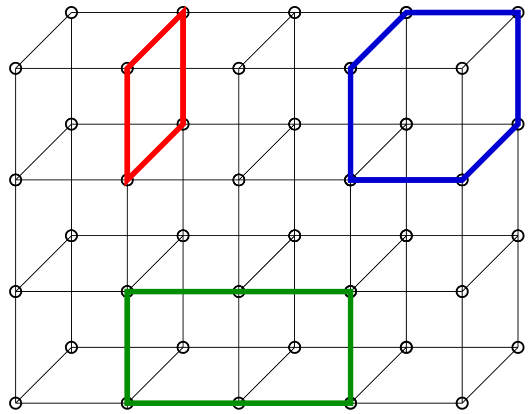

Figure 4.1: The three kinds of Wilson loops entering the Lüscher-Weisz gauge action. Red: plaquette; green: rectangular; blue: twisted bent.

educated guess for the assumed plaquette u_0, which is compared with the expectation value in the end. Deviations from the guess mean non-optimum improvement. In all our simulations, we observed only small deviations, and we kept the assumed plaquette constant along the Monte Carlo timeseries for each generated ensemble.

4.1.2 The Chirally Improved Dirac Operator

The Chirally Improved Dirac (D_{CI}) operator [25, 26] is an approximate solution to the Ginsparg-Wilson (GW) equation [17]. The most simple discretization of the covariant derivative (which enters the Dirac operator) is given by

$$\frac{1}{2}\Big[(U_\mu(n)\delta_{n+\hat{\mu},m} - U_\mu(n-\hat{\mu})^{-1}\delta_{n-\hat{\mu},m}\Big] \ . \tag{4.4}$$

However, respecting all symmetries, one can add many further terms, which may improve the action when the coefficients are chosen properly. Following this idea, one starts with the most general ansatz for a Dirac operator,

$$D_{nm} = \sum_{\alpha=1}^{16} \Gamma_\alpha \sum_{p\in\mathcal{P}^\alpha_{m,n}} c^\alpha_p \prod_{l\in p} U_l \, \delta_{n,m+p} \ , \tag{4.5}$$

where for each element of the Clifford algebra Γ_α, p is a path connecting the points n, m. $\mathcal{P}^\alpha_{m,n}$ is the set of all considered paths p, and c^α_p are coefficients. This ansatz is plugged into the GW equation

$$D\,\gamma_5 + \gamma_5\,D = a\,D\,\gamma_5\,D \ .$$

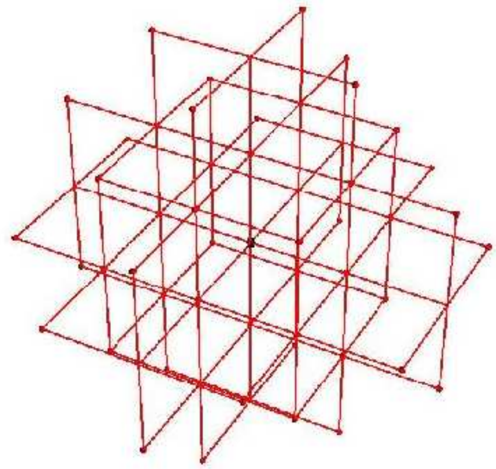

Figure 4.2: The paths (connected to the center site) entering the Chirally Improved Dirac operator. We choose a trunctation to maximum path lengths of four lattice units. The coefficients to the paths are found in Appendix A. (Figure take from [1].)

Since this is an quadratic equation, comparison of the coefficients leads to an algebraic set of coupled equations. Restrictions for the coefficients come from the lattice symmetries and γ_5-hermiticity. In principle, exact chiral symmetry is achievable if one takes into account all possible terms. In practice, the system in truncated, and the equations can be solved numerically. The quality of chiral improvement of course depends on the chosen truncation. We limit ourselves to a maximum path length of four lattice units. The paths and coefficients used are found in Appendix A and depicted schematically in Figure 4.2.

In principle, the coefficients in the parametrization could be optimized for each gauge coupling and quark mass value with respect to chiral symmetry. However, defining the setup this way, the predictive power of the simulation is weakened, and, furthermore, complications arise when different sets of gauge ensembles are compared. Therefore, we decided to use the same paths and coefficients in all our dynamical runs, which means that the bare Dirac operator is the same in all discussed ensembles. Cleary, the drawback of this strategy is weaker chiral improvement. This is for example observed in the appearance of additive mass renormalization. To be able to make a statement about quark masses though, we determine the PCAC (partially conserved axial current) mass, also called AWI (axial Ward identity) mass for each ensemble.

Link smearing (to be discussed in Section 4.3.1) is a well-known simple technique to improve the action. We define our Dirac operator as product of one level of stout smearing [126] with the truncated sum of Eq. (4.5). This operator product thus includes some further paths which are not part of the bare D_{CI}.

4.2 Monte Carlo Integration of the Functional Integral

In this section we discuss the numerical integration of the gauge fields using Monte Carlo techniques. First, the general ideas are introduced in Section 4.2.1. Next, we discuss the issue of generating gauge configurations for dynamical QCD in Section 4.2.2. Finally, numerical improvements are considered in Section 4.2.3.

4.2.1 Generating Gauge Configurations

In continuum quantum field theory one encounters a very high-dimensional functional integral. The measure of the fields is non-vanishing only for very rough fields. To be specific, only continuous non-differentiable fields contribute to the integral. On the other hand, all those rough configurations have infinite action, which means a vanishing Boltzmann factor. This is a typical case of entropy and action drawing in opposite directions. What looks weird at first sight (and indeed complicates a rigorous construction of the integral), becomes more clear from the point of view of Lebesgue's integral.

When defining the action as part of the measure, $\mathcal{D}'[.] = \mathcal{D}[.]\mathrm{e}^{-S[.]}$, one obtains a meaningful measure for classes of field configurations, at least on a finite lattice. This point of view naturally leads to the concept of importance sampling. The weight factor of the configurations, e^{-S}, is not treated at the level of observables, but rather already in the process of generating the field configurations. Among others, this is one reason why Monte Carlo methods are very efficient for high-dimensional integrals such as the functional integral.

Pure SU(N) gauge theory can be simulated with standard Monte Carlo techniques, such as heat bath [127] or overrelaxation [128, 129]. Including dynamical fermions, however, complicates the simulation significantly. The most primitive ansatz, considering the fermion determinant as an observable, does not respect the idea of importance sampling well enough. The weight factors of the quenched and the dynamical theory differ significantly, and hence the important configurations of pure gauge theory differ too much from the important dynamical configurations. Therefore this approach needs very high statistics and is not pursued in practice. Including the fermion determinant as a weight factor in importance sampling, it has to be real and non-negative. γ_5-hermiticity (obeyed by D_{CI}) forces the determinant to be real. When taking an even number of mass-degenerate fermions (n_f=2 in this thesis), $[\det D]^2$ is non-negative and thus ensures a valid probability weight.

This leaves the problem of numerical evaluation of the determinant squared. In the functional integral, fermions are represented by Grassmann numbers. Their anti-commutation property makes them extremely inappropriate for numerical simulations. This problem can be overcome by the analogy of fermionic and bosonic Gaussian integrals. The fermion determinant can be rewritten as a Gaussian integral of pseudofermions with the inverse Dirac operator [130]. These pseudofermions have the same spin quantum numbers as the physical fermions, but obey Bose-Einstein statistics. Due to the spin-statistics theorem they therefore cannot have any physical meaning, they only serve as a numerical technique.

Since the inverse Dirac operator is a highly non-local operator, simple local update propositions are computationally expensive, as they require to calculate the global change of the action. Simple global updates, on the other hand, lead to large changes in the action and thus to a bad Metropolis acceptance rate. Hence, conventional Monte Carlo techniques show a weak performance for generating gauge configurations with dynamical quarks.

4.2.2 The Hybrid Monte Carlo Algorithm

The state-of-the-art method for full QCD on the lattice is the Hybrid Monte Carlo algorithm (HMC) [131]. The central idea is to use the action to make a sophisticated global update proposition, which causes only a small change of the Boltzmann factor. In fact, one would like to have a Boltzmann factor which is constant along the update trajectory up to numerical deviations. Exactly such a kind of property is held by a constant of motion in classical Hamiltonian evolution.

Consider a classical Hamiltonian H, given by a sum of a kinetic and a potential term,

$$H[q,p] = V[q] + \frac{1}{2}p^2 \ , \tag{4.6}$$

where p is the canonical momentum to q, and the potential V is independent of p. Then the classical equations of motion read

$$\dot{p} = -\frac{\partial H}{\partial q} = -\frac{\partial V}{\partial q} \tag{4.7}$$

$$\dot{q} = \frac{\partial H}{\partial p} = p \ . \tag{4.8}$$

The Hamiltonian is itself a constant of motion along the evolution, which is often called molecular dynamics trajectory.

Let us now use this property for QCD simulations [131, 132]. As already discussed, we rewrite the fermion determinant using pseudofermions ϕ. For two mass-degenerate flavors of quarks, the total action S then reads

$$S[U,\phi] = S_G[U] - \phi^\dagger (DD^\dagger)^{-1} \phi \ , \tag{4.9}$$

where $D = D[U]$ is the Dirac operator. ϕ can be easily updated using a Gaussian distributed χ and $\phi = D\chi$.

When augmenting the functional integral with a decoupling Gaussian integral of dummy variables $P \in \mathtt{su}(3)$, observables can be written as

$$\langle O \rangle_U = \frac{\int \mathcal{D}[U,\phi] \mathrm{e}^{-S[U,\phi]} O[U]}{\int \mathcal{D}[U,\phi] \mathrm{e}^{-S[U,\phi]}} \tag{4.10}$$

$$= \frac{\int \mathcal{D}[U,\phi,P] \mathrm{e}^{-S[U,\phi]-\frac{1}{2}\mathrm{tr}[P^2]} O[U]}{\int \mathcal{D}[U,\phi,P] \mathrm{e}^{-S[U,\phi]-\frac{1}{2}\mathrm{tr}[P^2]}} \tag{4.11}$$

$$= \langle O \rangle_{U,P} \tag{4.12}$$

Now we interpret the total action S as the potential term and P as the canonical momentum to the gauge field U. If we then pursue the classical evolution in a fictitious Monte Carlo time according to the Hamiltonian

$$H = S[U,\phi] + \frac{1}{2}\mathrm{tr}[P^2] \ , \tag{4.13}$$

H is a constant of motion and at the same time the Boltzmann factor which determines the acceptance probability in the Metropolis step. Thus, an exact integration of the Hamiltonian evolution would yield an acceptance rate of 100%. The deviations due to the inexact numerical integration of the molecular dynamics trajectory are compensated for in the Metropolis step, decreasing the accceptance rate.

Considering the principal requirements for an algorithm to ensure a generation of ensembles which are representative for the measure of the integral, one finds that the HMC algorithm is reversible and preserves the integration measure. Ergodicity can be proved for sufficiently small trajectory lengths τ. Thus, ergodicity can be ensured by choosing $\tau \in [0, \tau_{max}]$ randomly for each trajectory [133]. In practice, however, one usually considers fixed τ, as ergodicity is expected to hold also for large τ even if this cannot be proven. The technicalities of using the HMC algorithm together with the Chirally Improved Dirac operator are discribed in [37].

Autocorrelation is a delicate issue in Markov chains. Only astronomically large upper bounds for the exponential autocorrelation time can be proven rigorously. Autocorrelation should thus be investigated a posteriori having the data at hand, however, in QCD in most cases the Monte Carlo time series available are not long enough to allow for such an analysis. In particular approaching the continuum limit, observables related to topology are known to cause a severe critical slowing down [134]. Furthermore, the HMC algorithm was found to be non-renormalizable, which complicates the analysis of its scaling behavior towards the continuum limit [135]. Suggestions for improving the algorithm in several respects are discussed in the following section.

4.2.3 Numerical Improvements for the HMC Algorithm

A prominent improvement of performance is achieved with the domain-decomposition HMC [136]. The idea is to have the ultraviolet modes frozen most of the time, updating only the "active links". Another recent proposal makes use of field transformations, with the aim of solving the long standing problem of critical slowing down in the continuum limit [137]. Unfortunately, at least the leading order of the field transformation does not suffice for this goal [138]. Yet another suggestion is to use open boundary conditions to circumvent topological barriers [139].

Many further improvements have been proposed, and most of them work well for simple actions, like Wilson improved. Since the Chirally Improved Dirac operator is built from paths up to a length of four, we have to restrict ourselves to techniques which are almost independent of the form of the Dirac operator.

We use Hasenbusch mass preconditioning [140], where the pseudofermion action is split into several parts by introducing n_p species of pseudofermions. This way the small and the large eigenvalues of the Dirac operator can be separated. We use $n_p = 2$ in all simulations. Furthermore, we make use of the chronological inverter by minimal residue [141] and a mixed-precision inverter [142] for the Dirac operator. Some of the ensembles have been generated using a higher order Omelyan integrator [143] and a multiple timescale integration [144, 145].

Still, numerical problems arise when the determinant is close to zero, which leads to the so-called exceptional configurations. Non-physical large quark masses or fine lattice spacings are ways to avoid this problem. Another possibility is to use a chiral Dirac operator, obeying the Ginsparg-Wilson equation exactly. This restricts its eigenvalues to the Ginsparg-Wilson circle and impedes fluctuations close to zero. The chiral improvement is thus one of the reasons why we can go down to pion masses of 250 MeV at comparably rough lattices ($a \approx 0.13\,\mathrm{fm}$).

4.3 Methods in Hadron Spectroscopy

In this section we introduce common methods in hadron spectroscopy. Link smearing is discussed in Sections 4.3.1, quark smearing in Section 4.3.2. Interpolator construction is detailed in Section 4.3.4. Finally, methods to extract excited states are discussed in Section 4.3.5.

4.3.1 Link Smearing

On the lattice, gauge covariant construction of non-local objects, e.g., the discretized derivative operator, is done using the link variables as gauge transporters. As already discussed in Section 4.1.2, taking the shortest path is not the only possibility to produce gauge covariant objects. One can take a sum over all possible paths between given sites with suitable coefficients, as long as the relevant symmetries are respected. The application of link smearing is equivalent to the inclusion of further paths. From this point of view, the idea of link smearing is similar to the one of Symanzik's improvement program [119, 120], easier to implement, but less systematic.

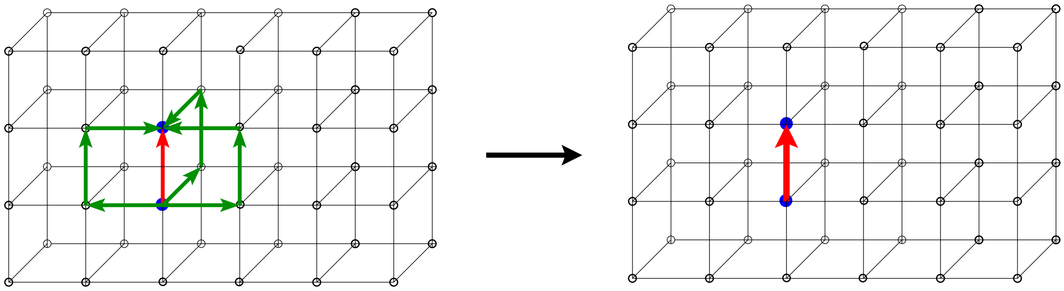

Figure 4.3: The concept of link smearing. The "fat" link (red path, rhs), is a weighted average of the "thin" link (red path, lhs) and the staples (green and further paths).

The link smear operator maps the gauge field to the smeared gauge field (see Figure 4.3). All links are averaged with their neighboring links in a particular way. The original ones are called "thin", the smeared ones "fat" links. The link smear operator is combined with other operators to improve their properties. One application is to build the action with fat links to reduce its discretization effects. Another application arises when one is interested only in observables which are dominated by infrared physics, such as hadron masses. Constructing hadron interpolators with fat links leads to a reduction of ultraviolet fluctuations, but does not affect the exponential long range behavior. This can improve the signal-to-noise ratio considerably.

Several smearing recipes have been constructed, all of them average the thin link $U_\mu(n)$ with its staple

$$S_\mu(n) = \sum_{\nu \neq \pm\mu} U_\nu(n)\, U_\mu(n+\hat{\nu})\, U_\nu(n+\hat{\mu})^\dagger \,. \tag{4.14}$$

Now we briefly introduce the smearing recipes used in this work, denoting the fat link as V_μ:

APE Smearing

The APE procedure was the first formulated smearing technique [146]:

$$V_\mu(n) = P_{\mathrm{SU}(3)} \Big[(1-\alpha) U_\mu(n) + \frac{\alpha}{6} S_\mu(n) \Big] \,, \tag{4.15}$$

with one weighting parameter α. In general, the sum of several Lie group elements is itself not an element of the Lie group. Thus a gauge covariant projection back to the group SU(3) is needed, given by

$$P_{\mathrm{SU}(3)} : A \to B = \max_{B \in \mathrm{SU}(3)} \mathrm{Re}\ \mathrm{tr}\ (BA^\dagger) \,. \tag{4.16}$$

Stout Smearing

Stout smearing uses the projector to the Lie algebra [126]:

$$V_\mu(n) = \mathrm{e}^{\alpha P_{\mathtt{su}(3)}[S_\mu(n)U_\mu(n)^\dagger]}U_\mu(n) \tag{4.17}$$

$$P_{\mathtt{su}(3)}[M] = \frac{1}{2}(M-M^\dagger) - \frac{1}{6}\mathbb{1}\mathrm{tr}(M-M^\dagger)\ . \tag{4.18}$$

The crucial property of this procedure is that differentiability of the fat link V_μ is preserved. This allows the use of stout smearing as part of the Dirac operator in the HMC algorithm.

HYP Smearing

HYP smearing was originally formulated as a recipe which extends the concept of APE to the hypercube to improve locality properties of the operator [147]. This is done in three steps:

$$\begin{aligned}
\bar{U}_{\mu,\nu\sigma}(n) &= P_{\mathrm{SU}(3)}\Big[(1-\alpha_3)U_\mu(n) + \frac{\alpha_3}{2}\sum_{\rho\neq\pm(\mu,\nu,\sigma)} S_\rho(n)\Big] \\
\tilde{U}_{\mu,\nu}(n) &= P_{\mathrm{SU}(3)}\Big[(1-\alpha_2)U_\mu(n) + \frac{\alpha_2}{4}\sum_{\sigma\neq\pm(\mu,\nu)} \bar{S}_\sigma(n)\Big] \\
V_\mu(n) &= P_{\mathrm{SU}(3)}\Big[(1-\alpha_1)U_\mu(n) + \frac{\alpha_1}{6}\sum_{\nu\neq\pm\mu} \tilde{S}_\nu(n)\Big]\ ,
\end{aligned} \tag{4.19}$$

where $\bar{S}$ is the staple built from $\bar{U}$, and $\tilde{S}$ from $\tilde{U}$.

Extensions, further recipes and discussion of smearing are found in [148–154]. As already mentioned in Section 4.1.2, we include one level of stout smearing in the definition of the Dirac operator to improve the action. The parameter of stout smearing is adjusted such that the expectation value of the plaquette is maximized, yielding $\alpha = 0.165$ [126]. The use of smearing in the construction of interpolators will be discussed in Section 4.3.4.

4.3.2 Quark Smearing

Hadron correlation functions include traces of quark propagators D^{-1} (see, e.g., Eq. (3.9)). So far, on realistic lattice sizes, the full inverse Dirac operator is too huge for actual numerics. Thus, in actual calculations, the Dirac operator is inverted on particular quark sources. Point sources are a possible choice, but it was found that extended quark sources improve the signal and also allow for a larger operator basis in the variational method. In each ensemble, we use three different kinds of sources: narrow, wide and a (P-wave like) derivative source. In the following, we describe the method of choice in detail and afterwards briefly introduce alternative methods.

Jacobi Smearing

Gauge covariant sources can be constructed using Jacobi smearing [155, 156]. A point-like source is smeared out by applying a polynomial of the hopping term in the spatial directions,

$$\begin{aligned} S_{\kappa,K} &= \sum_{k=0}^{K} \kappa^k H^k S_0 \,, \\ H(n,m) &= \sum_{i=\pm 1}^{\pm 3} U_i(n)\delta(n+\hat{\imath},m) \,, \end{aligned} \tag{4.20}$$

where S_0 denotes the point source. The parameters κ and K are tuned for each ensemble such that the resulting source shape is approximately Gaussian. Narrow (wide) sources will be denoted by quark subscripts n (w) in the remainder of this work.

The derivative sources, S_{∂_i}, are obtained by applying the covariant difference operators on the wide source, S_w [40],

$$\begin{aligned} P_i(n,m) &= U_i(n)\delta(n+\hat{\imath},m) - U_i(n-\hat{\imath})^\dagger \delta(n-\hat{\imath},m) \\ S_{\partial_i} &= P_i S_w \,, \end{aligned} \tag{4.21}$$

where $\hat{\imath}$ is one of the spatial directions. In the following, derivative sources are indicated by the subscript ∂_i of the quark field.

Stochastic All-to-all Methods

There are other approaches to calculate an expression for the quark propagators. The conventional Jacobi smearing is not convenient for the evaluation of, e.g., disconnected diagrams, which unavoidably appear in the isoscalar channels and in transition processes with altering quark number. All-to-all methods seem to be necessary for this task. As already mentioned, a complete inversion of the Dirac operator overcharges our capacities. Hence, stochastic estimators have been developed to solve this problem [157]. The central idea is to approximate the unity operator by an ensemble of noise vectors. This can be used to approximate the all-to-all quark propagator in the limit of infinitely many noise vectors,

$$D^{-1}(n,m)^{i,j}_{\alpha,\beta} = \lim_{N\to\infty} \sum_{r=1}^{N} \psi_r^{i,\alpha}(n) \eta_r^{j,\beta}(m)^\dagger \,. \tag{4.22}$$

Here η_r are the noise vectors to start with and the ψ_r fulfill $D\psi_r = \eta_r$. The additional noise for the inversion can always be chosen to be less than the noise of the Monte Carlo integration. The method can be improved using dilution of the noise vectors and exact treatment of the low-lying modes of the Dirac operator.

Distillation

The distillation method makes use of the observation that only the lowest modes of the three dimensional covariant lattice Laplace operator ∇^2 contribute significantly to Gaussian shaped sources [158]. This is obvious when using a definition of the quark smear operator which satisfies (the chosen sign convention differs from [158])

$$S_{\sigma,n_\sigma}(t) = \left(1 - \frac{\sigma\nabla^2(t)}{n_\sigma}\right)^{n_\sigma} \xrightarrow{n_\sigma\to\infty} \mathrm{e}^{-\sigma\nabla^2(t)} \ . \tag{4.23}$$

The exponential suppression can be replaced by a projection to the lowest modes. This projector is the distillation operator

$$\Box(t) = V(t)V^\dagger(t) \ , \tag{4.24}$$

where $V(t)$ is the rectangular matrix of the lowest eigenmodes of the Laplacian. The distillation operator is used to build quark sources. Next the Dirac operator is inverted on those sources and afterwards projected to the lowest eigenmodes, which yields the "perambulators"

$$\tau_{\alpha,\beta}(t',t) = V^\dagger(t')D^{-1}_{\alpha,\beta}(t',t)V(t) \ . \tag{4.25}$$

The crucial advantage of distillation is that it allows to concentrate on the low modes of the theory, and simultaneously to benefit from properties typical for exact all-to-all methods:

- The whole timeslice contributes. This improves statistics and allows for a momentum projection at the sources. Furthermore, evaluation of disconnected diagrams becomes fairly efficient.

- Factorization allows to compute the perambulators as propagators and to choose the particular form of the interpolators in the end.

- The factorization also allows to construct sequential propagators by gluing perambulators, and thus simplifies the calculation of three-point functions.

The main drawback of the method is that the number of eigenmodes needed grows linearly with the spatial volume in lattice points. This problem can be overcome with the introduction of stochastic estimator techniques in the subspace of the lowest modes [71, 159]. Another generalization of the algorithm is to include a function of the eigenvalue of the Laplacian in the distillation operator. This can be chosen to force a weighting inside the subspace in favor of the very low modes. Another drawback of the method is that many inversions have to be computed and stored, which demands lots of computer time and disk space.

4.3.3 Inverting the Dirac Operator

Briefly, we want to mention how the Dirac operator is inverted on the prepared sources. The inversion is performed iteratively, by solving

$$G = D^{-1}S\,, \quad DG = S\,, \tag{4.26}$$

for G, where S is the given quark source. Many tools have been developed for this task, like versions of the conjugate gradient [160, 161] or the deflation algorithm [162, 163].

4.3.4 Interpolator Construction

As discussed in Section 3.2.3, observables are extracted from correlation functions of operators. The operators which create hadronic states from the vacuum are called *interpolators*. The quark sources are combined with elements of the Clifford algebra to construct gauge invariant interpolators with definite quantum numbers. In each channel, we construct several interpolators in order to be able to extract excited states using the variational method (to be introduced in Section 4.3.5). Clearly, the interpolators should show good overlap with the low-lying physical states. One popular technique to reduce contamination of ultraviolet modes is given by link and quark smearing, introduced in Sections 4.3.1 and 4.3.2.

Throughout all simulations discussed in this thesis, one level of stout and three levels of spatial HYP smearing are applied. Several levels of HYP smearing have been investigated, where it was found that most observables show the best signal in case of three levels. The parameters of stout smearing are chosen the same way as in the case of the Dirac operator. The parameters of the spatial HYP smearing have been varied, monitoring the minimum and the average value of the plaquette, partly following arguments of [147, 151]. The maximum values of these observables are not located at the same choice of parameter. We decided to choose the parameters in between, such that both the average and the minimum plaquette are close to maximum. This results in $\alpha_1 = 0.8$ and $\alpha_2 = 0.4$, where α_1 is the parameter in the last step of the smearing procedure, where the center link is smeared.

These fat links are then used to perform quark smearing, creating the sources. We shift the center positions of the quark sources for subsequent configurations in order to decrease statistical correlation of the data. Finally, the interpolators at the sink are projected to zero momentum. For sufficiently many configurations, translational invariance is restored and only zero momentum states contribute to the hadron correlation functions. We compute connected diagrams only, and therefore focus on isovector mesons, strange mesons, and baryons in this work. The issue of many-particle states will be discussed in Section 4.4.2. We list all used interpolators in Appendices B and C.

Meson Interpolators

Concerning mesons, this work focuses on isovector and strange mesons, since the used method is suited for connected diagrams only. Some few isoscalars will be discussed, with the systematic error of neglecting disconnected diagrams. A general bilinear meson interpolator can be written as

$$O_M = \lambda_{ab}\, \overline{q}_a\, S^{(1)\dagger}\, \Gamma_i\, S^{(2)}\, q_b\ . \tag{4.27}$$

The implicit sum builds irreducible representations of the gauge symmetry, of flavor symmetry and of Lorentz symmetry using the Clebsch-Gordan coefficients λ_{ab}. Γ_i are possible Dirac matrices and q, $\bar{q}$ denote Grassmann numbers representing quarks. The quarks can have particular distribution functions, induced by the smearing operators S, which may include any number of derivatives. We now discuss the construction of meson interpolators to ensure good quantum numbers I, S and J^{PC}.

Isospin and strangeness are determined through the symmetrization of the flavors and the chosen quark mass in the Dirac operator.

Spin and parity are determined by the choice of the Dirac matrix and the spatial distribution of the quarks. Using spatially isotropic sources, such as the Gaussian ones without displacement, the quantum numbers of meson interpolators are completely determined by their Dirac matrix. In the continuum, this restricts them to a few (non-exotic) channels of spin 0 and 1. Recall that the discretization leads to a finite number of irreducible representations of the Lorentz group, as discussed in Section 3.2.2. Therefore, on the lattice, spatially isotropic sources restrict mesons to the channels A_1 and T_1. In principle, these irreps couple to higher spins in the continuum limit as well (see Table 3.1). However, the naïve continuum limit of spatially isotropic interpolators remains restricted to spin 0 and 1. This strongly influences the overlap of the interpolator with the physical states, such that coupling to other (higher) spin states is suppressed at small lattice spacings.

To access higher spin states, and to enlarge the basis of operators, we consider the direct product of spinor and spatial structure in the language of group theory. The decomposition to the irreducible representations then leads to interpolators with definite quantum numbers [122, 164–167]. We realize a non-trivial spatial structure by using the derivative sources, which transform according to the lattice irreducible representation T_1. The only non-trivial resulting decomposition in the continuum and on the lattice looks (at zero momentum):

$$\begin{aligned}
\text{continuum:} \quad & 1 \otimes 1 &&= 0 \oplus 1 \oplus 2 && \qquad (4.28)\\
\text{lattice:} \quad & \mathrm{T}_1 \otimes \mathrm{T}_1 &&= \mathrm{A}_1 \oplus \mathrm{T}_1 \oplus \mathrm{T}_2 \oplus \mathrm{E}\ , && \qquad (4.29)\\
\text{where} \quad & 2 &&= \mathrm{T}_2 \oplus \mathrm{E} \quad \text{in the continuum limit.} && \qquad (4.30)
\end{aligned}$$

For the investigation of physical spin 2 states, we thus can construct T_2 as well as E interpolators on the lattice. Furthermore, we are able to investigate exotic channels (however, the signals are found to be very weak in most cases).

In general, C-parity is a good quantum number only for chargeless states, which applies, e.g., to the $I_z = 0$ components of isovector mesons. However, in the case of exact flavor symmetry, each multiplet shares only a single correlation function. This degeneracy is a consequence of the symmetry and related to a cancelation of disconnected diagrams. Accordingly, C-parity can be effectively assigned to the entire multiplet, and in case of exact SU(3) flavor symmetry even to strange mesons. Breaking SU(3) flavor symmetry towards the physical point, C-parity remains an approximate symmetry for strange mesons. The associated quantum numbers are not restored and states are allowed to mix different C-parity. We discuss the C-parity content of the strange mesons and the mixing towards the physical point for several channels. For this purpose, the interpolators have to be constructed such to respect C-parity in the limit of exact flavor symmetry. In general, this requires a symmetrization with respect to the quark smearing. The necessity depends on the chosen order of the derivative operator and Jacobi smearing in the construction of the derivative sources. The derivation is carried out in Appendix B.1. The meson interpolators are listed in Appendix B.2, indicating also the effective C-parity.

Another approach to realize non-isotropic interpolators is given by the use of displaced quark sources [166]. Leaving the constraint of bilinearity allows for tetraquark operators, which are discussed for example in [168].

Baryon Interpolators

A general 3-quark baryon interpolator can be written as

$$O_B = \lambda_{abc}\,\Gamma_1\,S^{(1)}\,q_a\left[(S^{(2)}\,q_b)^T\,\Gamma_2\,S^{(3)}\,q_c\right], \tag{4.31}$$

where the implicit sum takes care for color antisymmetrization, flavor symmetrization and Lorentz symmetrization with the Clebsch-Gordan coefficients λ_{abc}. In contrast to mesons, each interpolators has now two Dirac matrices (Γ_1, Γ_2). Again, q are Grassmann numbers representing quark fields and S are smearing operators. For the construction of baryon interpolators we use only Gaussian smeared quark sources (n, w). We now discuss the construction of baryon interpolators to ensure good quantum numbers I, S and J^P.

As for mesons, isospin and strangeness are determined through the symmetrization of the flavors and the chosen quark mass in the Dirac operator. We consider the nucleon in the octet, Δ and Ω in the decuplet representation. In case of Λ, we take into account singlet and octet representations. In case of Σ and Ξ, we consider octet and decuplet representations.

The Lorentz quantum numbers spin and parity are completely determined by the chosen Dirac matrices and the spin of the quarks, due to the isotropic sources. We construct interpolators which transform according to the lattice irreducible representations G_1 and H, with the naïve continuum limits of spin 1/2 and 3/2, respectively.

Definite parity is obtained using the parity projection operator. Spin 3/2 is obtained using the Rarita-Schwinger projector. For details, see Appendix C.1.

Since a baryon is built from three valence quarks, there are $2^3 = 8$ possible smearing combinations. In case of exact flavor symmetry, Fierz identities can yield relations among them. In the spin 1/2 channels of the nucleon, Λ (singlet and octet), Σ and Ξ (octet and decuplet) we use three different Dirac structures. In the spin 1/2 channels of Δ and Ω, an open Lorentz index is summed at the level of the interpolators. In case of all spin 3/2 interpolators, the open Lorentz index (after spin projection) is summed after taking the expectation value of correlation functions. All our baryon interpolators are listed in Appendix C.2. Partly, the construction of interpolators follows previous work with the Chirally Improved Dirac operator in quenched QCD [35]. Partly, the construction follows [169, 170]. The construction of further interpolators is discussed in the following. Other approaches to baryon interpolator construction, using derivative operators or displacements can be found, e.g., in [166].

Sidestepping the Fierz Identities

Considering point-like operators, the number of independent interpolators for a given channel is restricted by the Pauli principle (see, e.g., [171]). The corresponding Fierz-transformations can be used to show that some interpolators are linearly dependent, and some even vanish exactly [169, 170]. In particular, there are no non-vanishing point-like interpolators in the Δ spin 1/2 and Λ singlet 3/2 channels, according to reference [169].

In the present work, we propose two strategies to construct interpolators nevertheless. First, note that the Fierz identities also hold for extended isotropic interpolators, as long as all involved quarks come with the same smearing operator. However, the identities are invalidated if different quark smearing operators enter the interpolator. This allows for additional independent interpolators, albeit with a possibly weakened signal due to the approximate Fierz identities. This strategy is pursued to construct the Lambda spin 3/2 singlet interpolators used in this work (see Appendix C.2). In fact, we find that using different smearing for the quarks, the signal of these interpolators is of the same magnitude as the one of other interpolators. We conclude that such interpolators are relevant for hadron spectroscopy, and we will find that they contribute significantly to low-lying physical states.

The same strategy can be followed to build Δ spin 1/2 interpolators, however, we propose yet another construction. An interpolator with correct quantum numbers of this channel is given by [169]

$$O_\Delta^{J=\frac{1}{2}} = \epsilon_{abc}\, \gamma_\mu \gamma_5 u_a \left(u_b^T\, C\, \gamma_\mu\, u_c \right) , \tag{4.32}$$

where C is the charge conjugation matrix and summation over repeated indices is understood. Using Fierz transformations, one can show that in the case of local fields, this interpolator is identical to zero. As already discussed, different smearing widths are a possibility to make it non-vanishing, nevertheless. However, there is also another way, to be discussed now. A simple Rarita-Schwinger field for the Δ channels reads

$$O^{RS}_{\Delta,\mu} = \epsilon_{abc}\, u_a \left(u_b^T\, C\, \gamma_\mu\, u_c\right) . \tag{4.33}$$

In general, Rarita-Schwinger fields have overlap with both, spin 1/2 and 3/2 states. Thus they need to be projected in order to have definite spin. The Rarita-Schwinger equation is a transversal condition for the projected spin 3/2 field (see, e.g., [172]). Hence, at zero momentum, the projector to spin 3/2 annihilates the time component of the field. Thus the $\mu = 0$ component of the (non-projected) Rarita-Schwinger field has overlap with spin 1/2 only. Consequently, this term has already spin as a good quantum number. The parity of this term is reversed compared to the $\mu \neq 0$ components, therefore we have to include an additional γ_5 matrix for the quark u_a outside the brackets.

The so obtained interpolator is equivalent to the $\mu = 0$ term of the sum denoted in Eq. (4.32). We conclude that the sum can be decomposed into the $\mu = 0$ term and the purely spatial sum, which yields two separate interpolators, which both have good quantum numbers by themselves. In the case of identical smearing of all involved quark fields, Fierz identities are valid and hence these two interpolators coincide up to a sign. Using different quark smearing, however, they become independent. We use the spatial sum to define the interpolator for the Δ spin 1/2 channel. The same line of arguments applies to the nucleon spin 1/2 channel, where we include the corresponding $\mu = 0$ term as third interpolator.

4.3.5 Extracting Excited States

As already mentioned in Chapter 1, the majority of experimental knowledge lies in data on resonances. In Nature, the resonances can decay and are described by the continuous spectrum of the Hamiltonian. This will be briefly reviewed in Section 4.4.2. In a finite system, the spectrum becomes discrete and the eigenvalues of the Hamiltonian contain information about the resonances in the infinite system [97,173]. In the present thesis, the low-lying spectrum of the finite system is determined. This discrete spectrum is compared with experimental data on resonances in the infinite system.

In principle, all energy levels are contained in the Euclidean correlators, as discussed in Section 3.2.3. Thus, the excited spectrum can be expracted by performing a multi-exponential fit to the hadron correlators. For example, the first excited energy level can be obtained by fitting two exponentials at large time separations,

$$\begin{aligned} \langle O(t)|O^\dagger(0)\rangle &= A_0 \mathrm{e}^{-tE_0} + A_1 \mathrm{e}^{-tE_1} + A_2 \mathrm{e}^{-tE_2} + \ldots \\ &\overset{t\to\infty}{=} A_0 \mathrm{e}^{-tE_0} + A_1 \mathrm{e}^{-tE_1} + \mathcal{O}(\mathrm{e}^{-t\Delta E}) , \end{aligned} \tag{4.34}$$

where O is a hadron interpolator, A_i are overlap coefficients, t denotes time, E_i the energy levels and ΔE is the distance to the first neglected energy level. This simple approach has the drawback of introducing a high number of fit parameters, which results in a weak stability of the fit. We briefly introduce a strategy to improve the stability in this approach and afterwards discuss the method which is used in the present work in detail.

Bayesian Methods

The usual χ^2-criterion of the fit can be augmented by a function of the fit parameters, the minimum of which is located at the expected values of them [174–176]. This stabilizes the fit but introduces a bias, however, the amount of it is adjustable. A possible application is to fit in the first place only the ground state at large time separations. Then the result is used as a bias for a fit with more exponential functions at shorter times. Experience tells that this method needs good statistics.

The Variational Method

Currently, the state-of-the-art method to extract excited states energy levels from the lattice is the variational method [49, 50, 177, 178]. The basic idea is to choose interpolators $O(t)$ such that the coefficients A_i of the lower-lying states vanish. If we are interested in the first excitation, this means to consider the subspace orthogonal to the ground state $|E_0\rangle$,

$$\begin{aligned}\langle O_{\perp|E_0\rangle}(t)|O^\dagger_{\perp|E_0\rangle}(0)\rangle &= 0\cdot \mathrm{e}^{-tE_0} + A_1\mathrm{e}^{-tE_1} + A_2\mathrm{e}^{-tE_2} + \dots \\ &\overset{t\to\infty}{=} A_1\mathrm{e}^{-tE_1} + \mathcal{O}(\mathrm{e}^{-t\Delta E})\,. \end{aligned} \tag{4.35}$$

This separation in orthogonal subspaces can be achieved in a very convenient way by a diagonalization procedure. Given a set of N interpolators O_i with matching quantum numbers, one can compute all cross-correlations between them, obtaining the correlation matrix

$$C_{ij}(t) = \langle 0|O_i(t)O_j^\dagger(0)|0\rangle\,. \tag{4.36}$$

The spectral decomposition of this matrix is in general given by (for $t \geq 0$)

$$\begin{aligned} C_{ij}(t) &= \sum_{\alpha=1}^{\infty} v_i^{\alpha *} v_j^{\alpha}\,\mathrm{e}^{-tE_\alpha} \qquad (4.37)\\ v_j^\alpha &= \langle\alpha|O_j^\dagger(0)|0\rangle \\ \mathcal{H}|\alpha\rangle &= E_\alpha|\alpha\rangle \end{aligned}$$

where $\mathcal{H}$ is the Hamiltonian of the theory. One can show that for $t \to \infty$ the eigenvalues λ of the correlation matrix behave as

$$\lambda_\alpha(t) = c_\alpha \mathrm{e}^{-tE_\alpha} \left[1 + \mathcal{O}(\mathrm{e}^{-t\Delta E_\alpha})\right] , \tag{4.38}$$

where ΔE_α is the distance of E_α to other spectral values E_β. However, approaching large t, usually the signal of the correlation matrix becomes bad before the error term in Eq. (4.38) becomes negligible.

In practice, a superior method is given by considering the generalized eigenvalue problem [50]

$$C(t)\,\psi = \lambda(t, t_0)\, C(t_0)\, \psi , \tag{4.39}$$

where t_0 is fixed and small. Again, the eigenvalues behave as Eq. (4.38), but with the crucial difference that the amplitudes c_α and the coefficients of the subleading exponentials are different. One finds that $c_\alpha \approx \mathrm{e}^{t_0 E_\alpha}$ and the other coefficients suppressed, such that the leading term in Eq. (4.38) dominates already at intermediate t, where the signal is still sufficiently strong.

This can be shown considering the finite-dimensional truncated correlation matrix

$$C^{(0)}_{ij}(t) = \sum_{\alpha=1}^{r<\infty} v_i^{\alpha*} v_j^\alpha \, \mathrm{e}^{-tE_\alpha} , \tag{4.40}$$

with r and all $|\alpha\rangle$ such that the correlation matrix $C(t)$ is well approximated. The corresponding eigenvalues of the generalized eigenvalue problem obey

$$\lambda^0_\alpha(t, t_0) = \mathrm{e}^{-(t-t_0)E_\alpha} \tag{4.41}$$

exactly. Writing $C = C^0 + C^1$ and treating C^1 as a small perturbation, one can show that

$$\lambda_\alpha(t, t_0) \propto \mathrm{e}^{-(t-t_0)\,E_\alpha} \left[1 + \mathcal{O}(\mathrm{e}^{-(t-t_0)\,\Delta E_\alpha})\right] , \tag{4.42}$$

where again ΔE_α is the distance of E_α to other spectral values E_β. In the interval $t_0 \le t \le 2t_0$, the error term is even furtherly constrained with ΔE_α being the distance of E_α to spectral values $E_{N+\beta}$ associated with states neglected due to the finite number N of interpolators [178].

Loosely speaking, the concept of the method is to offer a basis of convenient interpolators, wherefrom the system chooses the linear combinations closest to the low-lying physical eigenstates. Obviously, the number of interpolators should be large enough to provide good overlap with the physical states. Furthermore, they should have only little overlap with each other and with the higher modes of the theory, in order to reduce contamination from highly excited states. In actual calculations, at some point, including more interpolators unfortunately increases the statistical noise in the diagonalization. Thus, in practice, one truncates the correlation matrix to a subset. Usually, the optimal choice is to include only a few (3 to 8) interpolators which show good overlap with the low physical modes.

As additional benefit, the variational method can provide information about the content of the physical states (see, e.g., [179, 180]). The eigenvectors represent the linear combinations of the given interpolators which are closest to the considered physical states at each time slice. This will be used, e.g., to discuss the singlet/octet content of Lambda states.

4.4 From the Lattice to Nature: Hadron Phenomenology

Actual simulations are performed at finite lattice spacings, unphysical quark masses and in finite volumes. To make predictions for Nature, one thus has to approach physical quark masses, and to perform the continuum and the infinite volume limit. In addition to this threefold of limits, there is a crucial difference between the theory in a finite box and in the infinite system. In the finite box, the Hamiltonian has a purely discrete spectrum, whereas in the infinite system the spectral density is mainly continuous and includes decaying resonances. In the infinite volume limit, the discrete spectrum becomes denser and denser in the inelastic region and finally approaches the continuous spectrum.

We first discuss the threefold of limits in Section 4.4.1, and afterwards deal with the issue of the energy spectrum in finite and infinite systems in Section 4.4.2.

4.4.1 Determining and Approaching the Physical Point

First of all, the physical point has to be defined. In light and strange hadron spectroscopy, there are three parameters: the gauge coupling, the light and the strange quark mass parameter. Hence, three observables are chosen as input from experiment. In this work, we choose the Sommer parameter, the pion mass and the Ω mass. Since only dimensionless observables can be extracted from lattice simulations, one of the input observables serves to set the scale. This scale enters all dimensionful predictions from the lattice. In principle, the other parameters could be tuned until all input observables exactly match their physical values in Nature. Actual QCD simulations, however, are very expensive, and thus one has to rely on some extrapolation (or interpolation) scheme to approach the physical point defined by the input observables. In this way, the input observables define an extrapolation scheme for all other observables. After this extrapolation, the results correspond to a simulation with physical parameters but still on a finite lattice. Therefore, a continuum limit and an infinite volume limit are necessary as well. Due to asymptotic freedom of QCD, the continuum limit is defined by sending the coupling to zero. The infinite volume limit needs the volume in lattice units to grow faster than the lattice spacing shrinks. While in principle the parameters can be chosen such that the input observables match experimental data, the continuum and the infinite volume limit always have to be performed a posteriori.

In any case, theoretical guidance concerning the fit forms is highly desirable in order to have the systematic errors of the extrapolations at least partly under control. The extrapolations can be chosen following different paths in parameter space. Particular properties, such as disentanglement of different effects or additional symmetry properties, may characterize some of the paths. Alternatively, an entire (hyper)surface can be fitted to perform several or even all extrapolations at once.

In this work, we extrapolate to the physical product of the pion mass and the Sommer parameter, where we use the Sommer parameter to define the lattice spacing (see Section 6.1). Afterwards, we tune the strange quark mass parameter to match the Ω mass approximately (see Section 6.2). The continuum limit is omitted, since only small $\mathcal{O}(a^2)$ discretization effects are expected for the used improved action, and because of considerable computational expenses. Finally, finite volume effects are discussed for specific observables (see Section 9).

Finite volume effects for massive quantum field theories are discussed, e.g., in [97–99, 173]. Chiral Perturbation Theory is the established tool to deal with extrapolation towards lighter pion masses [11, 12], but can also be used to discuss finite volume effects (see, e.g., [181, 182]). A recent review about Chiral Perturbation Theory on the lattice is found in [183]. Discussion based on Chiral Unitary Theory is found, e.g., in [82, 184–186]. The systematics of discretization effects have been treated in the Symanzik Improvement Program [119, 120]. We remark that non-analytic functional forms cannot be excluded [187], in which case control over the systematic errors of the extrapolation would be lost.

4.4.2 Energy Spectra in Finite and Infinite Systems

In an infinite system, a bound state is distinguished from a scattering state through the absence of any continuous open index (see, e.g., [188]). The continuous spectral density is a non-trivial function of the energy, which directly relates to the existence of unstable resonances. In scattering theory, a resonance shows up as a pole of the T matrix which is shifted to the lower-half complex plane by $-i\Gamma/2$. This corresponds to a state whose probability decays like $\exp(-\Gamma t)$. In a unitary theory, assuming the resonance being narrow, one finds that the resonance is well described by Breit-Wigner form [189]. For a single resonance the contribution to the T matrix is proportional to

$$T(E) \propto \frac{i\Gamma}{E - E_R + i\Gamma/2} \,, \tag{4.43}$$

which leads to the characteristic resonant peak of the cross section at the energy E_R with a width equal to the decay rate Γ. The properties of a resonance are also contained in the overall phase shift δ of the scattering matrix near the resonance,

$$\tan\delta(E) = -\frac{\Gamma/2}{E - E_R} \ . \tag{4.44}$$

Within an energy range of order Γ around E_R, the phase shift δ jumps by a factor of π. The resonant peak of the total cross section is located at $\delta = \pi/2$.

In a finite box, the Hamiltonian has a purely discrete spectrum, and all states are stable. Nevertheless, there are states which are more or less localized, allowing for an interpretation in terms of bound states or stationary scattering states in the box. In general, the states will be admixtures of both, which is related to the absence of particle number conservation. However, in many cases the state will be dominated by one type, which can be identified in the variational analysis if one- and many-particle interpolators are included in the basis. Furthermore, the dependence of the energy levels on the pion mass and on the volume can yield useful information.

At first sight, the resonance parameters Γ and δ are absent on finite lattices. However, it was found that the information is encoded in the volume dependence and avoided level crossings of the spectrum [97–99]. To avoid the computational costs of several simulations at different lattice volumes, the resonance parameters can also be extracted from the momentum dependence of the spectrum [100, 101].

Due to limited computational resources, no resonance parameters are extracted in this work. We compute the low-lying spectrum of the Hamiltonian on the finite lattice using single hadron interpolators only. Since the number of particles is not a good quantum number in quantum field theory, in general, these interpolators should have overlap with all states in the given channel. However, the "many-particle" states were found to be suppressed by factors $\mathcal{O}(1/L^3)$ [190, 191], which comes on top of the generic suppression of the excited states. We also observe weak coupling to "many-particle" states, and miss, e.g., the state dominated by $\pi\pi$ scattering in the ρ channel (see Section 7.2.2). Many-particle interpolators will be necessary in order to observe all states. For such attempts, see, e.g., [168, 192–195].

Neglecting further interactions of the hadronic bound states, the energy level $E(A, B)$ for two free hadrons reads

$$E\left[A(\vec{p}), B(-\vec{p})\right] = \left[\sqrt{m_A^2 + |\vec{p}|^2} + \sqrt{m_B^2 + |\vec{p}|^2}\right]\left[1 + \mathcal{O}(ap)\right] \ . \tag{4.45}$$

The hadrons A and B have back-to-back momenta if the whole state is projected to zero momentum. In the infinite volume limit, there is a continuum of scattering states. In a finite box, the momentum $\vec{p}$ can take only discrete values, determined by the boundary conditions, $a\vec{p} = 2\pi(n_x, n_y, n_z)/L$. In the S-wave, the lowest 2-particle state level thus shows vanishing relative momentum. In the P- and D-wave, the lowest 2-particle state level has a momentum of order $\mathcal{O}(2\pi/aL)$.

We discuss signals of scattering states in our data in Sections 7 and 8. A possibility to shed some light on the nature of the state is to monitor the eigenvectors of

Eq. (4.39) of the state when varying parameters of the simulation. Ideally, one compares the eigenvectors for several dynamical simulations, but also partially quenched data can yield some information. Since effects from partial quenching can shift the energy level, corresponding results may also allow to extract further information about the state.

Chapter 5

Simulation Properties

In this chapter, we present some properties of the simulation. The setup of the simulation is detailed in Section 5.1, afterwards Monte Carlo time histories and algorithm properties are briefly discussed in Section 5.2.

5.1 Details of the Simulation

We use the Lüscher-Weisz improved gauge action and the Chirally Improved Dirac operator (D_{CI}) to generate a total of ten ensembles with two dynamical mass-degenerate light quarks. The pion masses lie in the range from 250 to 600 MeV, the lattice spacings in the range of 0.13 to 0.14 fm, according to the definition to be discussed in Section 6.1. The bare parameters of the simulation and the lattice spacings are collected in Table 5.1. The pion masses and (non-renormalized) quark AWI-masses are found in Table 6.2.

The main part of the calculation is performed using seven ensembles with lattices of size $16^3 \times 32$, a linear size of roughly 2.2 fm (see Sections 6, 7 and 8). The other three ensembles are of different sizes and are used to discuss finite volume effects in Section 9. Finite volume effects are expected to be negligible for the Sommer parameter, and surprisingly, in the present work the pion mass is compatible with a flat volume dependence for the volumes considered. Hence, we choose to simplify the setup and use the same lattice spacings and pion masses irrespective of the lattice volumes. For a more detailed discussion, see Section 9.

A leading order chiral fit is performed to extrapolate the observables to the physical pion mass (see Sections 4.4 and 6). A continuum limit is left out due to limited computer resources, which can be partly justified considering small $\mathcal{O}(a^2)$ corrections experienced in quenched simulations using the same action [29]. Finite volume effects are discussed in Section 9.

The Lüscher-Weisz improved gauge action and the Chirally Improved Dirac operator are detailed in Section 4.1. For the gauge action, we use an assumed average plaquette of $u_0 = 0.45$ for all ensembles. The parameters of the Dirac operator have been tuned on quenched configurations and are listed in Appendix A. We have chosen to use these parameters for all ensembles. This affects the chiral properties of the Dirac operator, however, a separate tuning of the parameters for each ensembles would weaken the predictive power. Further details and discussions concerning the HMC algorithm are found in [37, 41, 48].

set	β_{LW}	m_0	m_s	configs.	$L^3 \times T$ $[a^4]$	$m_\pi L$	a [fm]
A50	4.70	-0.050	-0.020	200	$16^3 \times 32$	6.40	0.1324(11)
A66	4.70	-0.066	-0.012	200	$16^3 \times 32$	2.72	0.1324(11)
B60	4.65	-0.060	-0.015	300	$16^3 \times 32$	5.72	0.1366(15)
B70	4.65	-0.070	-0.011	200	$16^3 \times 32$	3.38	0.1366(15)
C64	4.58	-0.064	-0.020	200	$16^3 \times 32$	6.67	0.1398(14)
C72	4.58	-0.072	-0.019	200	$16^3 \times 32$	5.11	0.1398(14)
C77	4.58	-0.077	-0.022	300	$16^3 \times 32$	3.74	0.1398(14)
LA66	4.70	-0.066	-0.012	97	$24^3 \times 48$	4.08	0.1324(11)
SC77	4.58	-0.077	-0.022	600	$12^3 \times 24$	2.81	0.1398(14)
LC77	4.58	-0.077	-0.022	153	$24^3 \times 48$	5.61	0.1398(14)

Table 5.1: Parameters of the simulation: Ten ensembles are generated, their names given in the first row. We show the gauge couplings β_{LW}, the light quark mass parameter m_0, the strange quark mass parameter m_s, the number of configurations analyzed ("configs.") and the volume $L^3 \times T$ in lattice units. The dimensionless product of the pion mass with the spatial extent of the lattice, $m_\pi L$, enters finite volume corrections. We also give the dimensionful lattice spacing a according to the definition discussed in Section 6.1. The three ensembles LA66, SC77 and LC77 are separated from the others by a horizontal line, since they are used only in Section 9 for a discussion of finite volume effects. The pion masses and quark AWI-masses are found in Table 6.2.

5.2 Monte Carlo Time Histories

After equilibration, every fifth configuration is selected for analysis. We show the Monte Carlo (MC) time history for the pion mass of ensembles A50, C77, B70 and A66 in Figure 5.1. No significant autocorrelation is observed, however, we stress that for a rigorous determination of the autocorrelation much more statistics would be necessary. The strong peaks arise naturally towards smaller pion masses through enhanced statistical fluctuations and do not imply serious concerns. In fact, large values of the pion mass usually go along with a cheap inversion of the Dirac operator. Small pion masses correspond to exceptional configurations, which are suppressed in dynamical simulations, as long as small steps are chosen in the numerical integration of the molecular trajectory.

Autocorrelation of topological quantities is known to be particularly problematic in QCD simulations with chiral Dirac operators and at small lattice spacings.

However, at the used simulation parameters, we observe frequent tunneling and an approximately Gaussian distribution of the topological sectors. We show the MC history and a histogram for the topological sectors for ensemble C77 in Figure 5.2.

For Dirac operators fulfilling the Ginsparg-Wilson condition exactly, the eigenvalues lie on a unit circle centered at one. In case of approximate solutions, like the D_{CI} operator, the distribution of the eigenvalues deviates from the circle. We show the smallest 150 eigenvalues of 20 configurations of ensemble A50 in Figure 5.3, left hand side. Figure 5.3, right hand side, shows a histogram for the minimal real part of the eigenvalues of 100 configurations. The deviations from the GW-circle are predominantly towards larger eigenvalues and small eigenvalues are suppressed.

The eigenvalues of the Dirac operator are also important for the stability of the algorithm. Small eigenvalues come with a small weight factor and are thus suppressed. However, there occurrence is enhanced for finite step sizes in the numerical integration of the HMC trajectory. In those cases, the conjugate gradient (CG) solver for the fermion force needs many more iterations to achieve the desired precision. One finds that the reciprocal number of needed CG steps is related to the smallest eigenvalue of $D^\dagger D$ and that the distribution is approximately Gaussian [142]. It was claimed that the algorithm setup is safe if the mean μ of $1/N_{CG}$ is much larger than the standard deviation σ, at least by a factor of three [196]. We show the distribution of $1/N_{CG}$ for the three ensembles with the smallest pion masses in Figure 5.4. We find $\mu/\sigma > 5$ in all cases and conclude that the algorithm setup is safe with respect to small eigenvalues of the Dirac operator.

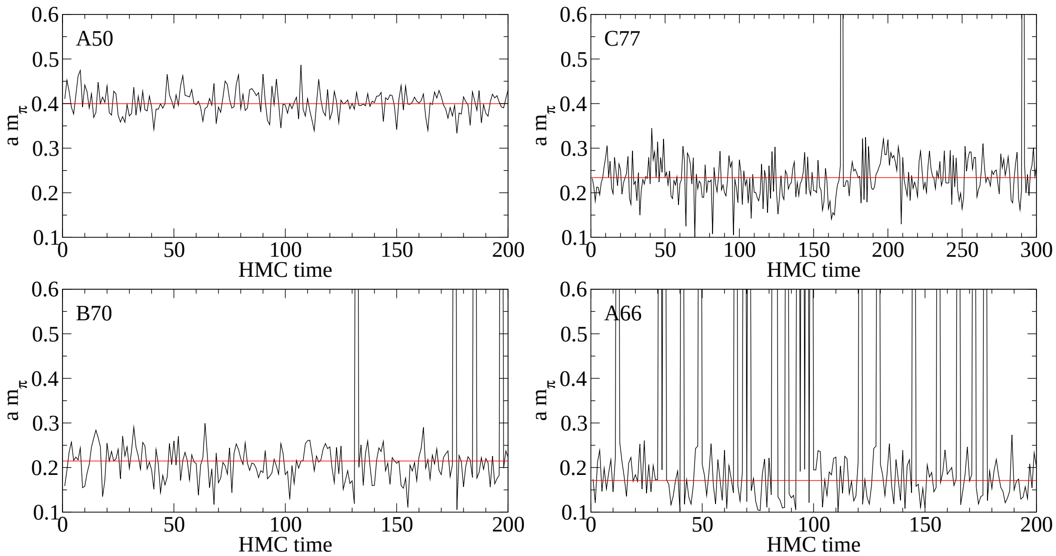

Figure 5.1: Monte Carlo time history for the dimensionless pion mass am_π (here: measured on each individual configuration of the sequence) for ensembles A50, C77, B70 and A66. The red horizontal lines denote the average values. No significant autocorrelation is observed. The strong peaks arise naturally towards smaller pion masses through enhanced statistical fluctuations. (Figure taken from [48].)

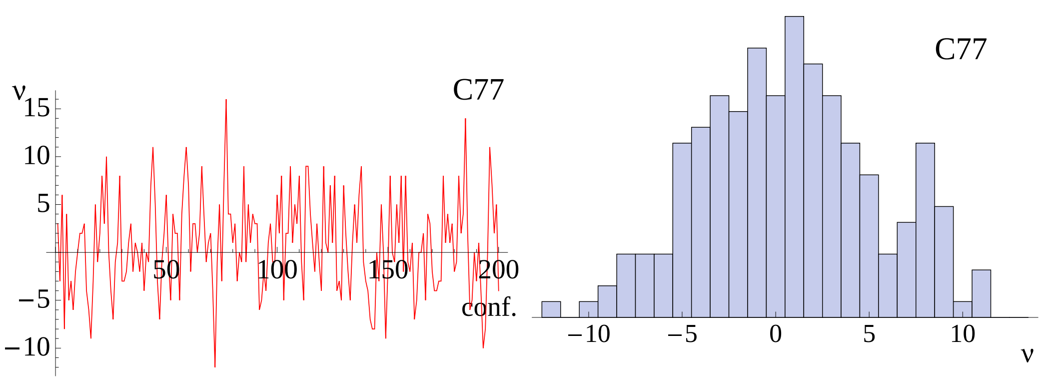

Figure 5.2: Monte Carlo time history (lhs) and histogram (rhs) for the topological sector ν for 200 configurations of ensemble C77. Note the frequent tunneling of the algorithm. (Figure taken from [41].)

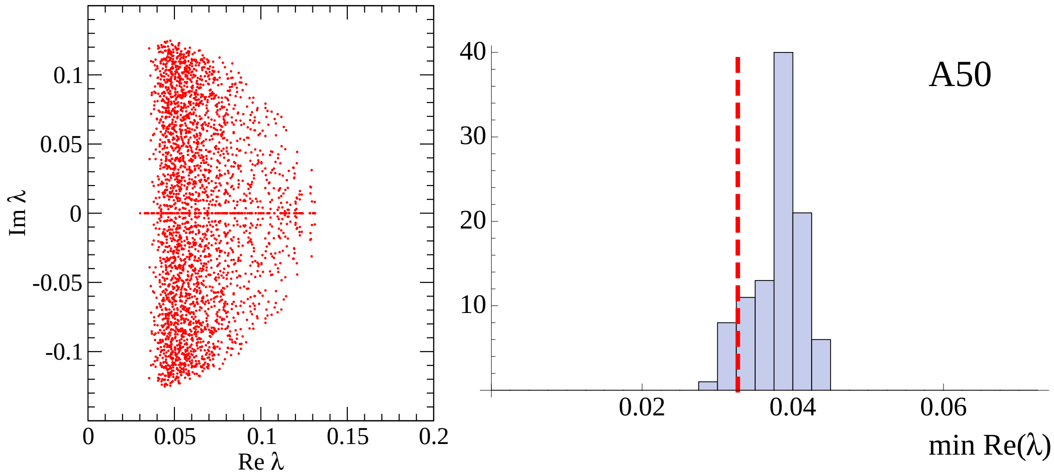

Figure 5.3: Smallest 150 eigenvalues λ of the Dirac operator of 20 configurations of ensemble A50 (lhs) and histogram for the smallest real parts of λ of 100 configurations of A50 (rhs). The deviations from the GW-circle are predominantly towards larger eigenvalues. (Figure taken from [41].)

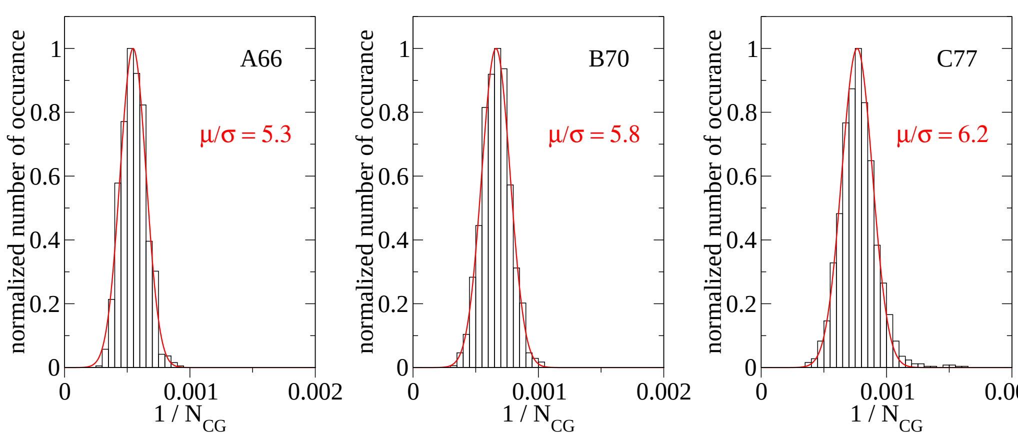

Figure 5.4: Normalized histogram of reciprocal number of conjugate gradient steps needed for the ensembles with the smallest pion masses: A66, B70 and C77. A fit to a Gaussian distribution is included. The ratio of the mean and the standard deviation μ/σ is larger than five in all cases, indicating a safe algorithm setup. (Figure taken from [48].)

Chapter 6

Scale and Low Energy Parameters

We discuss the delicate issue of setting the scale and extrapolation to the physical pion mass in Section 6.1. In our approach, the strange quark mass can be set afterwards, which is described in Section 6.2. The axial vector Ward-Takashi identity is used to extract running current quark masses in Section 6.3. Finally, pseudoscalar decay constants are dealt with in Section 6.4. This chapter has substantial overlap with reference [5].

6.1 Scale

In our earlier work [4] we had analyzed configurations at one quark mass parameter for three values of the gauge coupling. There, we used the lattice spacing derived from the static quark potential with a Sommer parameter $r_{0,\mathrm{exp}} = 0.48$ fm. Now we have two or three quark mass parameters for each gauge coupling and can attempt an extrapolation to the physical point or the chiral limit for each value of the coupling. The latter extrapolation would be relevant for the parameters of Chiral Perturbation Theory (ChPT), which we will not attempt to extract here.

We use two approaches to set the scale. In the first one we determine $y \equiv a/r_0$ from the static quark potential separately for each ensemble, as discussed in [41,197]. We then study the dependence of this quantity on the measured values of $x \equiv (am_\pi)^2$ (cf., Figure 6.1). The physical values are obtained along

$$y = \frac{\sqrt{x}}{m_\pi r_0} \; . \tag{6.1}$$

For each of the three gauge couplings we then perform a linear fit in x and obtain the physical value where the extrapolations intersect Eq. (6.1) with $(m_\pi r_0)_{\mathrm{exp}} = 137\,\mathrm{MeV} \times 0.48\,\mathrm{fm} = 0.3332$. (We use the average of charged and neutral pion masses.) From this one reads off the lattice spacing a. Table 6.1 gives the resulting value in the row labeled $(\pi, r_0)_{\mathrm{phys}}$. The value in the chiral limit is obtained as usual from a/r_0 where $am_\pi = 0$.

The other approach is to replace $y = a/r_0$ by mass values like am_N or am_ρ. Since the ρ is unstable for small enough pion mass, there will be threshold effects. In our parameter range we find no coupling to the (P-wave) $\pi\pi$ sector yet and a

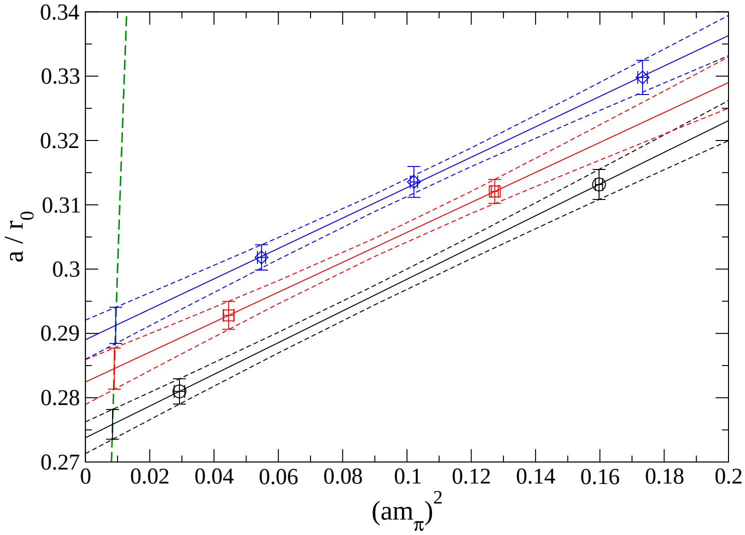

Figure 6.1: Setting the scale with the Sommer parameter and the pion mass as input at the physical point. The green (long-dashed) line is the curve Eq. (6.1). The solid and short-dashed lines represent the extrapolation of our lattice data. Their intersections with the green line define the lattice constants a.

	A	B	C
$(\pi, r_0)_{\mathrm{phys}}$	0.1324(11)	0.1366(15)	0.1398(14)
$(\pi, r_0)_{\mathrm{chiral}}$	0.1314(12)	0.1356(17)	0.1387(15)
$(\pi, \rho)_{\mathrm{phys}}$	0.1330(44)	0.1378(50)	0.1400(29)

Table 6.1: Lattice spacing in physical units derived for ensembles of type A ($\beta = 4.7$), B ($\beta = 4.65$), C ($\beta = 4.58$) (cf., Table 5.1) by the methods discussed in the text.

linear extrapolation intersecting with $y = \sqrt{x}\, m_\rho/m_\pi$ gives the values of the lattice spacing in Table 6.1 compatible with the results of the first method, but with larger errors.

Throughout this thesis we will use the values obtained from the definition denoted by $(\pi, r_0)_{\text{phys}}$ in Table 6.1.

6.2 Setting the Strange Quark Mass

In this two-flavor simulation we use the partial quenching approximation to access the strange hadron spectrum, i.e., we consider the strange quark as a valence quark only. In view of results with full strange quark dynamics (e.g., [198]) we find, at least for the ground states, no noticeable difference in the mass range considered here. In each ensemble the strange quark mass parameter m_s is set by identifying our result for the Ω baryon positive parity ground state energy level with the physical $\Omega(1672)$. These parameters are found in Table 5.1.

For this definition we use $r_{0,\text{exp}} = 0.48\,\text{fm}$ in each ensemble, differing from the (in Section 6.1) discussed method to set the overall scale. Since the two different definitions agree at physical pion masses, this method is consistent at the physical point, but results have to be taken with care at unphysically large pion masses.

6.3 Axial Ward Identity Quark Mass

The so-called axial Ward identity (AWI) mass (or PCAC mass) is determined from the asymptotic (i.e., plateau of the) ratio of the unrenormalized correlators

$$2\, m_{\text{AWI}} = \frac{c_A}{c_P} \frac{\langle 0|\partial_t A_4^-(\vec{p}=0,t)\ X(0)|0\rangle}{\langle 0|P^-(\vec{p}=0,t) X(0)|0\rangle}\ , \tag{6.2}$$

where $P^- = \bar{d}\gamma_5 u$, $A_4^- = \bar{d}\gamma_4\gamma_5 u$, and X is an interpolator with the quantum numbers of the pion, usually P^+ or A^+. The constants $c_A(s)$ and $c_P(s)$ denote the lattice factors relating the smeared interpolators to the lattice point-like interpolators (not to be confused with the renormalization constants Z relating lattice point operators to the continuum renormalization scheme). They are obtained from the ratio of correlators from smeared to point sources [41].

The relation to the renormalized quark mass needs the renormalization factors for the pseudoscalar and axial currents,

$$m^{(r)} = \frac{Z_A}{Z_P}\, m_{\text{AWI}}\ . \tag{6.3}$$

Table 6.2 gives the values of m_{AWI} and m_π for the ensembles studies. (Values for the renormalization constants have been derived in [199, 200].)

Set	a [fm]	$a\,m_\pi$	m_π [MeV]	$a\,m_{\mathrm{AWI}}$	m_{AWI} [MeV]
A50	0.1324(11)	0.3997(14)	596(5)	0.03027(8)	45(1)
A66	0.1324(11)	0.1710(48)	255(7)	0.00589(40)	9(1)
B60	0.1366(15)	0.3568(15)	516(6)	0.02356(13)	34(1)
B70	0.1366(15)	0.2111(38)	305(6)	0.00836(23)	12(1)
C64	0.1398(14)	0.4163(18)	588(6)	0.02995(20)	42(1)
C72	0.1398(14)	0.3196(18)	451(5)	0.01728(16)	24(1)
C77	0.1398(14)	0.2340(27)	330(5)	0.01054(19)	15(1)

Table 6.2: Pion masses and (non-renormalized) quark AWI-masses for the different sets of gauge configurations.

6.4 Decay Constants

The pseudoscalar decay constant describes the coupling to weak decays. It can be extracted from the asymptotic behavior of the correlation between the pseudoscalar or the time components of the axial interpolators.

$$c_A^2\, Z_A^2\, \langle A_4^-(\vec{p}=0,t)\, A_4^+(0)\rangle \sim m_\pi\, F_\pi^2\, \mathrm{e}^{-m_\pi t} \equiv c\,\mathrm{e}^{-m_\pi t}\ . \tag{6.4}$$

The coefficient then gives

$$F_\pi = 2\, m_{\mathrm{AWI}}\, c_P\, Z_A \sqrt{\frac{c}{m_\pi^3}}\ , \tag{6.5}$$

and equivalently for the kaon F_K.

The dependence of the pion decay constant on the quark mass can be described by Chiral Perturbation Theory. Up to 1-loop order one finds [201]

$$F_\pi = F_{\pi,0} - m\,\frac{2\,\Sigma_0}{16\,\pi^2 F_{\pi,0}^3}\,\ln\left(m\frac{2\,\Sigma_0}{\Lambda_4^2 F_{\pi,0}^2}\right)\ . \tag{6.6}$$

Here, $F_{\pi,0}$ and Σ_0 refer to the pion decay constant and the quark condensate in the chiral limit $m \to 0$ and Λ_4 is a low energy constant. The corresponding expressions including the 2-loop order can be found in [202, 203].

The renormalization factor Z_A cancels in the ratio F_K/F_π. We show this ratio in Figure 6.2 where we assume a lattice spacing of 0.135 fm (the average of our values for the scheme $(\pi, r_0)_{\mathrm{phys}}$) and a physical pion mass of 139.57 MeV. The extrapolation of our data to that point gives

$$F_K/F_\pi = 1.215(41)\ , \tag{6.7}$$

which fully covers the experimental value 1.197(9) [7].

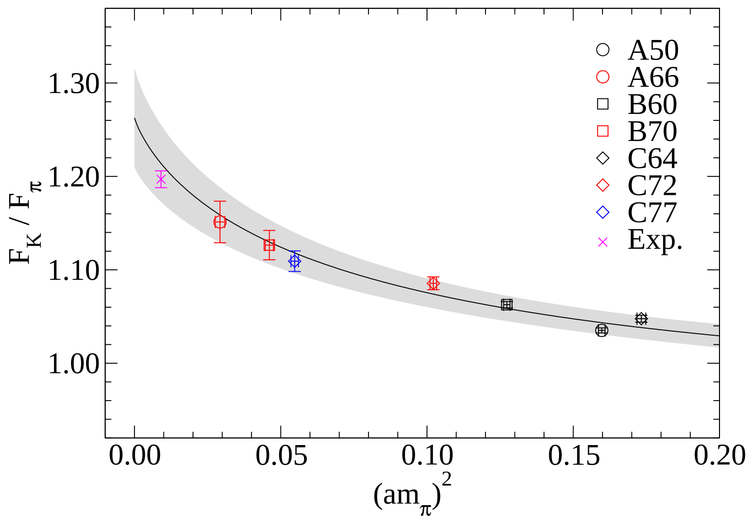

Figure 6.2: The ratio of the pseudoscalar decay constants F_K/F_π is plotted against m_π^2 (in dimensionless units) for each set of gauge configurations. The full black line is a fit of the data using the relevant expressions for numerator and denominator; the shaded area indicates the error band. The magenta cross indicates the experimental value [7]. (Figure taken from [5].)

Chapter 7

Results for the Meson Spectrum

This chapter presents our results for the meson spectrum. First, we briefly review the cornerstones of the analysis in Section 7.1. Then, the isovector light mesons are discussed in Section 7.2 and the strange mesons in Section 7.3. Neglecting disconnected diagrams, isoscalar mesons are investigated in Section 7.4. Finally, we summarize the results for the meson spectrum in Section 7.5. This chapter has significant overlap with reference [5].

7.1 Analysis Flow

The gauge configurations are generated according to Sections 4.1 and 4.2. Interpolating fields are constructed following Section 4.3 and Appendix B.1, listed in Appendix B.2. We consider different subsets of the interpolators to construct several correlation matrices, and apply the variational method, which is detailed in Section 4.3. There are some subtleties in this procedure, to be discussed in the following.

In the limit of infinitely high statistics, the choice of the interpolators becomes irrelevant. All interpolators couple to the low lying physical states, which then determine the correlation functions at large time separations. However, in practice, this coupling may be weak and the time range of a reliable signal short. Thus, for a good signal-to-noise ratio, it is important to select a few interpolators which do have good overlap with the low lying physical states.

Another possible systematic influence comes from choosing the value of t_0 in the variational method and the fit range for the generalized eigenvalues. We use $t_0 = 1a$ throughout. In principle, the impact of that choice can be estimated by choosing several values of t_0 and varying the fit range. For the final fit one should then choose a window where this impact is negligible. However, in practice the corresponding choices are restricted by the given signal-to-noise ratio for coarse lattices and weak signals.

The energy levels are obtained from exponential fits to the eigenvalues in a range of t-values where the eigenvalues and eigenvectors are compatible with an asymptotic behavior. Typically that plateau extends from $t = 2a$ or $3a$ up to $t = 6a$ to $12a$. In some cases the eigenvalues are close to each other and their order changes from one timeslice to another and also changes randomly over the set of configurations. This complicates the exponential fits to the eigenvalues and the automatic attribution of the eigenvectors to physical eigenstates. In such situations we use scalar products of eigenvectors at a given timeslice with the eigenvectors at the preceding timeslice to sort the eigenvalues according to their corresponding physical states. This procedure becomes more reliable towards finer lattice spacings. For subsets of configurations (in the jackknife analysis) the eigenvectors are contracted with the average of the vectors at the same timeslice.

The lattice spacing and the physical point are defined as described in Sections 4.4 and 6. Finally, all energy levels are extrapolated towards the physical point as a function of the pion mass squared. The notions of "chiral extrapolation" and "chiral fit" will be used loosely as synonyms for the extrapolation towards physical pion masses. In the plots we also show the corresponding 1σ error band (dashed curves). The number of energy levels shown is always less than the number of interpolators chosen for the diagonalization. The χ^2 per degree of freedom (d.o.f.) for the chiral fits of all energy levels are collected in the Tables D.1, D.2 and D.3 All figures showing energy levels versus the pion mass squared follow the same convention for the legend, which is detailed once in the caption of Figure 7.1.

7.2 Isovector Light Mesons

7.2.1 Scalars

π : $\mathbf{I(J^{PC} = 1(0^{-+})}$: For the first excitation in the pion channel (see Figure 7.1), the set of operators (1,2,17) is used in all ensembles (see Table B.1). The corresponding effective mass plateaus are rather short, increasing the uncertainty of the extracted mass. Due to the finiteness of the lattice, the back-running pion limits the possible fit range for the first excitation [40, 41, 195], in particular at small pion masses. Nevertheless, masses can be extracted and the chiral extrapolation hits the experimental $\pi(1300)$ within 1σ.

$\mathbf{a_0}$: $\mathbf{I(J^{PC} = 1(0^{++})}$: In reference [4] three (A50, B70 and C77) of the seven ensembles have been analyzed, with less statistics than in the present work. Partially quenched data was used to argue that the signal in the 0^{++} channel probably has significant contributions from the S-wave scattering state $\pi\eta_2$, where η_2 is the pseudo Goldstone boson of the $U(1)_A$ symmetry in two flavor QCD. In the present work we analyze only fully dynamical data (except for the strange sector). Our results are now compatible with the experimental ground state $a(980)$ within 1σ and with the first excitation $a(1450)$ within 2σ (see Figure 7.1). However, the channel still poses some difficulties. The plateau is rather short and there remains some am-

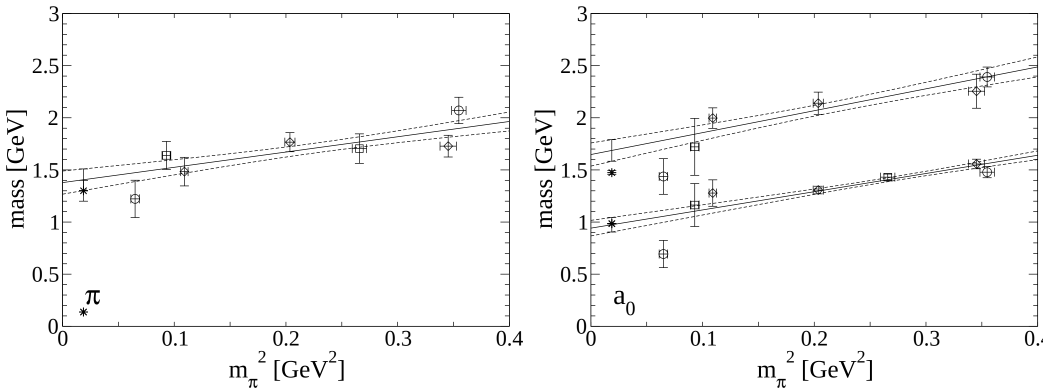

Figure 7.1: Energy levels for light scalar mesons: 0^{-+} (π): Only the first excited energy level is shown (lhs), the ground state pion mass squared defines the abscissa. 0^{++} (a_0): Energy level for the observed ground state and first excitation (rhs). Here and in other figures, circles denote results from ensembles of type A ($\beta = 4.70$), squares denote results from ensembles of type B ($\beta = 4.65$), diamonds denote results from ensembles of type C ($\beta = 4.58$) (see Table 5.1) and stars denote experimental values [7].

biguity in choosing the fit range, leading to a systematic error. In addition, the results depend on the chosen set of interpolators. We show results from subsets of (1,4,10,12,13). In ensemble B60, the excitation signal was not good enough to be fitted. The extrapolations of the ground state levels agree for the different choices of interpolators.

However, in particular the ground state energy level of ensemble A66 deviates when changing the set of interpolators. The result becomes unexpectedly light, most pronounced in the case of the set (10,12,13), though the corresponding effective mass plateaus look stable. Indeed, this point lies below the (theoretical) $\pi\eta_2$ threshold and could indicate a scattering state signal. It could also signal a severe finite size effect for this case in A66, this will be discussed in a forthcoming publication. Nevertheless, except for this point, the results are compatible with the experimental states.

In Figure 7.2(a) we show the eigenvectors for the ground state for three ensembles covering the whole range of pion masses presented. They are fairly consistent with each other and not supporting the notion of a change in the physics of the ground state over that range. Figure 7.2(b) shows the eigenvalues and effective masses of ground state and first excited energy level for the ensemble with smallest pion mass (A66).

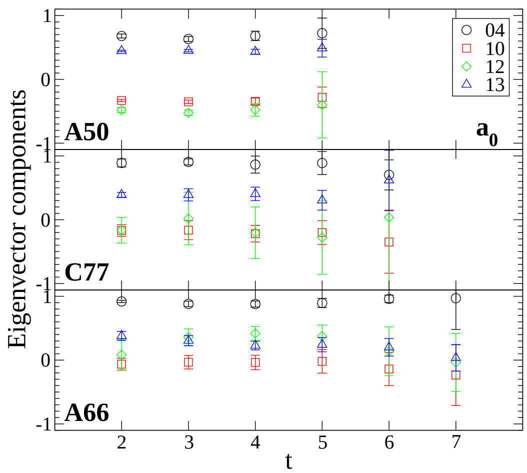

(a) 0^{++}: Eigenvectors

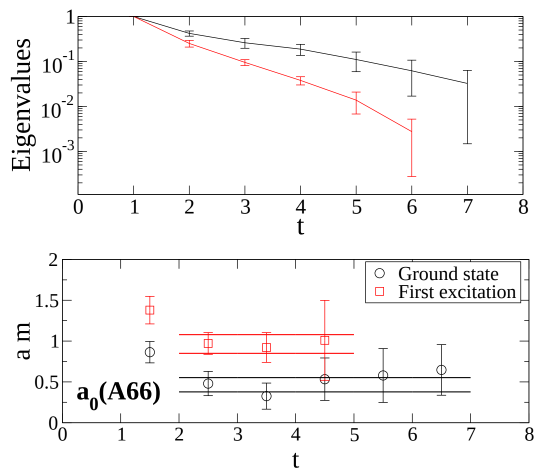

(b) 0^{++}: Eigenvalues and effective masses for A66

Figure 7.2: Subfig. (a): Eigenvector components of the ground state of the light scalar meson channel ($1(0^{++})$) of ensembles A50, C77 and A66 (top to bottom). Interpolator (4) (only gaussian sources) dominates, while contributions of the other interpolators (one or two derivatives) is found to be particularly relevant at heavy pions. Nevertheless, the eigenvectors are very similar over the whole range of pion masses (250 to 600 MeV) and only evolve smoothly. Subfig. (b): Eigenvalues (top) and effective masses (bottom) for the light scalar meson channel ($1(0^{++})$) of ensemble A66, ground state and first excitation.

7.2.2 Vectors

ρ : $\mathbf{I(J^{PC} = 1(1^{--})}$: The $\rho(770)$ comes out nicely as usual (see Figure 7.3). The first and second excitation are extracted using the set (1,8,12,17,22), where the second excitation is not stable in A66. These excitations are very close to one another, making the chiral extrapolations less reliable. The pattern of energy levels would allow a crossover of eigenstates but the eigenvectors do not confirm this. Therefore, we extrapolate the results to the physical point according to the naïvely assumed level ordering, neglecting a possible crossover. The results are compatible with the experimental $\rho(1450)$ and $\rho(1570$ or $1700)$ within error bars (for a discussion on the latter excitation see [7]).

We find no obvious indication for a coupled $\pi\pi$ P-wave channel. As discussed earlier [4, 61] this may be due to weak coupling. By including two pion interpolators one can derive a scattering phase shift from the modification of the observed energy levels close to the resonance (see, e.g., [93]). Such a study needs inclusions of disconnected graphs, which are not accessible to us: The necessary propagator

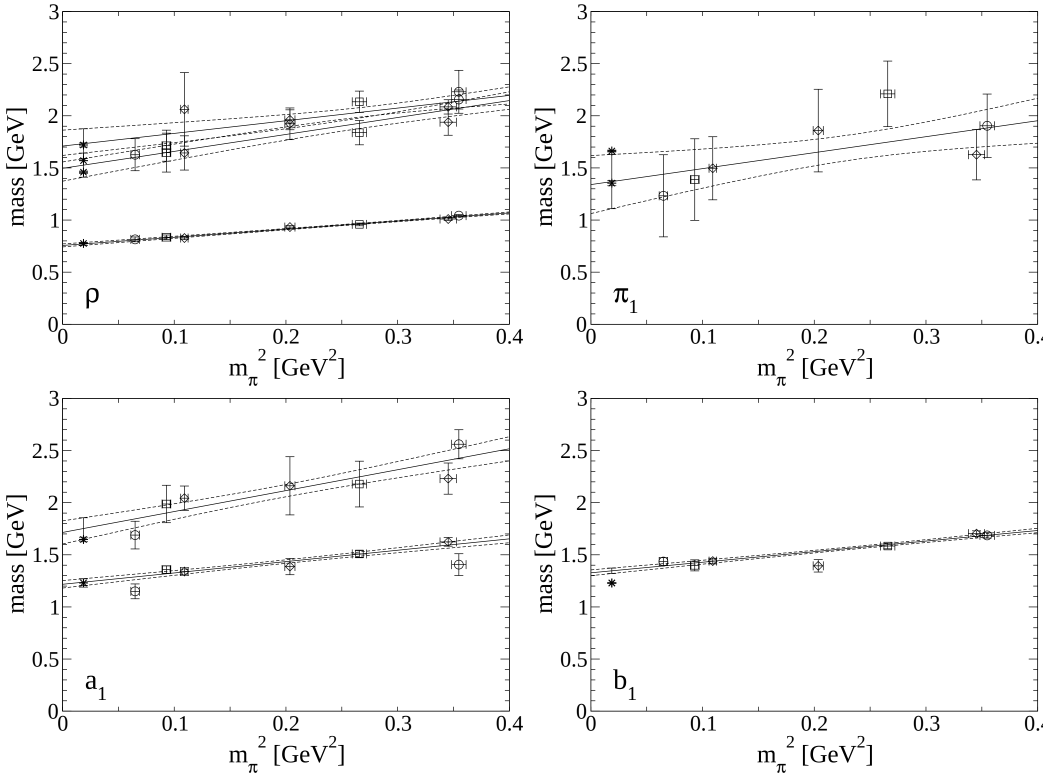

Figure 7.3: Energy levels for light vector mesons: 1^{--} (ρ) (top left); 1^{-+} (π_1) (top right); 1^{++} (a_1) (bottom left); 1^{+-} (b_1) (bottom right); for discussion we refer to the text.

calculation is numerically too costly for CI fermions.

π_1 : $\mathbf{I(J^{PC}=1(1^{-+})}$: The quantum numbers 1^{-+} cannot be obtained with isotropic quark sources only. Thus, this channel is not accessible by simple quark models, and it is commonly referred to as exotic. Due to the weak signal, the set of operators has to be optimized in each ensemble separately, taking one or two interpolators of (9,11,14,16,21,24). This way, energy levels can be extracted, albeit with sizeable error bars. The chiral extrapolation hits the experimental $\pi_1(1400)$, but is also compatible with the $\pi_1(1600)$ (see Figure 7.3). In some of the ensembles we get the best signal using interpolators which are nonzero only due to the definition in Eq. (B.29) and discussed there. This may be related to the "exotic" property of this channel.

$\mathbf{a_1}$: $\mathbf{I(J^{PC}=1(1^{++})}$: The signal in the pseudovector meson channels is usually bad compared to the pion and the ρ channels. Nevertheless, the ground state and a first excitation can be identified. The ground state is extracted using the single

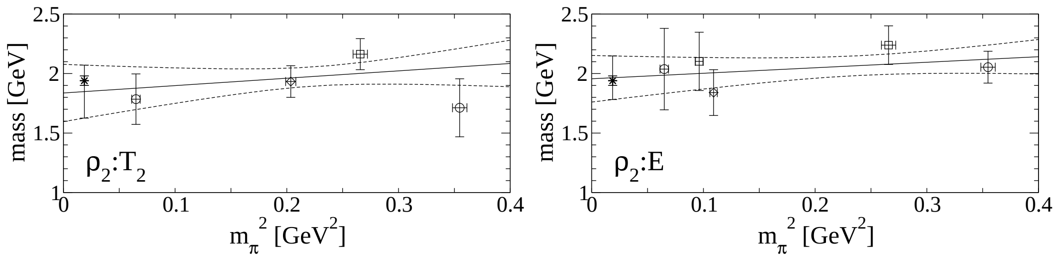

Figure 7.4: Energy levels for light tensor mesons: 2^{--} (ρ_2) in both representations T_2 (lhs) and E (rhs).

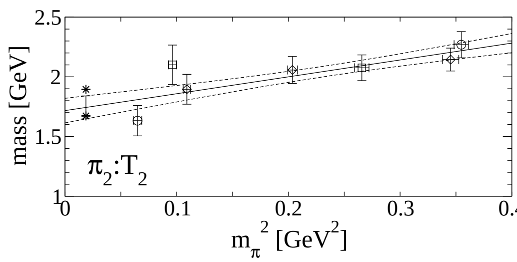

Figure 7.5: Energy levels for light tensor mesons: 2^{-+} (π_2) in representation T_2.

interpolator (1). For the first excitation the set has to be optimized in each ensemble separately, taking subsets of three interpolators out of (1,2,4,13,15,17). Some of the plateaus tend to move towards smaller masses at large time separations. However, as far as possible, long fit ranges are chosen. The chiral extrapolations hit the experimental $a_1(1260)$ and the $a_1(1640)$ within error bars (see Figure 7.3).

$\mathbf{b_1}$: $\mathbf{I(J^{PC}) = 1(1^{+-})}$: In the 1^{+-} channel, the ground state plateau is more stable than in its positive C-parity partner channel (a_1). Using the single interpolator (6), a mass with comparatively small error bar is obtained. The chiral extrapolation comes out too high compared to the experimental $b_1(1235)$ (see Figure 7.3).

7.2.3 Tensors

The continuum representation for spin 2 decomposes into the irreducible representations T_2 and E on the lattice. These interpolators are orthogonal, thus masses can be extracted in each of them separately. In the continuum limit, the results should agree, however, at finite lattice spacings they can show different discretization effects. We extract the energy levels separately and compare the corresponding chiral extrapolations.

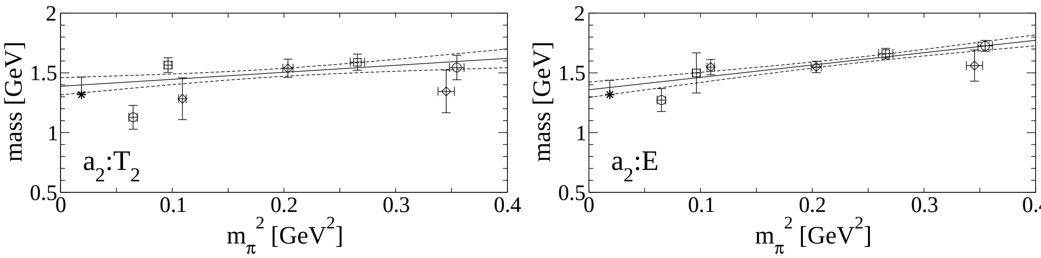

Figure 7.6: Energy levels for light tensor mesons: 2^{++} (a_2) in both representations T_2 (lhs) and E (rhs).

$\rho_\mathbf{2}$: $\mathbf{I(J^{PC} = 1(2^{--})}$: In many of the spin 2 channels the signal is weak and fits can be performed only for some of the seven ensembles. In particular this is the case in the 2^{--} channel (see Figure 7.4). We use the single interpolator (2) in T_2 (see Table B.7) and (2) in E (see Table B.5). The effective masses are noisy, the fitted plateaus are rather short, with only 2 d.o.f. in the fits. Nevertheless, the chiral extrapolations of the T_2 and E ground state masses agree with each other and also with the experimental $\rho_2(1940)$ mass. Hence, our results are compatible with this state, which is omitted from the summary table of [7].

$\pi_\mathbf{2}$: $\mathbf{I(J^{PC}) = 1(2^{-+})}$: In the 2^{-+} channel (Figure 7.5), interpolator (6) is applied in T_2. The extrapolation to the physical point is compatible with the experimental $\pi_2(1670)$ (within 1 resp. 1.5σ). The signal for representation E (not shown) is too weak to be reliable.

$\mathbf{I(J^{PC}) = 1(2^{+-})}$: We studied this channel for completeness but the signals were inconclusive and did not allow to extract an energy level.

$\mathbf{a_2}$: $\mathbf{I(J^{PC}) = 1(2^{++})}$: In the 2^{++} channel (Figure 7.6), we use interpolator (2) in T_2 (see Table B.8) and (2) (respectively (6) for A66) in E (see Table B.6). Some of the plateaus are unexpectedly light, however, that might be statistical fluctuation. The chiral extrapolations of the T_2 and E ground state masses agree and both match the experimental $a_2(1320)$ mass within error bars. The χ^2/d.o.f. of the chiral fit of T_2 is larger than three (see Table D.1), where the major contribution stems from ensemble A66. Finite volume effects could be responsible for the significant deviation of this particular value.

7.3 Mesons with Strange Valence Quarks

In 2-flavor simulations, strange hadrons can be studied by including the strange quark just as a valence quark. The corresponding quantum field theory is not well defined, the probability distribution of physical observables is not anymore strictly non-negative. Nevertheless, since the strange quark is heavy compared to the light, dynamical quarks, observables can be measured and regarded as predictions including systematic errors. We stress that even though light hadrons are well defined in 2-flavor simulations, they also show the systematic error of neglecting strange sea quarks when the results are compared to experiment. From this point of view, the predictive power of strange valence hadrons is not significantly below the one of light hadrons in 2-flavor simulations. The strange quark mass parameter is set in each ensemble such that the $\Omega(1672)$ is reproduced (always assuming that $r_{0,\mathrm{exp}} = 0.48\,\mathrm{fm}$) (see Section 6.2).

In contrast to isovector light mesons, C-parity is no good quantum number for $I = 1/2$ strange mesons due to the non-degeneracy of the light and strange quark mass. At unphysically large pion masses, however, C-parity is approximately restored (see discussion in Section 4.3.4). Our interpolators (see Appendix B) are constructed such that C-parity is a good quantum number in the limit of degenerate quark masses. Therefore, by monitoring the eigenvectors of the variational method, we can learn about the C-parity content of the states.

Since excited states are always more difficult to deal with than ground states, this raises the demands on the variational method. In some cases it is therefore suggestive to separate the channels according to C-parity. At our largest pion masses, around 600 MeV, one expects C-parity to be almost restored. Approaching the physical point, C-parity is violated stronger and stronger, and the corresponding mixing of interpolators is expected to become increasingly important. To investigate this mixing, we include all possible interpolators in the correlation matrix, but we also analyze separately the sectors with given C-parity. The advantage of the second approach is a clearer distinction of the energy levels, where some come in the $[C = +1]$ sector, some in the $[C = -1]$ sector. In the combined correlation matrix we see both sets, but due to the increased noise, fewer levels can be reliably determined. We discuss this point in the subsequent channels. Our results for the dominant C-parity assignments agree qualitatively with [66]. Here we also discuss the corresponding mixing, which is accessible due to our lighter pion masses.

7.3.1 Scalars

$\mathbf{K}$: $\mathbf{I(J^P) = 1/2(0^-)}$: In the strange 0^- channel, interpolator (1) is used for the ground state, which extrapolates close to the experimental kaon (see Figure 7.7). The χ^2/d.o.f. of the chiral fit is larger than four (see Table D.2), which indicates that due to the tiny statistical errors the systematic errors (e.g., of setting the strange quark mass) become visible. For the excited state, we use the set (1,2,8,17), its linear extrapolation towards the physical point agrees with the experimental $K(1460)$ within error bars. Hence we can confirm this state (which is omitted from

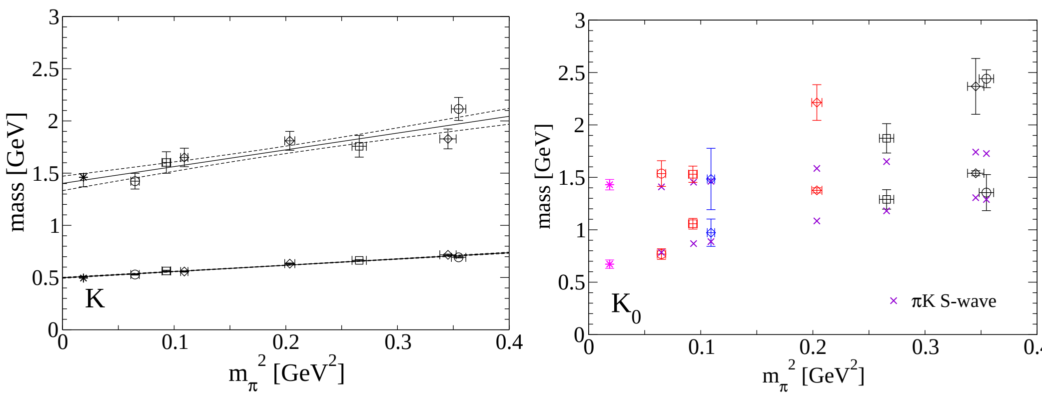

Figure 7.7: Energy levels for strange scalar mesons: $I(J^P) = 1/2(0^-)$ (K) (lhs); and $I(J^P) = 1/2(0^+)$ (K_0) (rhs). For the second case, the S-wave scattering state πK for zero and minimum non-zero relative momentum is indicated for all ensembles using crosses. The chiral fits are omitted for clarity.

the summary table of [7]). In this channel we use only 0^{-+} interpolators, since the signal of the exotic 0^{--} interpolators is too weak, and the corresponding energy levels lie too high.

$\mathbf{K_0}$: $\mathbf{I(J^P) = 1/2(0^+)}$: The strange scalar channel 0^+ is as peculiar as its light multiplet partners. The $K_0^*(800)$ (also called κ) is a very broad resonance (with a width of more than 80% of its mass) and is omitted from the summary table of [7] due to its unclear nature.

Using interpolator (13) alone (not shown), the chiral extrapolation almost hits the presumed center of the resonance. To apply the variational method, we use the set (10,12,13) and include also (1,4) in the basis at small pion masses. We observe that at light pion masses the effective masses tend to decrease at large time separations, which may be a signal for contributions of a scattering state. Like in most cases, we choose a large fit range (e.g., 8 timeslices in A66). The results are compatible with the $K_0^*(800)$ and the $K_0^*(1430)$, but also with the S-wave scattering state πK (see Figure 7.7). The χ^2/d.o.f. of the chiral fit of the ground state is larger than 8 (see Table D.2), which is again interpreted as indication for systematic errors, probably related to scattering states. Here we use only 0^{++} interpolators, the signal of the exotic 0^{+-} interpolators is too weak.

7.3.2 Vectors

$\mathbf{K^*}$: $\mathbf{I(J^P) = 1/2(1^-)}$: Considering the strange J^P channels as mixing of J^{P+} and J^{P-}, one can use information from the corresponding light J^{PC} channels to speculate

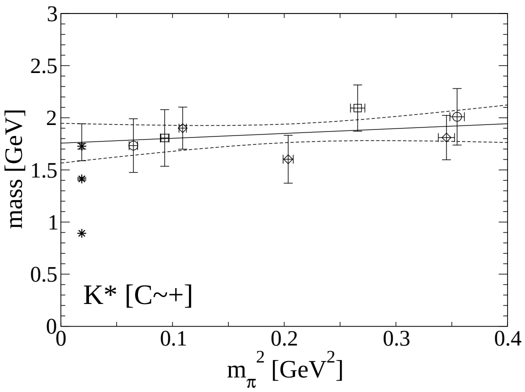

(a) $I(J^P) = 1/2(1^-)\,(K^*)$: Energy levels from interpolators restricted to $C \approx +1$.

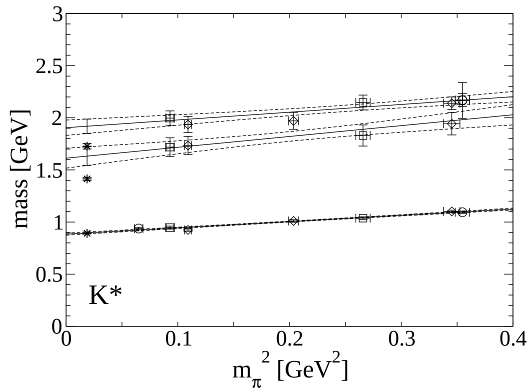

(b) $I(J^P) = 1/2(1^-)\,(K^*)$: Energy levels from interpolators with both types of C-parities.

Figure 7.8: Energy levels for strange vector mesons: $I(J^P) = 1/2(1^-)\,(K^*)$. Subfig. (a): Analysis restricted to $[C \approx +]$ interpolators. Note that the experimental ground state is missed in this case. Subfig. (b): Both types of C-parities included. For discussion we refer to the text.

about the dominating C-parity in the low-lying states of the strange J^P channel. Based on that analogy, in the scalar channels one expects dominance of positive C-parity, which is confirmed by our results. In the vector channels, however, both C-parities are expected to contribute to the measurable low-lying states. Looking at the experimental states in the corresponding light meson channels $\rho(770)$, $\pi_1(1300)$, $\rho(1450)$ and $\rho(1570$ or $1700)$, one expects that the $K^*(892)$ is an (almost) pure 1^{--} state, while mixing could become important for $K^*(1410)$ and $K^*(1680)$.

We first discuss sets of purely negative C-parity interpolators. Taking interpolators (1,8,12,17,20), we extract a ground state and up to two excitations. The chiral extrapolation of the ground state hits the experimental $K^*(892)$ nicely , which is clearly an (almost) pure $[C \approx -]$ state. The excitations are a bit high compared to the experimental $K^*(1410)$ and the $K^*(1680)$. The overall picture is very similar to the one of the analysis with the full basis, which is discussed later.

Considering only 1^{-+} interpolators, the chiral extrapolation hits the $K^*(1680)$ (see Figure 7.8, left hand side). This suggests that mixing is important at least for the $K^*(1680)$.

Finally, taking the set (1,8,9,12,16,20,21), both types of C-parities are included in the variational method. In this analysis, the three lowest states are dominated by $[C \approx -]$ interpolators, where even for the excitations the mixing is compatible with zero. A slight mixing is observed in ensemble A66, however, the signal is very weak, and the corresponding energy levels cannot be extracted reliably. One might wonder why we do not see a significant contribution of $[C \approx +]$ interpolators to at least one of the excitations. A possible interpretation is that the mixing is indeed weak in this

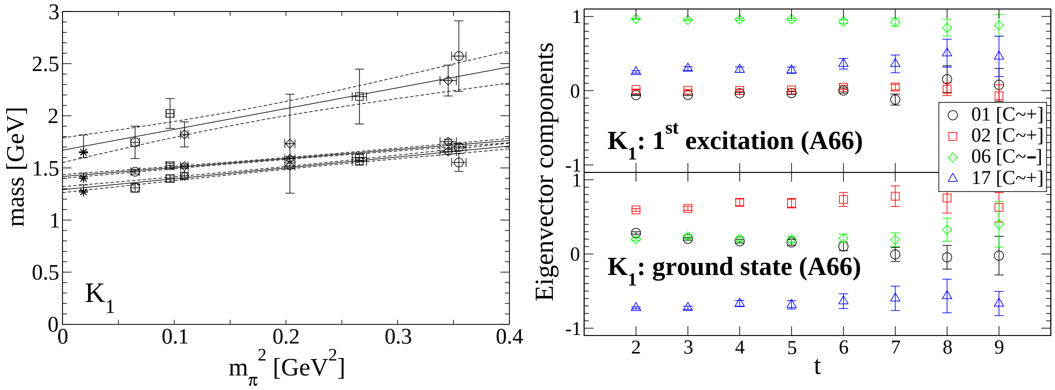

Figure 7.9: Strange vector mesons $I(J^P) = 1/2(1^+)$ (K_1): Results for the energy levels are shown left hand side. The corresponding eigenvectors for the ground state and the first excitation for the lightest pion mass (A66) are shown right hand side. Interpolators (1,2,17) have $[C \approx +]$, (6) has $[C \approx -]$. Note the dominance of positive (negative) C-parity in the ground state (first excitation). Note furthermore that there is some mixing in both states, which is allowed by the breaking of C-parity towards light pion masses. At our largest pion masses, this mixing is suppressed strongly.

channel at all simulated pion masses and that there is a further state, dominated by $[C \approx +]$, which is not clearly identified in the full analysis. The chiral extrapolations of the excitations come out a bit high compared to the experimental $K^*(1410)$ and $K^*(1680)$ (see Figure 7.8, right hand side), suggesting that simulations at smaller pion masses and with higher statistics are necessary in order to reliably describe the mixing of different C-parities and to be able to obtain the $K^*(1410)$.

$\mathbf{K_1}$: $\mathbf{I(J^P) = 1/2(1^+)}$: Looking at the experimental states in the corresponding light meson channels $a_1(1260)$, $b_1(1235)$ and $a_1(1640)$, mixing is expected already for the lowest states $K_1(1270)$, $K_1(1400)$ and $K_1(1650)$.

Employing pure $[C \approx +]$ sets of interpolators, the chiral extrapolation of the ground state ends up between the $K_1(1270)$ and the $K_1(1400)$. The first excitation hits the $K_1(1650)$ within error bars. From pure $[C \approx -]$ interpolators only a ground state can be extracted, the chiral extrapolation of which agrees with the $K_1(1400)$.

Allowing for both types of C-parity, three states can be extracted when the set of interpolators is optimized in each ensemble. The chiral extrapolations are compatible with $K_1(1270)$, $K_1(1400)$ and $K_1(1650)$ (see Figure 7.9, left hand side). Since the splitting of $K_1(1270)$ and $K_1(1400)$ is rather small, it is hard to make a statement about its increase towards smaller pion masses. This is worsened by the fluctuation of the plateau points. However, the eigenvectors indeed show stronger mixing approaching the physical point (see Figure 7.9, right hand side), which is

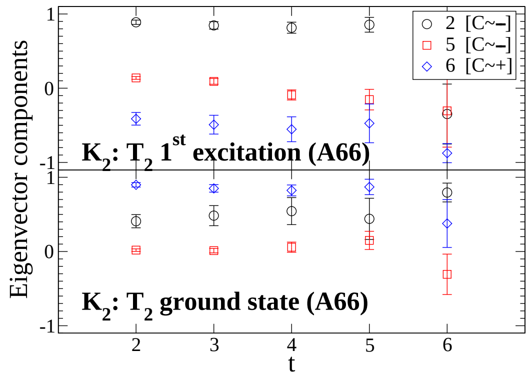

Figure 7.10: The eigenvectors for $I(J^P) = 1/2(2^-)$ (K_2) for the ground state and the first excitation for the lightest pion mass (A66) are shown. Interpolators (2,5) have $[C \approx -]$, (6) has $[C \approx +]$. Note the dominance of positive (negative) C-parity in the ground state (first excitation). Note furthermore that there is significant mixing in both states, which is allowed by the breaking of C-parity towards light pion masses. At our largest pion masses, this mixing is suppressed. The mixing pattern is similar in representation E (not shown).

usually accompanied by a more pronounced splitting. At simulated pion masses, $K_1(1270)$ and $K_1(1650)$ are dominated by $[C \approx +]$, $K_1(1400)$ by $[C \approx -]$ interpolators. Our results confirm the existence of $K_1(1650)$ (omitted from the summary table of [7]), which is dominated by positive C-parity in our analysis.

7.3.3 Tensors

$\mathbf{K_2}$: $\mathbf{I(J^P) = 1/2(2^-)}$: In the spin 2 channels, investigation of the mixing becomes more complicated, since the signal is often weak already for the ground state. From the light meson states $\pi_2(1670)$, $\pi_2(1880)$ and the (not established) $\rho_2(1940)$, one could expect a dominance of $[C \approx +]$ interpolators in the ground state. So far, $K_2(1580)$ is omitted from the summary table of [7], the lowest established states in this channel are $K_2(1770)$ and $K_2(1820)$.

Restricting the basis to negative C-parity, we use interpolator (2) as in the corresponding light channel. In both T_2 and E, the chiral extrapolation is compatible with $K_2(1770)$ and $K_2(1820)$. For positive C-parity, using interpolator (6) in T_2 and (8) in E, the chiral extrapolations are again compatible with $K_2(1770)$ and $K_2(1820)$.

To take into account both C-parities, the set (2,5,6) (resp. (3,4,5,6) in C72) is chosen in T_2 and (2,5,8) in E. The two lowest eigenvalues are very close and have to be sorted according to the eigenvectors. The eigenvectors of T_2 are shown in Figure 7.10. We observe that the ground (excited) state is dominated by positive (negative)

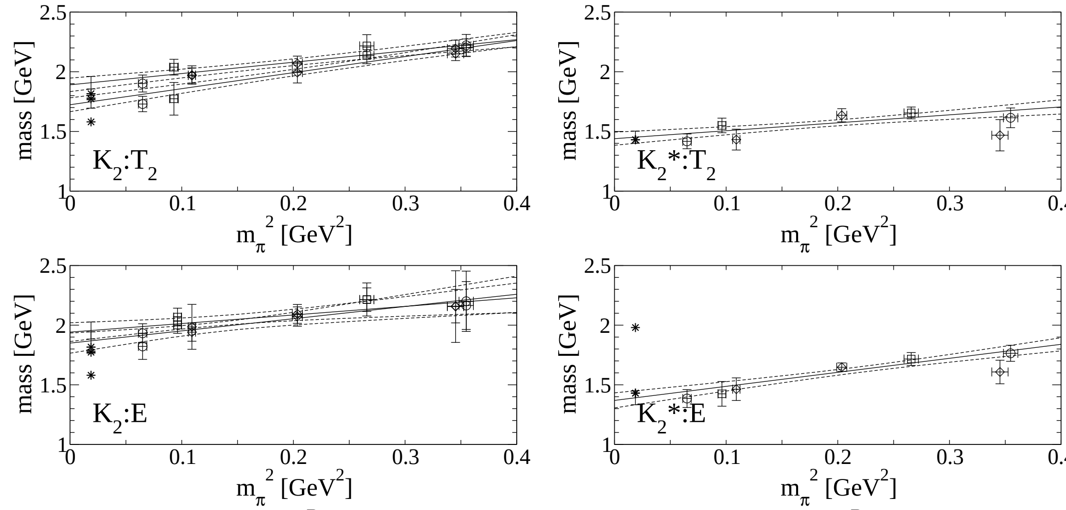

(a) Energy levels for $I(J^P) = 1/2(2^-)\,(K_2)$. (b) Energy levels for $I(J^P) = 1/2(2^+)\,(K_2^*)$.

Figure 7.11: Energy levels for strange tensor mesons. Subfig. (a) shows $I(J^P) = 1/2(2^-)\,(K_2)$ in both representations T_2 and E. Subfig. (b) shows $I(J^P) = 1/2(2^+)\,(K_2^*)$ in both representations T_2 and E. Chiral fits are suppressed for clarity.

C-parity. However, there is significant mixing in both states, which appears to be the strongest mixing of all channels considered. Strong mixing is also observed in representation E. The chiral extrapolations are compatible with the experimentally established $K_2(1770)$ and $K_2(1820)$ (compare Figure 7.11, left hand side) and do not confirm the $K_2(1580)$, which is omitted from the summary table of [7]. However, increasing mixing towards lighter pion masses could still change the slope of the chiral extrapolation.

$\mathbf{K_2^*}$: $\mathbf{I(J^P) = 1/2(2^+)}$: No experimental state is known in the light-quark 2^{+-} channel. In the light 2^{++} channel, the lowest states are $a_2(1320)$, $a_2(1700)$ and $a_2(1950)$, of which the latter two are not established. In the strange 2^{+-} channel the lowest experimental states are $K_2^*(1430)$ and the (not established) $K_2^*(1980)$.

The signal of negative C-parity interpolators is weak here, thus we restrict our analysis to positive C-parity interpolators. Interpolator (2) (Table B.8) is used in T_2 and interpolator (2) (Table B.6) in E to extract a ground state mass. In both lattice channels, the chiral extrapolation hits the experimental $K_2^*(1430)$ nicely (see Figure 7.11, right hand side).

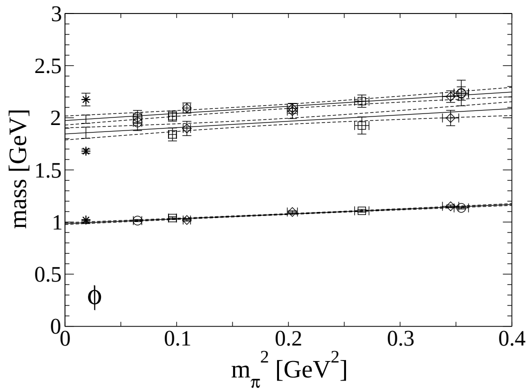

Figure 7.12: Energy levels for isoscalar vector mesons ϕ: $I(J^{PC}) = 0(1^{--})$

7.4 Isoscalar Light Mesons

ϕ : $\mathbf{I(J^{PC}) = 0(1^{--})}$: In principle, correlation functions of isoscalar mesons include connected and disconnected diagrams. The low lying isoscalar ϕ mesons decay mainly into kaons, thus one expects that these states are dominated by strange quarks (Zweig rule). Since disconnected diagrams are dominated by loops of light sea quarks, it is reasonable to assume that the ϕ mesons are dominated by connected (strange) diagrams. We extract ϕ meson masses evaluating only these connected diagrams, albeit with the systematic error of neglecting the disconnected diagrams. We use the same set of operators as in the light isovector 1^{--} (ρ) channel (see Section 7.2.2) to extract three energy levels.

The ground state mass extrapolates to a value very close to the experimental $\phi(1020)$ mass (see Figure 7.12), which confirms our choice of the strange quark mass parameters. The extrapolation of the excited states ends up significantly higher than the experimental $\phi(1680)$. Since the first excitation $\rho(1450)$ in the light isovector channel is reproduced nicely, one may conclude that the neglected disconnected diagrams play a more important role for the $\phi(1680)$ compared to the $\phi(1020)$. The lattice irreducible representation T_1 couples to continuum spins 1 and 3 (among others). The extrapolations of the first and second excitation are indeed both compatible with the spin 3 state $\phi_3(1850)$. However, all our interpolators in this channel have a naïve continuum limit of spin 1, which indicates that the matching with $\phi_3(1850)$ is probably an accident.

$\mathbf{f_2}$: $\mathbf{I(J^{PC}) = 0(2^{++})}$: As in the ϕ meson channel, the experimental decay channels of the isoscalar light meson f_2 suggest dominance of connected diagrams. We use the same interpolators as in the isovector 2^{++} (a_2) channel. The results of T_2 and

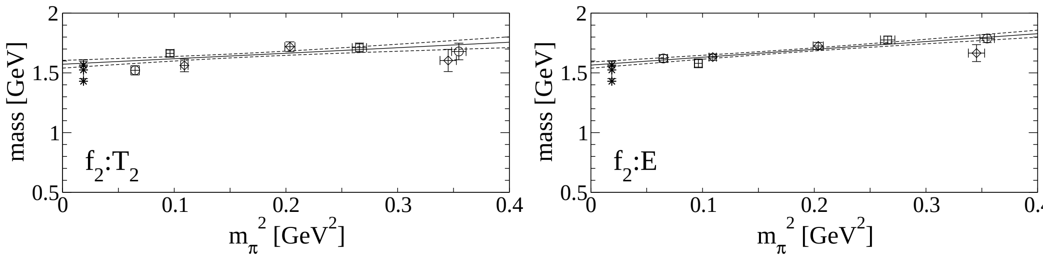

Figure 7.13: Energy levels for isoscalar tensor mesons f_2: $I(J^{PC}) = 0(2^{++})$ in representations T_2 (lhs) and E (rhs).

E agree (see Figure 7.13), but their chiral extrapolations are in better agreement with the $f_2'(1525)$ than with the $f_2(1430)$. The latter needs confirmation and is not listed in the summary table of [7]. It is unclear if inclusion of the neglected disconnected diagrams would yield the $f_2(1430)$ or if the ground state of the theory is the established $f_2'(1525)$.

7.5 Summary of the Results for the Meson Spectrum

In this chapter, the results for the meson spectrum from our simulation have been presented. Figure 7.14 shows the results after extrapolation to physical pion masses compared to experimental values [7]. The results are in general in good agreement with experiment. As discussed in more detail in Sections 7.2 and 7.3, we do not see any clear indications of scattering states, which probably show only little overlap with the one-particle interpolators used in this work. Exceptions are the strange 0^+ channel and the light isovector 0^{++} channel at small quark masses, where our signal is also consistent with a two-particle scattering state.

The strange meson channels 1^-, 1^+ and 2^- have been investigated with respect to their approximate C-parity. In the 1^- channel, the three lowest states seem to be dominated by negative C-parity, while positive C-parity was shown to contribute to a state in the vicinity of the second excitation. The low-lying states in the 1^+ channel support level ordering obeying alternating C-parity dominance, where some mixing of different C-parity is found towards light pion masses. The 2^- channel shows strong mixing towards light pion masses and the ground state (first excitation) is dominated by positive (negative) C-parity.

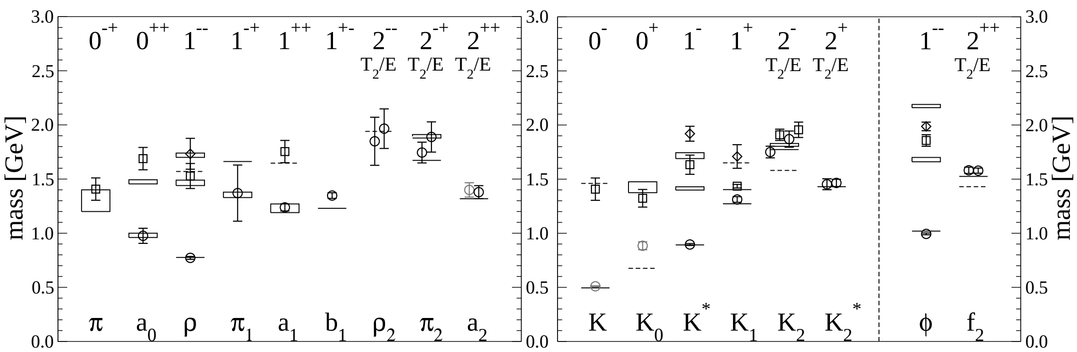

Figure 7.14: Energy levels for isovector light mesons (lhs) and strange and isoscalar mesons (rhs). All values are obtained by chiral extrapolation linear in the pion mass squared. Horizontal lines or boxes represent experimentally known states, dashed lines indicate poor evidence, according to [7]. The statistical uncertainty of our results is indicated by bands of 1σ, that of the experimental values by boxes of 1σ. In case of spin 2 mesons, results for T_2 and E are shown side by side. The strange quarks are implemented in the partial quenching approximation. The isoscalars additionally suffer from neglected disconnected diagrams. Grey symbols denote a poor χ^2/d.o.f. of the chiral fits (see Tables D.1, D.2 and D.3).

Chapter 8

Results for the Baryon Spectrum

This chapter presents our results for the baryon spectrum. First, we present light baryons in Section 8.1. Then, strange baryons are discussed in Section 8.2. Finally, we summarize the results for the baryon spectrum in Section 8.3.

8.1 Results for Light Baryons

8.1.1 Nucleons

N : $\mathbf{I(J^P) = 1/2(1/2^+)}$: The nucleon spin $1/2^+$ ground state is the lightest baryonic bound state of QCD. We use interpolators covering three Dirac structures and different levels of quark smearing, (1,2,9,10,19,20) (see Appendix C), to extract four states. Let us first discuss the ground state. The leading order chiral extrapolation yields an energy level around 10% larger than the experimental $N(939)^{****}$ (see Figure 8.1). Here and in the following, the stars as superscript of experimental states denote the level of quality classified by [7]. The deviation may be caused by systematic errors like finite volume effects, which will be discussed in Chapter 9. Within the finite basis used in the variational method, the ground state is dominated by the first Dirac structure, with a contribution of the third one. We stress that (at least for pairwise different quark smearing) all Dirac structures used generate independent field operators which are not related by Fierz transformations (see Section 4.3.4).

The first excitation in the nucleon channel, $N(1440)^{****}$, the "Roper resonance", is famous because it is lighter than the ground state in the corresponding negative parity channel. This "reverse level ordering" is contrary to the predictions of most simple quark models (see, e.g., [204, 205]). However, in our simulation, the first excitation is about 500 MeV higher than the experimental Roper, and supports conventional level ordering with alternating parity. We briefly discuss some possible systematic effects which may cause this deviation. First of all, finite volume effects could shift the energy level up. This may be enhanced for this state, since in quark models it is considered as a radial excitation, which implies an enlarged size. Unfortunately, the signal of the eigenvalues is weak and the fit range short, which complicates a reliable analysis of finite volume effects. On the other hand, possi-

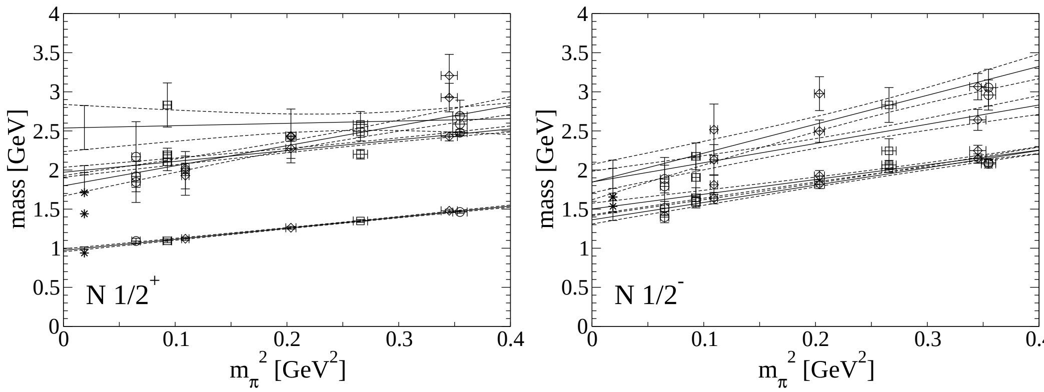

Figure 8.1: Energy levels for nucleon spin $1/2^+$ (lhs) and $1/2^-$ (rhs).

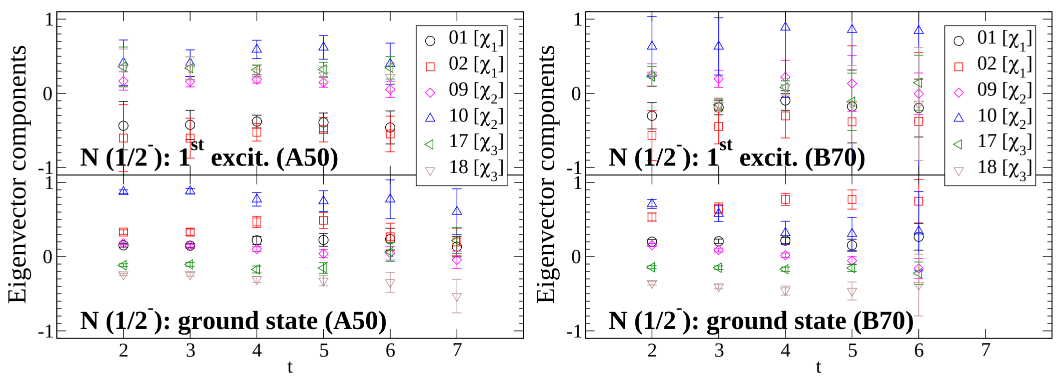

Figure 8.2: Eigenvectors for nucleon spin $1/2^-$ ground state (bottom) and first excitation (top), ensemble A50 (lhs) and B70 (rhs). Note the different composition of the states at the different pion masses. Details are discussed in the text.

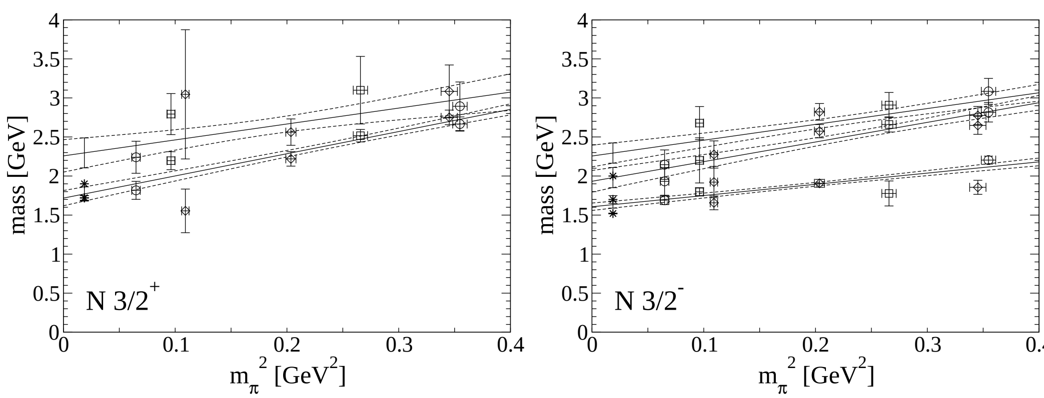

Figure 8.3: Energy levels for nucleon spin $3/2^+$ (lhs) and $3/2^-$ (rhs).

bly the used interpolators do not couple strongly enough to the Roper resonance. Finally, the discrete energy levels of the P-wave scattering state πN also could influence the situation dramatically by mixing and avoided level crossings. Comparing to the corresponding quenched simulations [35], the results in the nucleon positive parity channel do not deviate significantly. Our data are also in agreement with quenched and dynamical results from other groups (e.g., [57, 59, 61]). Towards physical pion masses, the first excitation was reported to bend down significantly [62], however, still all results from the lattice are closer to the $N(1710)^{***}$ than to the Roper resonance $N(1440)^{****}$.

After chiral extrapolation, we obtain two close excitations within roughly 1800-2000 MeV. One of those has a χ^2/d.o.f. of the chiral fit of larger than three (see Table D.4), which suggests a non-linear dependence on m_π^2. However, a chiral fit incorporating only data with pion masses below 350 MeV misses the experimental Roper resonance as well. In several of our ensembles, the excited energy levels overlap within error bars. Related to this, the order of states is not the same in all ensembles. At light pion masses, the first excitation is dominated by a linear combination of interpolators of the second Dirac structure; the second excitation is dominated by the first Dirac structure, with some contribution from the third one. Towards heavier quark masses, this level ordering interchanges. This supports a picture of level crossing between the first and second excitation in the range of pion masses simulated. The linear combination of interpolators with different quark source widths at light pion masses is compatible with the picture of a radial excitation. This behavior seems to be stable as long as the basis is not truncated too strongly.

N : $\mathbf{I(J^P) = 1/2(1/2^-)}$: In general, we find somewhat low energy levels in the negative parity baryon channels, compared to experiment. This is also true for the nucleon spin $1/2^-$ channel. We use again the set of interpolators (1,2,9,10,19,20), and find that the ground state comes out too low and the chiral extrapolation of the first excitation hits the experimental ground state (see Figure 8.1). A possible explanation can be formulated as follows. In Nature, the S-wave state πN (neglecting the interaction energy) lies below the one-particle ground state $N(1535)^{****}$ in the nucleon negative parity channel. This may also hold at some of the simulated pion masses, e.g., in ensemble A66 or even in C77. Increasing the pion mass further, the scattering state becomes heavier than the 1-particle state. This suggests a (avoided) level crossing of the two states. Indeed, our results on energy levels are compatible with such a picture. In [4] we analyzed only a subset of the configurations available in this work. We argued that the eigenvectors give no indication for a level crossing in the range of pion masses between roughly 300 and 600 MeV. In the present work, we can monitor the eigenvectors down to pion masses of 250 MeV. Furthermore, we use a larger basis, albeit at the cost of introducing additional noise. Note that we use the same quark smearing structures for different Dirac structures, such that the eigenvectors give information about the content of the state without the need of additional normalization of the interpolators. We find indeed a significant change in the eigenvectors towards the physical point. The eigenvectors are shown for ensembles A50 and B70 in Figure 8.2. In particular, the ground state is dominated by interpolator (2) (χ_1) around $m_\pi = 300$ MeV, and by interpolator (10) (χ_2) above $m_\pi = 500$ MeV. For the first excitation, interpolator 10 contributes stronger at lighter pion masses compared to heavier ones. This trend is observed also in the other ensembles and at partially quenched data. However, while the change in the content of the states is obvious, it does not directly support a (avoided) level crossing. The reason is the different relative sign of the interpolators, as easily inspected from Figure 8.2. Further discussion is postponed to a forthcoming publication.

$\mathbf{N}: \ \mathbf{I(J^P) = 1/2(3/2^+)}$: In the nucleon spin $3/2^+$ channel, only two states are known experimentally: The $N(1720)^{****}$ and the $N(1900)^{**}$, where the latter needs confirmation. We use interpolators (1,4,5), respectively (1,2,3,4) in A66 and B70. The signal is rather noisy and the effective mass plateaus appear to drop towards large time separations. Sizeable deviations from the chiral fit are observed in ensembles B70 and C77. Nevertheless, the chiral extrapolation of the ground state agrees well with the experimental $N(1720)^{****}$ (see Figure 8.3). The first excitation overshoots the $N(1900)^{**}$ by about 2σ, which thus cannot be confirmed.

$\mathbf{N}: \ \mathbf{I(J^P) = 1/2(3/2^-)}$: In this channel, experimentally, $N(1520)^{****}$ and $N(1700)^{***}$ are established, while $N(2080)^{**}$ needs confirmation. Using interpolators (1,2,3,4), three states can be extracted in our simulation (see Figure 8.3). The ground state extrapolates to a value between the $N(1520)^{****}$ and the $N(1700)^{***}$, the first excitation to the $N(2080)^{**}$ and the second comes out even higher.

8.1.2 Delta Baryons

$\mathbf{\Delta}: \ \mathbf{I(J^P) = 3/2(1/2^+)}$: Experimentally, the ground state $\Delta(1750)^*$ still needs confirmation, while $\Delta(1910)^{****}$ is well established. In our simulation, using interpolators (1,4,5), we find two states, where the second eigenvalue decays slower than the first one. The resulting crossing of the eigenvalues complicates the analysis. However, the plateaus can be fitted and energy levels extracted, albeit with sizeable error bars. The chiral extrapolation of the ground state is compatible with both $\Delta(1750)^*$ and $\Delta(1910)^{****}$, the first excitation comes out higher (see Figure 8.4). The interpolators for this channel are constructed following Section 4.3.4.

$\mathbf{\Delta}: \ \mathbf{I(J^P) = 3/2(1/2^-)}$: In the negative parity channel, $\Delta(1620)^{****}$ is established, while $\Delta(1900)^{**}$ needs confirmation. Using interpolators (1,2,3,4), we extract two states in this channel. The chiral extrapolation of the ground state hits

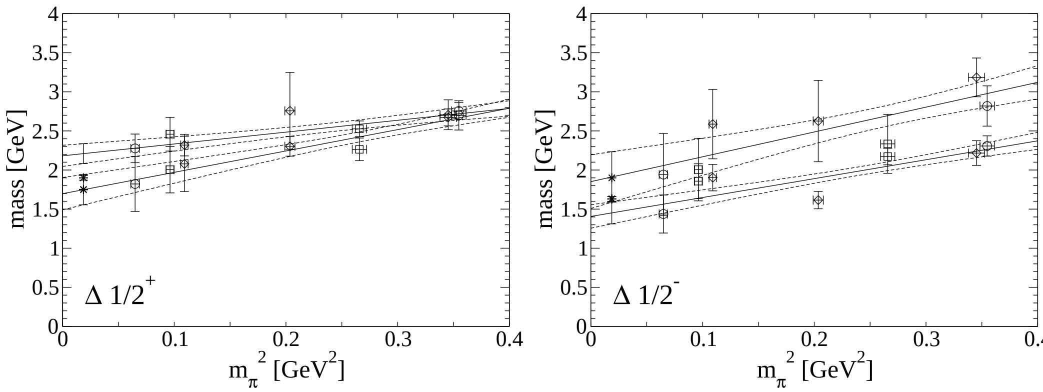

Figure 8.4: Energy levels for Δ spin 1/2, positive (lhs) and negative parity (rhs).

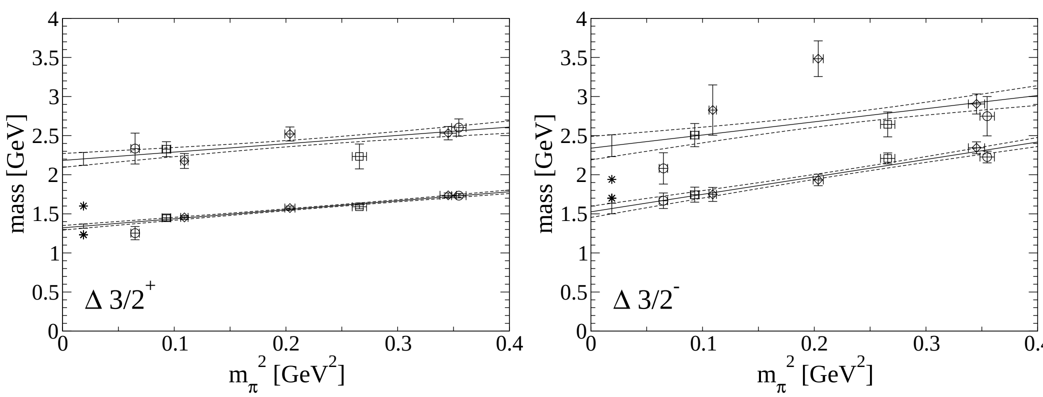

Figure 8.5: Energy levels for Δ spin 3/2, positive (lhs) and negative parity (rhs).

the experimental $\Delta(1620)^{****}$ within 1.2σ (see Figure 8.4). $\Delta(1900)^{**}$ is hit nicely, however, the associated error bar is too large to claim confirmation of this state.

$\mathbf{\Delta}$: $\mathbf{I(J^P) = 3/2(3/2^+)}$: The $\Delta(1232)^{****}$ is the lowest resonance of all spin 3/2 baryons. We find a good signal of two states, the chiral extrapolations of which both come out too high compared to the experimental $\Delta(1232)^{****}$ and the $\Delta(1600)^{***}$ (see Figure 8.5). Finite volume effects are a possible origin of the discrepancy, which will be discussed in Chapter 9. Note that the partially quenched data of this channel are used to set the strange quark mass parameter (see Section 6.2).

$\mathbf{\Delta}$: $\mathbf{I(J^P) = 3/2(3/2^-)}$: We find a good signal in the Δ spin $3/2^-$ channel in all seven ensembles (see Figure 8.5). However, as in some other negative parity baryon channels, the chiral extrapolation of the ground state comes out low compared to experiment. The results for the first excitation are inconclusive, the χ^2/d.o.f. of the chiral fit is larger than three.

8.2 Results for Strange Baryons

8.2.1 Lambda Baryons

$\mathbf{\Lambda}$: $\mathbf{I(J^P) = 0(1/2^+)}$: The Λ baryons have isospin zero, which can be realized from singlet or octet representations. While these are orthogonal at the $SU(3)_f$ symmetric point, they are allowed to mix towards the physical point. We use the set of interpolators (1,2,11,20,25,26,33,34,43), which includes different Dirac structures for both singlet and octet flavor structures. We extract four states, and find that after extrapolation to the physical point our lowest energy level agrees nicely with the experimental $\Lambda(1116)^{****}$. Our first excitation matches $\Lambda(1810)^{***}$, but is also compatible with $\Lambda(1600)^{***}$ within 2σ. The chiral fit of the second excited energy level shows a χ^2/d.o.f. around four (see Table D.4). The cause lies probably in the closure of the eigenvalues and corresponding difficulties of extracting energy levels and assigning them to states. Analyzing the eigenvectors, we find that in our simulation the ground state is dominated by octet interpolators of the first and third Dirac structure, which agrees with a quark model calculation [206]. In contrast to the quark model, in our simulation the first excitation is dominated by singlet interpolators of the first Dirac structure, and the second and third excitation are again dominated by octet interpolators.

$\mathbf{\Lambda}$: $\mathbf{I(J^P) = 0(1/2^-)}$: The Λ spin $1/2^-$ channel is highly interesing for several reasons. First, the experimental $\Lambda(1405)^{****}$ marks the lowest energy level among all negative parity baryons. So far, lattice simulations have problems to identify this

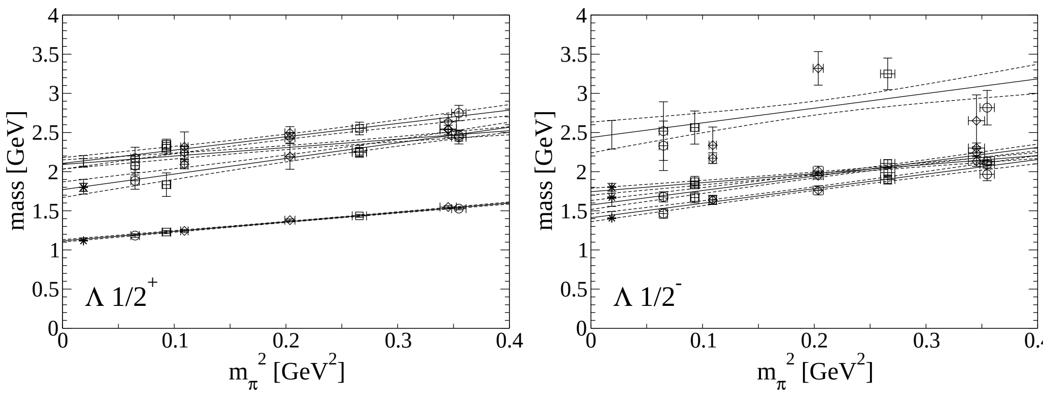

Figure 8.6: Energy levels for Λ spin $1/2$, positive (lhs) and negative parity (rhs).

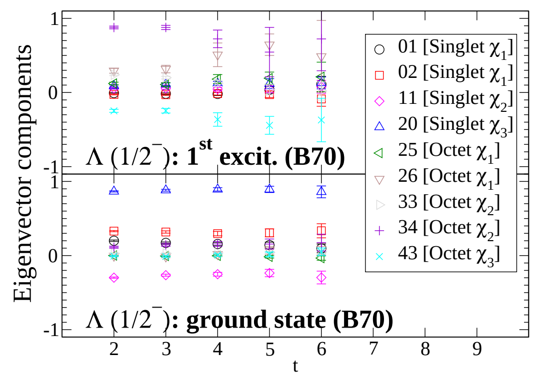

Figure 8.7: Eigenvectors for Λ spin $1/2^-$ ground state and first excitation for ensemble B70. The ground state is dominated by singlet χ_3 interpolators. The first and the second excitation are dominated by octet interpolators. We want to emphasize that small but non-negligible mixing of singlet and octet is observed.

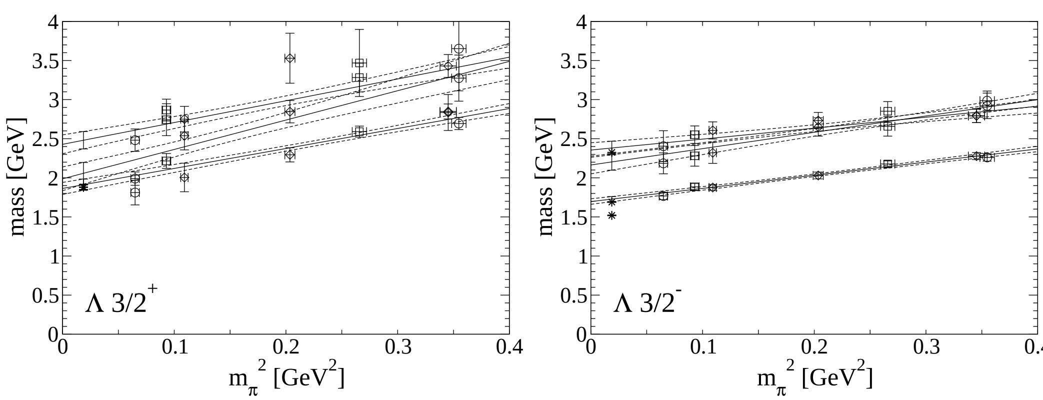

Figure 8.8: Energy levels for Λ spin $3/2$, positive (lhs) and negative parity (rhs).

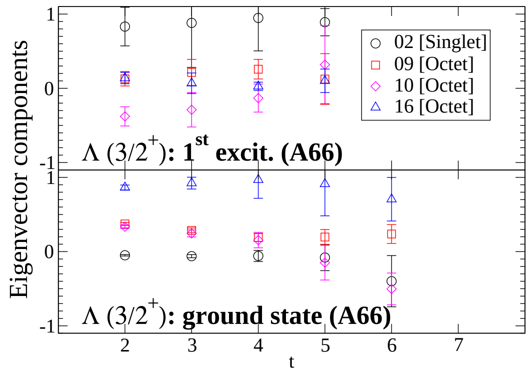

Figure 8.9: Eigenvectors for Λ spin $3/2^+$ ground state and first excitations for ensemble A66. We emphasize the domination of singlet interpolators for the first excitation. Such interpolators are non-vanishing only for broken Fierz identities, which is realized by the use of different quark smearing widths (see Section 4.3.4). Furthermore, we remark that small but non-negligible mixing of singlet and octet is observed.

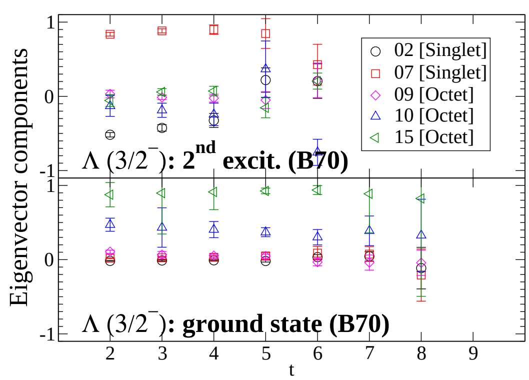

Figure 8.10: Eigenvectors for Λ spin $3/2^-$ ground state and second excitations for ensemble B70. We emphasize the domination of singlet interpolators for the second excitation. Such interpolators are non-vanishing only for broken Fierz identities, which is realized by the use of different quark smearing widths (see Section 4.3.4).

state (see, e.g., [60]), only one group claims to isolate it (see [207]). Furthermore, it is conjectured from Chiral Unitary Theory that it may have a double-pole structure (see, e.g., [7]). We apply different sets of interpolators and fit ranges and find some related deviation of the energy levels. We stress that our basis is large compared to other studies, in particular we include three types of Dirac structures for both singlet and octet interpolators. The analysis appears to be complicated because of nearby eigenvalues and early onsets of noise. Nevertheless, we can extract four energy levels, shown in Figure 8.6 for interpolators (2,3,10,18,26,27,34,42). We find that the ground state energy level agrees with the experimental $\Lambda(1405)^{****}$ within 1σ, a double-pole structure is not observed. The first and second excited energy level agree with the experimental $\Lambda(1670)^{****}$ and $\Lambda(1800)^{***}$, respectively. Note, however, the sizeable χ^2/d.o.f. of the chiral fits, larger than four (see Table D.5), indicating systematic effects which are not under control. We show the eigenvectors of the lowest two states in Figure 8.7 for ensembles B70 using interpolators (1,2,11,20,25,26,33,34,43). In our simulation, the ground state is dominated by singlet χ_3 interpolators, including some contribution from χ_2 and χ_1. The first and second excitation are dominated by octet interpolators, including contribution from all three Dirac structures. The singlet/octet level ordering agrees with quark model calculations [206]. The corresponding mixing is smaller in our simulation, however, it can be expected to increase towards physical pion masses. A more thorough discussion of this channel, considering different interpolators and fit ranges and finite volume effects will be presented in a forthcoming publication.

$\mathbf{\Lambda}$: $\mathbf{I(J^P) = 0(3/2^+)}$: In the Λ spin $3/2^+$ channel, the Particle Data Group lists only one resonance, $\Lambda(1890)^{****}$. For symmetric quark fields, singlet interpolators vanish exactly due Fierz identities. We use different quark smearing widths in order to invalidate the Fierz identities and construct singlet interpolators nevertheless, as discussed in Section 4.3.4. We use interpolators (2,9,10,16), including singlet and octet, to extract three states.

Analyzing the eigenvectors, we find that the level ordering is not the same in all ensembles. We trace the eigenvectors along the different ensembles to perform a chiral fit of all three states, and name them according to their ordering at the physical point. The extrapolation of the ground state hits the experimental $\Lambda(1890)^{****}$ nicely (see Figure 8.8). Within the finite basis used, this state is dominated by octet interpolators. We show the eigenvectors of the ground state and the first excitation of ensemble A66 in Figure 8.9. The first excitation shows a strong chiral slope, approaching the ground state energy level towards physical quark masses. The corresponding χ^2/d.o.f. of the chiral fit is larger than four (see Table D.4). The eigenvectors indicate a non-negligible mixing of singlet and octet interpolators at our lightest pion mass. Such mixing effects can increase towards lighter pion masses, complicating the functional dependence on m_π^2. This is a possible origin of the large χ^2/d.o.f. Assuming an enhanced chiral curvature towards physical quark masses, our data are also compatible with a picture of level crossing of the two lowest states. This would imply a singlet ground state in this channel. The second excitation lies a bit higher and is dominated by octet interpolators, including small singlet contributions. Finally we want to emphasize the importance of singlet interpolators for the low lying states in this channel, even though those interpolators are vanishing exactly for symmetric point-like quark fields.

$\mathbf{\Lambda}$: $\mathbf{I(J^P) = 0(3/2^-)}$: In the negative parity channel, the resonances $\Lambda(1520)^{****}$, $\Lambda(1690)^{****}$ and $\Lambda(2325)^{*}$ are known experimentally, where the first two are established. We use interpolators (2,9,10,16), including singlet and octet, to extract three states (see Figure 8.8). The level ordering differs in some of the ensembles, and, again, tracing of the eigenvectors defines the chiral fit for all three states, named according to their ordering at the physical point. We find fairly stable signals and χ^2/d.o.f. of the chiral fits of order one (see Table D.5), encouraging the chosen assignment of the states. The extrapolation of the ground state energy level is compatible with the $\Lambda(1690)^{****}$, and both excitations extrapolate to the $\Lambda(2325)^{*}$. A possible reason for the mismatch with the experimental ground state would be that the used interpolators do not couple strongly enough to this state, such that it is effectively hidden from our simulation. On the other hand, mixing of singlet and octet may increase towards physical quark masses, inducing a non-linear dependence on m_π^2. With a significant chiral bending down, the obtained energy levels could reproduce the experimental ones. We show the eigenvectors of ensemble B70 in Figure 8.10. The two lowest states are dominated by octet, the second excitation by singlet interpolators. Some mixing of singlet and octet is found in particular for the two excitations. This singlet/octet level ordering is in contrast to quark models which predict a singlet dominance for the ground state [206].

8.2.2 Sigma Baryons

$\mathbf{\Sigma}$: $\mathbf{I(J^P) = 1(1/2^+)}$: The $\Sigma(1189)^{****}$ ground state marks one of the lowest energy levels of the spin 1/2 baryons. At the SU(3) flavor symmetric point, the octet and decuplet irreducible representations are orthogonal. Towards physical quark masses, $SU(3)_f$ is broken and hence octet and decuplet are allowed to mix. We use the set (1,2,9,10,25,26), which includes octet with Dirac structures χ_1 and χ_2 and decuplet interpolators in the basis. Four states can be extracted from our simulations. The ground state signal is fairly good and the chiral extrapolation arrives very close to the experimental $\Sigma(1189)^{****}$ (see Figure 8.11). The first excitation comes out too high compared to the experimental $\Sigma(1660)^{***}$. The energy levels of the second and third excitations appear close to the first excitation in our simulations. Note the poor χ^2/d.o.f. of the chiral fit of the second excitation, being larger than four (see Table D.4), which suggests a non-linear dependence on m_π^2.

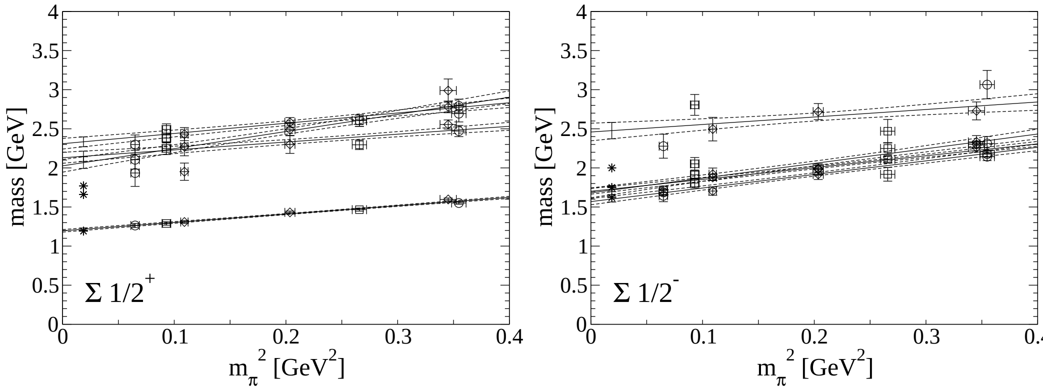

Figure 8.11: Energy levels for Σ spin 1/2, positive (lhs) and negative parity (rhs).

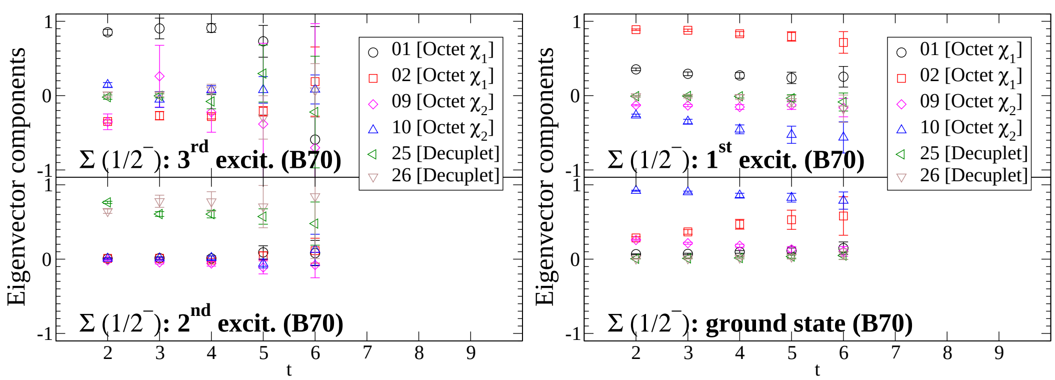

Figure 8.12: Eigenvectors for Σ spin $1/2^-$ ground state and first excitation (lhs) and second and third excitation (rhs) for ensemble B70. Note the dominance of decuplet interpolators for the second excitation, which is a low lying state (see Figure 8.11). Details are discussed in the text.

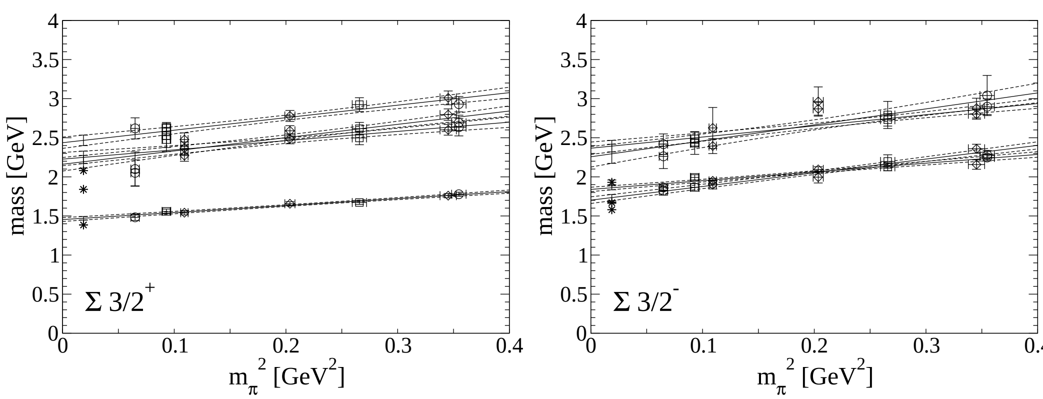

Figure 8.13: Energy levels for Σ spin 3/2, positive (lhs) and negative parity (rhs).

Monitoring the eigenvectors, we analyze the octet/decuplet content of the states. Within the finite basis employed, the ground state and the first excitation are strongly dominated by octet χ_1. Of the second and third excitation, one is dominated by decuplet and the other one by octet χ_2 interpolators. The mixing of octet and decuplet interpolators is found to be negligible in the range of pion masses considered. As we will see, this holds for most Σ and Ξ observables discussed in this work.

$\boldsymbol{\Sigma}$: $\mathbf{I(J^P) = 1(1/2^-)}$: In the Σ spin 1/2 negative parity channel, the Particle Data Group lists two low nearby states, $\Sigma(1620)^{**}$ and $\Sigma(1750)^{***}$, and one higher lying resonance, the $\Sigma(2000)^{*}$. Of those, only $\Sigma(1750)^{***}$ is established. Again the set of interpolators (1,2,9,10,25,26) is used to extract four states from our simulations. We find three low nearby states, all of which extrapolate close to the experimental $\Sigma(1620)^{**}$ and $\Sigma(1750)^{***}$ (see Figure 8.11). Hence, our results confirm the $\Sigma(1620)^{**}$ and $\Sigma(1750)^{***}$ and even suggest the existence of a third low lying resonance. Note, however, that there may be significant contribution from the $N\bar{K}$ scattering state. The eigenvectors of all four states are shown for ensemble B70 in Figure 8.12. Within the employed basis, the ground state is dominated by octet χ_2, the first excitation by octet χ_1, the second excitation by decuplet and the third excitation by octet χ_1 interpolators. We want to emphasize the existence of a low lying state in this channel which is dominated by decuplet interpolators. This result also agrees with a quark model calculation [206]. Again, the mixing of octet and decuplet interpolators appears to be negligible in the range of pion masses considered.

$\boldsymbol{\Sigma}$: $\mathbf{I(J^P) = 1(3/2^+)}$: The Particle Data Group lists $\Sigma(1385)^{****}$, $\Sigma(1840)^{*}$ and $\Sigma(2080^{**})$, where only the lighter one is established. We use interpolators (2,3,10,11,12) to extract four energy levels (see Figure 8.13). The chiral extrapolations come out a bit high compared to the experimental values. Investigating the eigenvectors, we find that the lowest two states are strongly dominated by decuplet, the second excitation by octet and the third excitation again by decuplet interpolators.

$\boldsymbol{\Sigma}$: $\mathbf{I(J^P) = 1(3/2^-)}$: In this channel, $\Sigma(1580)^{*}$, $\Sigma(1670)^{****}$ and $\Sigma(1940)^{***}$ are known experimentally, where the lightest one needs confirmation. Using interpolators (2,3,10,11,12) we can extract four states. We find two low lying states and two higher excitations (see Figure 8.13). In general, the corresponding energy levels are high compared to experiment, thus not confirming the $\Sigma(1580)^{*}$. However, the mixing of octet and decuplet might increase towards light pion masses, complicating the chiral extrapolation. Analyzing the eigenvectors, we find that of the two low lying states, one is dominated by octet and the other one by decuplet interpolators. Also, of the third and fourth state, one is dominated by octet and the other one by decuplet interpolators. Compared to the other Σ channels, there appears a measurable mixing of octet and decuplet interpolators. We remark the importance of

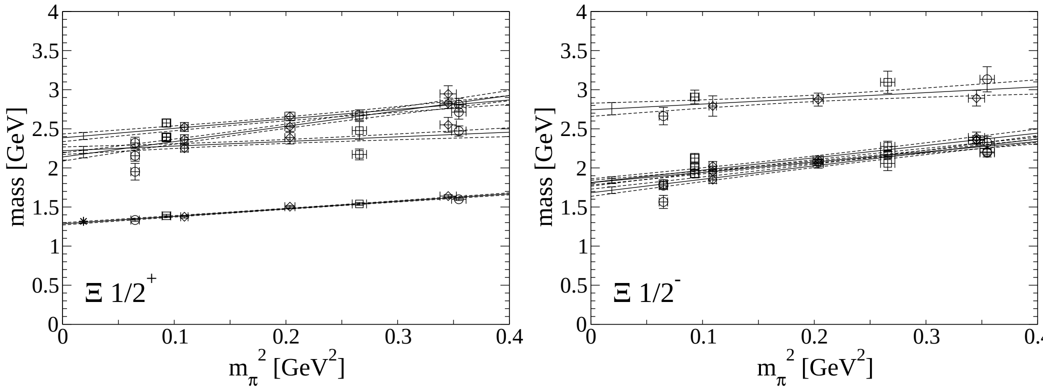

Figure 8.14: Energy levels for Ξ spin 1/2, positive (lhs) and negative parity (rhs).

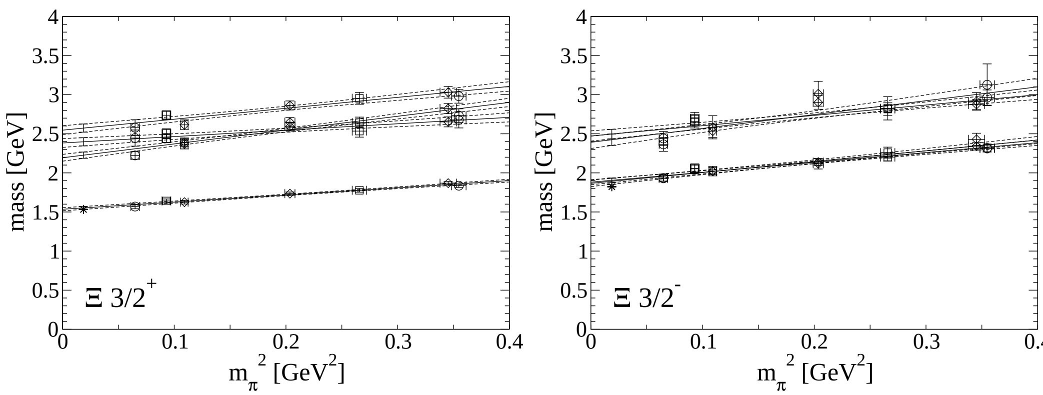

Figure 8.15: Energy levels for Ξ spin 3/2, positive (lhs) and negative parity (rhs).

decuplet interpolators for low-lying states in this channel, which is in contrast to quark model calculations [206].

8.2.3 Xi Baryons

$\mathbf{\Xi}$: $\mathbf{I(J^P) = 1/2(1/2^+)}$: Experimentally, only one resonance $\Xi(1322)^{****}$ is known in the Ξ spin $1/2^+$ channel. We use interpolators (1,2,9,10,25,26) to extract four states. The ground state shows a fairly clean signal and its chiral extrapolation hits nicely the $\Xi(1322)^{****}$ (see Figure 8.14). The three excitations come out much higher, where the results at the lightest pion mass suggest a significant chiral curvature towards physical pion masses. This is also expressed in the poor χ^2/d.o.f., which is larger than five for the second excitation (see Table D.4). Analyzing the eigenvectors, we find that within the finite basis used the ground state and the first

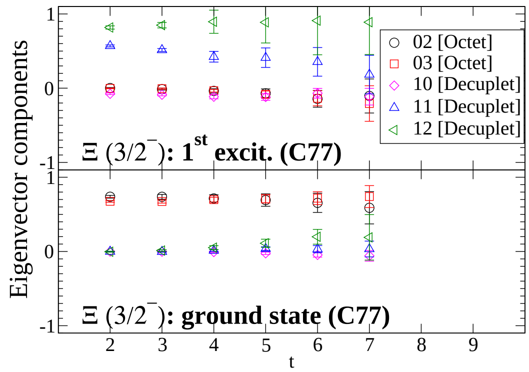

Figure 8.16: Eigenvectors for Ξ spin $3/2^-$ ground state and first excitation are shown for ensemble C77. Note the non-negligible mixing of octet and decuplet interpolators. Details are discussed in the text.

excitation are strongly dominated by octet χ_1. Of the third and the fourth excitation, one is dominated by decuplet and the other one by octet χ_2 interpolators. The mixing of octet and decuplet interpolators is found negligible in the range of simulated pion masses.

Ξ : $\mathbf{I(J^P) = 1/2(1/2^-)}$: No state is known in the Ξ spin $1/2^-$ channel experimentally, and no low-lying state identified in quark models, either [206]. Nevertheless, using interpolators (1,2,9,10,25,26), we find a total of four states in our simulations (see Figure 8.14). Of those, three are low lying and extrapolate to 1.7-1.9 GeV. Note the poor χ^2/d.o.f. larger than three of the corresponding three chiral extrapolations (see Table D.5). The fourth state appears rather high at 2.7-2.9 GeV, but shows a nice χ^2/d.o.f. of order one. The eigenvectors tell that the ground state is dominated by octet χ_2, the first excitation by octet χ_1, the second excitation by decuplet and the third excitation again by octet χ_1 interpolators. We emphasize the existence of a low lying state in this channel which is dominated by decuplet interpolators, analogous to the Σ spin 1/2 negative parity channel.

Ξ : $\mathbf{I(J^P) = 1/2(3/2^+)}$: In this channel, one state, Ξ(1530)****, is experimentally known and well established. We use interpolators (2,3,10,11,12) to extract four states from our simulation. All four states show a stable signal, and the ground state energy level nicely extrapolates to the experimental Ξ(1530)**** (see Figure 8.15). The second and third energy levels appear to be rather close to each other and are compatible with a level crossing picture within pion masses of 300 to 500 MeV. Within the finite basis used, the ground state is dominated by decuplet interpolators, which agrees with quark model calculations [206]. At light pion masses, the first

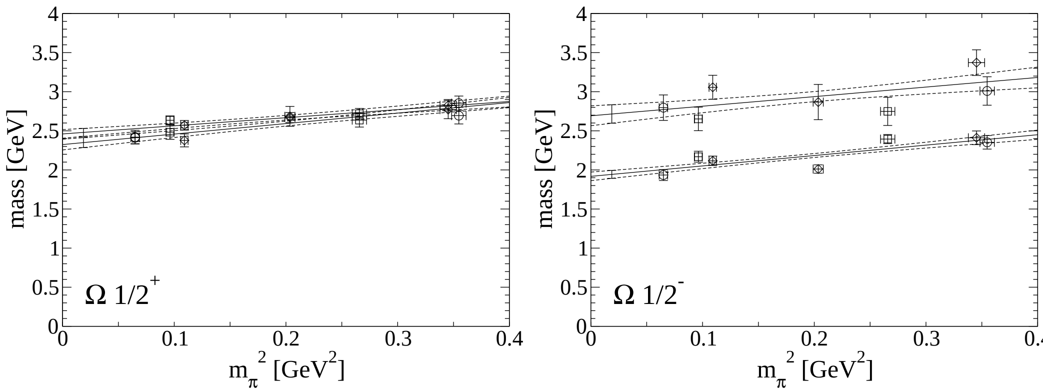

Figure 8.17: Energy levels for Ω spin 1/2, positive (lhs) and negative parity (rhs).

excitation is dominated by octet and the second by decuplet interpolators. The third excitation is again dominated by decuplet interpolators.

$\mathbf{\Xi}$: $\mathbf{I(J^P) = 1/2(3/2^-)}$: The Particle Data Group lists one state, $\Xi(1820)^{***}$, which is expected to be dominated by octet interpolators according to quark model calculations [206]. Using interpolators (2,3,10,11,12), we extract four energy levels in this channel. We find two low lying states, the energy levels of which extrapolate close to the experimental $\Xi(1820)^{***}$ (see Figure 8.15). Analyzing the eigenvectors, we find that of the two low lying states, one is dominated by octet and the other one by decuplet interpolators. The third state is dominated by octet and the fourth state by decuplet interpolators. Compared to the other Ξ channels, there appears a measurable mixing of octet and decuplet interpolators. We show the eigenvectors of the two low lying states in Figure 8.16.

8.2.4 Omega Baryons

$\mathbf{\Omega}$: $\mathbf{I(J^P) = 0(1/2^+)}$: Experimentally, the Ω baryons have been investigated only roughly. No state is identified in the Ω spin $1/2^+$ channel. Using the interpolators (1,4,5), the same as in the corresponding Δ channel, we find two states, whose energy levels are close for all simulated pion masses (see Figure 8.17). Both predicted resonances lie in the region of 2.2 to 2.6 GeV, where systematic effects are neglected.

$\mathbf{\Omega}$: $\mathbf{I(J^P) = 0(1/2^-)}$: Again, there is no experimental experience in the spin $1/2^+$ channel of the Ω baryons. We extract two states, where the excitation comes with some noise. The chiral extrapolation of the ground state predicts a resonance around 2 GeV (see Figure 8.17), systematics not considered. Note the corresponding poor

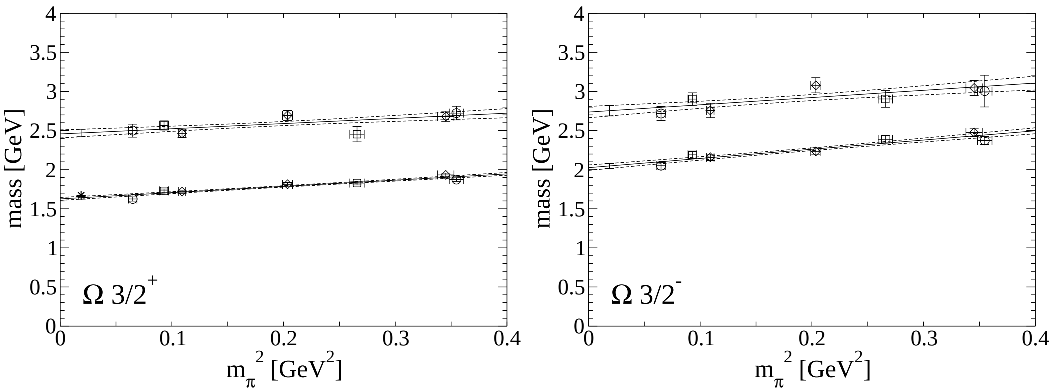

Figure 8.18: Energy levels for Ω spin 3/2, positive (lhs) and negative parity (rhs).

χ^2/d.o.f., larger than four (see Table D.5). The main contribution stems from the light energy level of ensemble C72. Since this behavior is not systematically observed in other channels, we assume the deviation to be due to statistical fluctuations.

$\mathbf{\Omega}$: $\mathbf{I(J^P) = 0(3/2^+)}$: The $\Omega(1672)^{****}$ is known experimentally to very high accuracy. This is one of the reasons why this state is often used to define the strange quark mass parameters. This path is also pursued in our setup. However, the determination of the parameters has been performed along a different scheme of scale setting. Thus, the results shown here for the ground state serve as an additional cross check for the final setup of the simulation. The ground state energy level extrapolates close to the experimental $\Omega(1672)^{****}$, but undershoots it slightly (see Figure 8.18). The corresponding χ^2/d.o.f. is around two (see Table D.4). Half of it is contributed by ensemble A66. Comparing to other observables including valence strange quarks, we find that indeed the strange quark mass of ensemble A66 could be slightly too light. However, a thorough discussion is difficult since also other systematics enter. We will provide some further discussion including finite volume effects in Chapter 9.

$\mathbf{\Omega}$: $\mathbf{I(J^P) = 0(3/2^-)}$: There is no experimental experience in the Ω spin $3/2^-$ channel. We find two states, both with a fairly good signal, in our simulations. The chiral extrapolation of the ground state energy level predicts a resonance slightly above 2 GeV (see Figure 8.18).

8.3 Summary of the Results for the Baryon Spectrum

In this chapter, the results for the baryon spectrum from our simulation have been presented. Figure 8.19 shows the results after extrapolation to physical pion masses

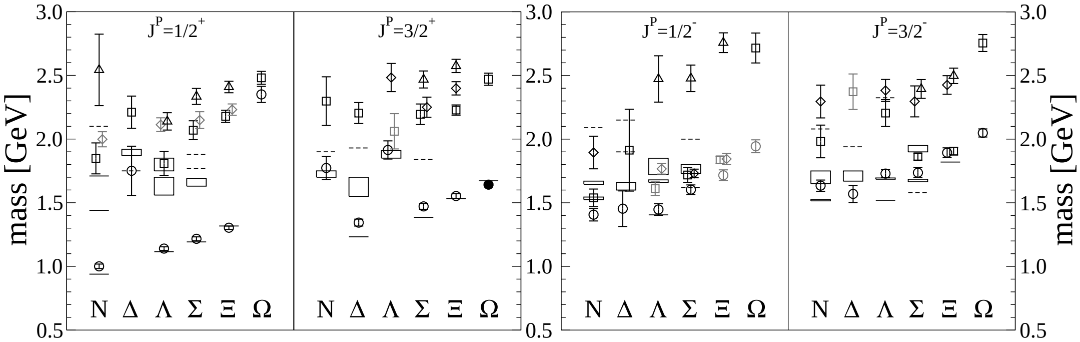

Figure 8.19: Energy levels for positive parity (lhs) and negative parity baryons (rhs). All values are obtained by chiral extrapolation linear in the pion mass squared. Horizontal lines or boxes represent experimentally known states, dashed lines indicate poor evidence, according to [7]. The statistical uncertainty of our results is indicated by bands of 1σ, that of the experimental values by boxes of 1σ. The strange quarks are implemented in the partial quenching approximation. Grey symbols denote a poor χ^2/d.o.f. of the chiral fits (see Tables D.4 and D.5).

compared to experimental values [7]. In general, the results are in good agreement with experiment. As an example, our result for the ground state in the Λ spin $1/2^-$ channel is compatible with the experimental $\Lambda(1405)^{****}$. However, we find that the excitations appear fairly high, in particular in positive parity channels. Finite volume effects on one hand and scattering states on the other hand could be the underlying reasons for the deviations from experiment. Both and other types of systematic effects will be partly addressed in Chapter 9.

Fierz identities impose restrictions on the basis of interpolators. In some specific channels, these identities force point-like interpolators to vanish exactly. In Section 4.3.4 we showed that interpolators can be constructed nevertheless. These interpolators are used in particular for the Δ spin 1/2 and the Λ singlet spin 3/2 channels.

Using the variational analysis, we investigated the singlet/octet content of the low-lying Λ channels and find an increasing mixing towards physical pion masses. Furthermore, we find that singlet interpolators couple strongly to the low-lying Λ spin 3/2 channels, which is impressive in view of their vanishing for point-like quarks due to Fierz identities. The Σ and Ξ channels have been investigated with respect to their octet/decuplet content. In general, the mixing is found to be essentially negligible in the range of pion masses considered. A bit surprisingly, in both the Σ and Ξ spin $1/2^-$ channels, three near-by low-lying states appear in our simulation. In each channel, one of those three states is dominated by decuplet interpolators. Our results thus suggest that decuplet interpolators are important also for the low-lying spin 1/2 spectrum.

Chapter 9

Finite Volume and Other Systematic Effects

This chapter discusses finite volume and other systematic effects of our results. First, we give an overview of possible sources of systematic errors in Section 9.1. The theoretical background of finite volume effects is introduced in Section 9.2. Section 9.3 discusses a possible volume dependence of the scale setting scheme applied in this work. Then, finite volume effects of the meson and baryon spectrum are dealt with in Sections 9.4 and 9.5. Finally, we conclude on finite volume effects in Section 9.6.

9.1 Possible Sources of Systematic Errors

First of all, let us collect the possible sources of systematic errors encountered in this work.

- Discretization effects are not investigated quantitatively. They are assumed to be small, because of the improved action and smeared operators.

- The autocorrelation of the Monte Carlo data is not analyzed rigorously due to limited statistics. However, we observe frequent tunneling of the topological charge, indicating a fairly small autocorrelation of the Markov chain.

- The simulation includes only two light sea quarks. If the effect of the dynamical strange quark on the scale setting is similar as on other observables, the effect could cancel out approximately in dimensionful predictions.

- Isospin breaking and electroweak corrections (and gravitation) are assumed to be negligible at the statistical accuracy available in this work.

- The dependence of hadron energy levels on the pion mass squared is in general non-linear, in contrast to the fit form used. This might become important in particular in case of enhanced mixing of operators and avoided level crossings towards physical quark masses. We discuss this point for observables where such effects are expected.

- In the previous chapters, the spectrum of the QCD Hamiltonian in a box with a linear size of approximately $L_s = 2.2$ fm was discussed. In this chapter, we will investigate the finite volume effects and extrapolate to infinite volume.

- With respect to the actual full basis, only a small set of one-particle interpolators is used. If the overlap with physical states is weak, the asymptotic region of the eigenvalues is covered by noise. This is expected to hold in particular for "two-particle states", which are not identified in this work. In addition to the choice of interpolators, also the value of t_0 in the variational analysis and the chosen fit range systematically enter the predictions. This is partly addressed in this chapter together with the discussion of finite volume effects. In particular for the excited states, the signal dives into noise early, and thus the visible part of the asymptotic region of the eigenvalues is rather short. For single ensembles it is then hard to judge if there is really a (one) physical state associated with the exponential behavior seen in the eigenvalues. At this point we benefit strongly from the total of ten independent ensembles. We interpret to observe a signal of a physical state if the signal is consistent in most of the ensembles.

- Spin is not a good quantum number on the lattice. However, the used interpolators are constructed to have overlap predominantly with only one spin channel in the continuum limit. Possible mixing with other spin channels is discussed whenever it is expected to be non-negligible.

- Finally, deviations of the used experimental value of the Sommer parameter, $r_{0,\mathrm{exp}} = 0.48$ fm, enter linearly all dimensionful quantities calculated in this work. The value is expected to lie within $0.46 \text{ fm} \leq r_{0,\mathrm{exp}} \leq 0.50$ fm, which implies a region of uncertainty of 4% for all dimensionful observables.

9.2 Finite Volume Generalities

Resonance properties were briefly accounted for in Section 4.4.2. For bound states in large volumes, there are two leading mechanisms of finite volume effects. Firstly, the spectral density of scattering states depends on the volume and distorts the bound state spectrum through avoided level crossings. This mechanism is very important towards very large volumes and also for the determination of resonance properties [97, 99]. However, the volumes used in the present work allow only for a low spectral density of scattering states in the low energy spectrum. This kind of finite volume effect is thus discussed only qualitatively for particular observables. Secondly, a virtual pion cloud exchange with the mirror image, a so-called "pion wrapping around the universe" causes an exponential correction to the energy level of the hadron [173]. This mechanism can be discussed to higher orders in Chiral

Perturbation Theory [181,182]. Here we follow a fit form successfully applied in [198],

$$E_h(L) = E_h(L = \infty) + c_h(m_\pi)\mathrm{e}^{-m_\pi L}(m_\pi L)^{-3/2} \;, \qquad (9.1)$$

where E_h is the energy level of the hadron at linear size L of the lattice. It was suggested that $c_h(m_\pi) = c_{h,0} m_\pi^2$, which implies two fit parameters for each observable: $E_h(L = \infty)$ and $c_{h,0}$. The parameter $c_{h,0}$ is shared among different ensembles, which we exploit to make combined fits. We remark that the fit form used is a fairly simple one, however, considering the small number of different volumes, we have to rely on a fit form which uses only few parameters. Other fit forms are assumed to yield compatible results within statistical uncertainty.

Due to the exponential behavior, finite volume effects are expected to become non-negligible for $m_\pi L \lesssim 4$. This region is entered in particular towards small pion masses. Eq. (9.1) is valid only for asymptotically large volumes, power-like corrections are expected for $m_\pi L \lesssim 3$ and already earlier for higher excitations. We generated a larger volume for set A66 and a smaller and a larger volume for C77. All these ensembles show $2.7 < m_\pi L < 4$, where the pion cloud exchange should have a measurable effect described by Eq. (9.1). To discuss finite volume effects, we apply Eq. (9.1) separately to each observable. The data of sets A66 and C77 are used to perform a combined fit, and the resulting parameters are used to extrapolate the data of all ensembles (for that observable) to infinite volume. Finally, the results are extrapolated to the physical point.

9.3 Volume Dependence of the Scale Setting

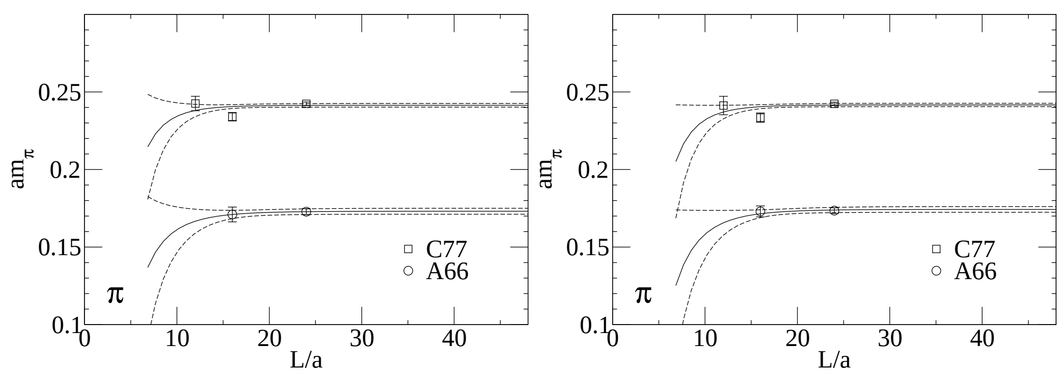

Figure 9.1: Volume dependence of the pion mass. Left hand side results of interpolator 1, right hand side results of interpolator 4 shown. In both cases, the fit range for the eigenvalues starts at $t = 6a$.

The scale enters all dimensionful observables, thus we first focus on finite volume effects of the scale. The procedure to set the scale chosen in this work makes use

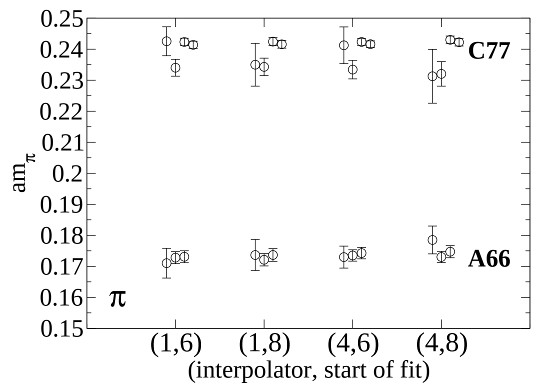

Figure 9.2: Systematic error of the pion mass. We show the dimensionless pion mass am_π for different choices of interpolators and fit ranges, labelled on the x-axis. E.g., (1,6) denotes interpolator 1 and a fit range for the eigenvalues from $t = 6a$ to the onset of noise. For each set of interpolator and fit range, results for small to large lattices are shown from left to right, the corresponding infinite volume limit rightmost. The volume extrapolation is always performed using a combined fit for the A66 and C77 data.

of the Sommer parameter and the pion mass. We discuss finite volume effects and other possible systematic influence on these two observables and finally the impact on the overall scale.

The pion mass is expected to follow a volume dependence according to Eq. (9.1). However, our data do not show a clear volume dependence at all. In Figure 9.1, we show the volume fit for sets A66 and C77 for interpolator (1) (lhs) and (4) (rhs). In both cases, the combined fit yields a small but negative coefficient for the extrapolation, which means an increase in mass towards infinite volume. This behavior is in contradiction to any expectation from theory. In order to remove other possible sources of systematic errors, we consider different interpolators and fit ranges for the eigenvalues. Some of the corresponding results are shown in Figure 9.2. For each set of interpolator and fit range, results for small to large lattices are shown from left to right, and the corresponding infinite volume extrapolation is found rightmost. For set A66, the results from the two volumes are compatible in all cases. For set C77, the result from the $L_s = 16a$ ensemble lies systematically below the values of the other two ensembles with smaller and larger volumes. The deviation is around three percent, translating into roughly 1% for $(am_\pi)^2$, which enters the scale setting procedure and any chiral extrapolation. This low value is apparently responsible for the negative coefficient of the volume fit. However, even if we exclude this point, the volume dependence is still very flat. Furthermore, the results in the infinite volume limit are fairly independent of the choice of interpolators and fit ranges.

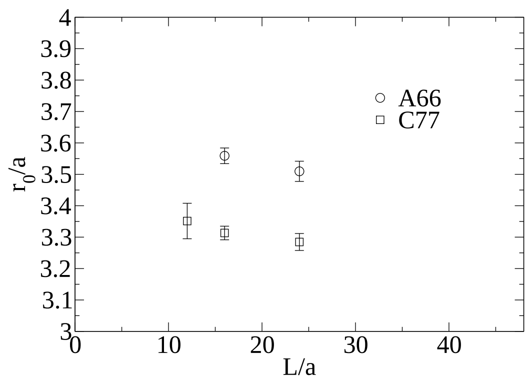

Figure 9.3: The Sommer parameter r_0/a versus the linear size of the lattice L/a. The data would be compatible with a decrease of the Sommer parameter towards infinite volume. However, we follow the expectation from theory and assume a flat volume dependence.

Before concluding on the effects of the pion mass on the scale, we briefly comment also on the volume dependence of the Sommer parameter. The Sommer parameter characterizes the static quark potential at intermediate scales ($\approx$ 0.5 fm). It is calculated using Wilson loops, excluding explicitely contractions with mirror images from the (anti)periodic boundary conditions. For these reasons, it is expected to be fairly independent of the volume. We show the results for r_0/a for the ensembles with different volumes of the sets A66 and C77 in Figure 9.3. The results would be compatible with a decrease towards infinite volume, however, due to the reasons given above, we assume a flat volume dependence in the region considered.

Now we want the discuss the effect on the scale. In any case, we assume the Sommer parameter to be independent of the volume. In order to estimate the systematic error, we consider two different scenarios. First, we assume the pion mass to be independent of the volume, which is compatible with our results. In this case, we simply augment the fit of Figure 6.1 with the results for the ensembles with other volumes, shown in Figure 9.4, left hand side. In the second scenario, we extrapolate the pion mass to infinite volume, using for definiteness the data of Figure 9.1, left hand side. The corresponding Sommer parameter is given by the average over the ensembles with different volumes. The resulting fit of scenario two is shown in Figure 9.4, right hand side. We find that the resulting scales of the two scenarios are in surprisingly good agreement and furthermore also agree with the scale determined from $L_s = 16a$ data only (see Figure 6.1). In order to simplify the setup of the simulation, we thus continue to use the scale determined in Section 6.1 also for ensembles with other volumes. Note that the introduced systematic error estimated from the choice of interpolators, fit range for the eigenvalues and the volume extrapolation is in the magnitude of the statistical error. Since in general

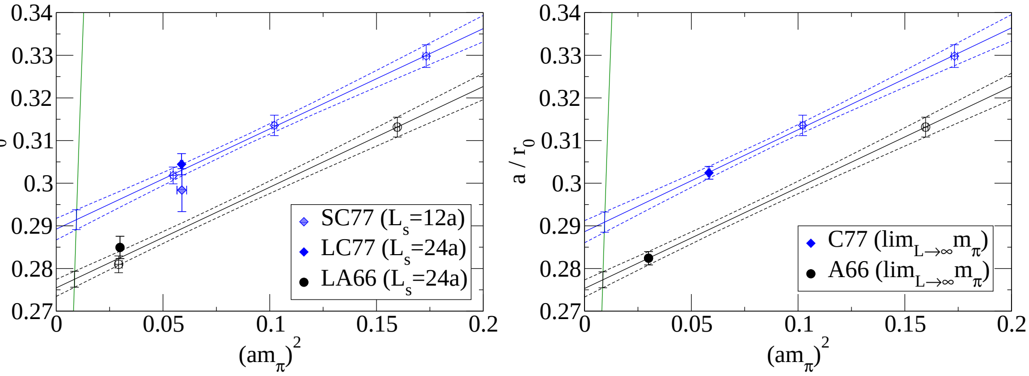

Figure 9.4: Setting the scale in the infinite volume limit. Lhs: Figure 6.1 is augmented with data from ensembles of different volumes for sets A66 and C77. The Sommer parameter and the pion mass are assumed to be independent of the volume. Rhs: Here, the pion masses of A66 and C77 are extrapolated to infinite volume following Figure 9.1 (lhs). In both scenarios the scale obtained is in good agreement with the scale obtained solely from $16^3 \times 32$ lattices, according to Section 6.1.

the impact of the statistical uncertainty of the scale on dimensionful observables is negligible compared to other sources of uncertainty, we conclude that this holds also for the impact of the systematic error.

In principle, the volume dependence of the strange quark mass parameter can be discussed in the same way. This would require only a volume analysis of the Ω spin $3/2^+$ ground state energy level. However, we prefer to discuss several observables which include strange valence quarks, and conlude on the strange quark mass parameter only afterwards.

9.4 Volume Dependence of Meson Energy Levels

In this section, we discuss finite volume effects of the meson energy levels. A systematic discussion requires a good signal and also at least partly control over other systematic errors. Many observables, in particular excited energy levels, show a fairly weak signal. As a consequence, the fit range is usually short, and hence additional systematic effects are difficult to quantify. For these reasons, we focus on observables with a good signal where finite volume effects may be non-negligible. This is the case in particular for the ground states of pseudoscalar and vector meson channels. The pion was already discussed in Section 9.3. Now we investigate the strange mesons $K\,(0^-)$ and $K^*\,(1^-)$. We remark that only some of the systematic errors are discussed and that there may be other significant systematic errors as well, which become visible in particular for high statistical accuracy.

9.4.1 Strange Scalar Mesons

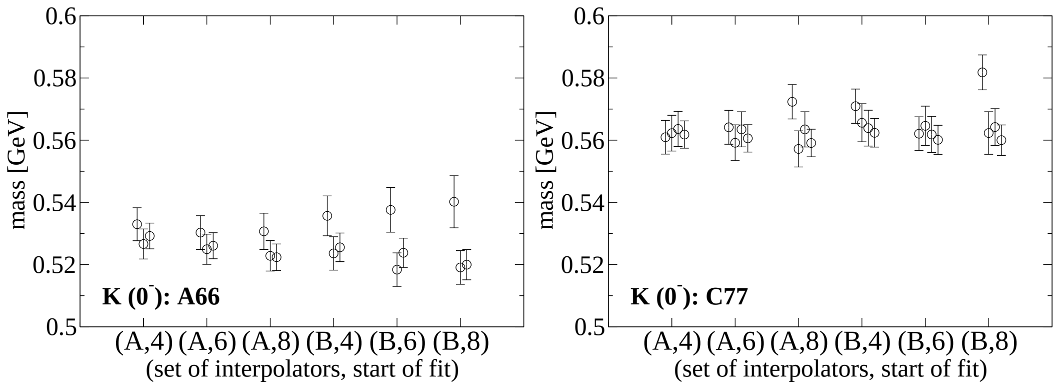

Figure 9.5: Systematic error of the strange meson $K\,(0^-)$ mass, analogous to Figure 9.2. "A" denotes interpolator (1), "B" denotes (4). For each set of interpolator and fit range, results for small to large lattices are shown from left to right, the corresponding infinite volume limit rightmost.

Our result for the $K\,(0^-)$ ground state energy level in the finite box of roughly 2.2 fm is a bit higher than the experimental Kaon around 495 MeV (see Figure 7.7). We apply different sets of interpolators and fit ranges for the eigenvalues in order to estimate the corresponding systematic error. We show results and infinite volume extrapolations for interpolators A=(1) and B=(4) and different fit ranges in Figure 9.5. The overall picture matches the expectation. The energy level becomes lighter towards larger volume and partly also towards later starting points for the fit of the eigenvalues. The results of the small lattices tend to become unstable towards late starting points of the fit, if the fit range becomes too short. Except for those understood discrepancies, the deviations associated with different interpolators and different fit ranges are well bounded and not larger than the statistical error.

We observe some small but non-negligible finite volume effects in set A66, but essentially none in set C77. For definiteness, we choose interpolator (1) and the fit range to start from $t_{\text{min}} = 6a$, and note that the corresponding systematic error is of the order of the statistical uncertainty. We use the fitted parameters of the volume dependence of sets A66 and C77 to extrapolate the results of all ensembles to infinite volume. Finally, we extrapolate to the physical point, shown in Figure 9.6. We obtain m_K=504(4) MeV, which is very close to the experimental Kaon. However, the deviation is larger than the statistical uncertainty. The χ^2/d.o.f. of the chiral fit is larger than four, similar as for the fit in the finite box. This is possibly related to the choice of the strange quark mass parameter.

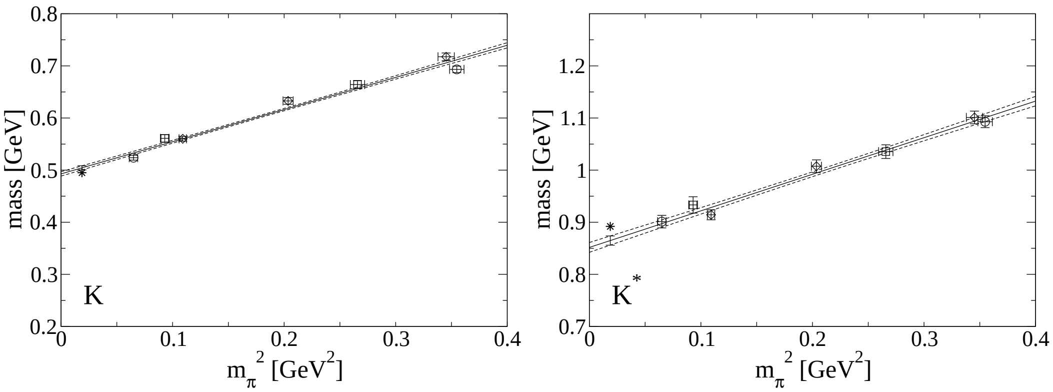

Figure 9.6: Energy levels for the strange mesons $m_K\,(0^-)$ (lhs) and $m_{K^*}\,(1^-)$ (rhs) in the infinite volume limit. After infinite volume extrapolation ((A,6) of Figure 9.5 resp. Figure 9.7), we extrapolate to physical pion masses. We obtain m_K=504(4) MeV and m_{K^*}=865(9) MeV, which are both compatible with experiment within few percent. Note, however, that the deviation is larger than the statistical uncertainty.

9.4.2 Strange Vector Mesons

We show the results and infinite volume extrapolations for $K^*\,(1^-)$ using interpolators A=(1,5) and B=(8) and different fit ranges in Figure 9.7. The finite volume effects appear to be much larger than for the $K\,(0^-)$ ground state. For definiteness, we choose interpolators (1,5) and $t_{\min} = 6a$, and note that the corresponding systematic error is similar to or somewhat smaller than the statistical uncertainty. Again, we use the fitted parameters of the volume dependence of sets A66 and C77 to extrapolate the results of all ensembles to infinite volume. The extrapolation to the physical point is shown in Figure 9.6. We obtain m_{K^*}=865(9) MeV, which deviates from the experimental K^* by about 2-3%. The χ^2/d.o.f. of the chiral fit improves a bit compared to the one in the finite box (see Table D.6).

9.5 Volume Dependence of Baryon Energy Levels

In this section, we discuss finite volume effects of the baryon energy levels. Again, we focus on observables with a good signal where non-negligible finite volume effects can be expected. This is the case in particular for the ground states of the positive parity baryon channels.

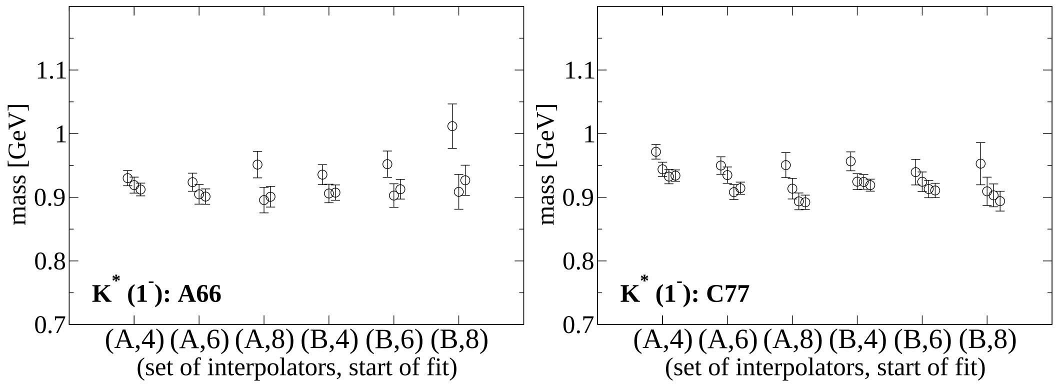

Figure 9.7: Systematic error of the strange meson K^* (1^-) mass, analogous to Figure 9.2. "A" denotes interpolators (1,5), "B" denotes (8). For each set of interpolator and fit range, results for small to large lattices are shown from left to right, the corresponding infinite volume limit rightmost.

9.5.1 Nucleon

The nucleon spin $1/2^+$ ground state shows a very clean signal. Our result for the finite box of roughly 2.2 fm deviates significantly from experiment (see Figure 8.1). We apply the sets of interpolators A=(1,2,9,10,19,20) and B=(3,4,10,11,19,20). Furthermore, we consider different starting values for the fit range for the eigenvalues. The results for the different ensembles and the corresponding infinite volume extrapolations are shown in Figure 9.8. Note that the result for (B,7) of ensemble A66 lies outside the plotted region. We conclude that for small volumes late starts of the fit have to be avoided.

We find a fairly strong dependence of the nucleon energy level on the lattice volume. For definiteness, we choose the set of interpolators A and $t_{\mathrm{min}} = 5a$ and the corresponding infinite volume extrapolation, which is shown explicitely in Figure 9.9. After infinite volume extrapolation of all ensembles with the extrapolation parameters for A66/C77, we extrapolate to the physical pion mass, shown in Figure 9.10 (lhs). Our final result is $m_N = 954(16)$ MeV, which hits the experimental $N(939)^{****}$ nicely within 1σ.

9.5.2 Delta Baryons

We show results and infinite volume extrapolations for different sets of interpolators and different fit ranges for the Δ spin $3/2^+$ ground state in Figure 9.11. Compared to the nucleon, the fit ranges of the eigenvalues are short, correspondingly, the results tend to fluctuate a bit more. The volume dependence appears to be the strongest of all observables considered. For definiteness, we choose the set of interpolators

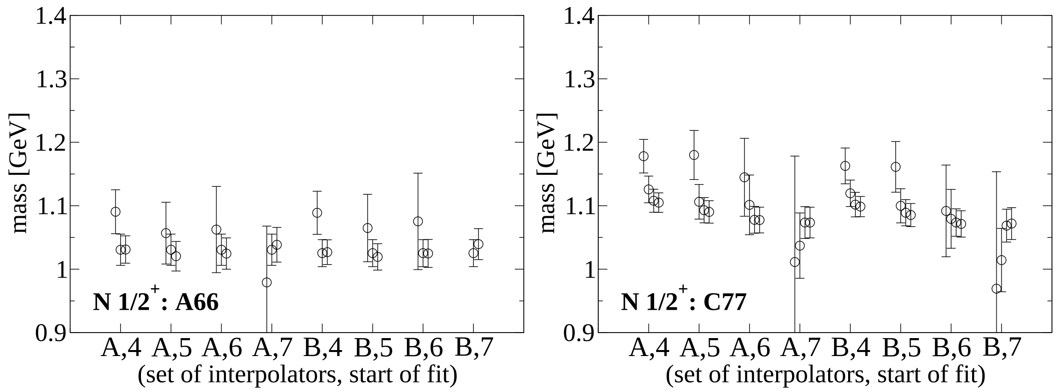

Figure 9.8: Systematic error of the nucleon mass, analogous to Figure 9.2. “A” denotes set of interpolators (1,2,9,10,19,20), “B” denotes (3,4,11,12,19,20). For each set of interpolator and fit range, results for small to large lattices are shown from left to right, the corresponding infinite volume limit rightmost.

A and $t_{\mathrm{min}} = 5a$ and the corresponding infinite volume extrapolation, and note that the systematic error of the order of the statistical error, or somewhat larger. After infinite volume extrapolation of all ensembles, we extrapolate to the physical pion mass, shown in Figure 9.10. Our final result is $m_\Delta = 1268(32)$ MeV, which hits the experimental $\Delta(1232)^{****}$ within roughly 1σ. We remark that the energy level appears low in ensemble A66 compared to other ensembles. This worsens the χ^2/d.o.f. of the chiral fit (see Table D.6), but improves the comparison with experiment.

9.5.3 Lambda Baryons

We show results and infinite volume extrapolations for different sets of interpolators and different fit ranges for the Λ spin $1/2^+$ ground state in Figure 9.12. For definiteness, we choose the set of interpolators A and $t_{\mathrm{min}} = 5a$ and the corresponding infinite volume extrapolation, and note that the systematic error is again of the order of the statistical error. After infinite volume extrapolation of all ensembles, we extrapolate to the physical pion mass, shown in Figure 9.13, left hand side. Our final result is $m_\Lambda = 1112(14)$ MeV, which hits the experimental $\Lambda(1116)^{****}$ nicely.

9.5.4 Sigma Baryons

In the Σ spin $1/2^+$ channel we apply the sets of interpolators A=(1,2,9,10,25,26) and B=(2,3,10,11,19,20,26,27) and different fit ranges to discuss the volume dependence of the ground state (see Figure 9.14). The volume dependence is found to be of comparable size like the one of the nucleon ground state energy level. Towards late

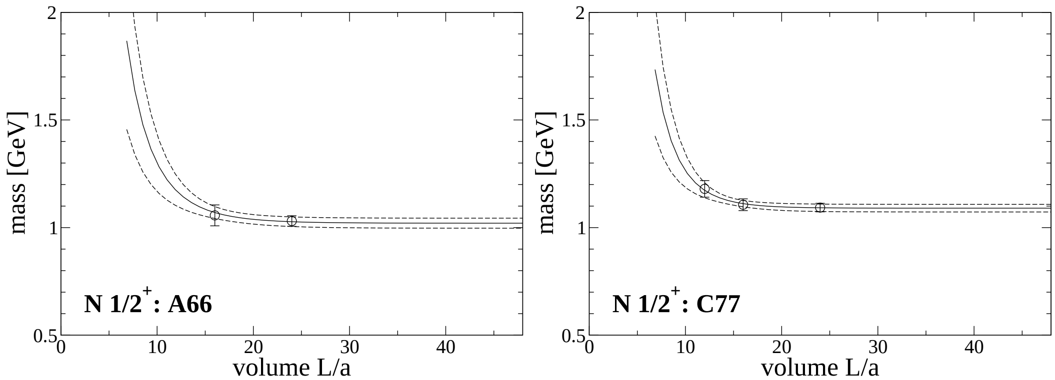

Figure 9.9: Volume dependence of the nucleon mass for the set of interpolators (1,2,9,10,19,20) and $t_{\min} = 5a$ ((A,5) of Figure 9.8).

fit ranges, the results start to scatter, nevertheless, the results are conclusive and the systematic error is of the order of the statistical one. We choose interpolators A and $t_{\min} = 6a$, and show the results in the infinite volume limit in Figure 9.13, right hand side. Our final result is $m_\Sigma = 1156(15)$ MeV, which deviates slightly from the experimental Σ around 1190 MeV. The χ^2/d.o.f. is of order two (see Table D.6), which is sizeable compared to the nucleon and Λ channels and possibly related to the mismatch with experiment.

9.5.5 Xi Baryons

We consider the sets of interpolators A=(1,2,9,10,25,26) and B=(2,3,10,11,19,20,26, 27) and different fit ranges to discuss the volume dependence of the Ξ spin $1/2^+$ ground state (see Figure 9.15). Again, the results are conclusive, and the systematic error is well bounded. We choose interpolators A and $t_{\min} = 6a$, and show the results for infinite volume in Figure 9.16, left hand side. Our final result is $m_\Xi = 1273(12)$ MeV, deviating from the experimental Ξ around 1317 MeV. Again, the discrepancy may be related to the χ^2/d.o.f. of order two (see Table D.6).

9.5.6 Omega Baryons

The Ω mass was used in the first place to define the strange quark mass parameter. We consider different sets of interpolators and fit ranges of the eigenvalues to estimate the corresponding systematic error. Figure 9.17 shows some of the corresponding results. Here, we choose for definiteness interpolators (1,3,4) and a fit range starting from $t_{\min} = 4a$, and note that the corresponding systematic error appears to be somewhat smaller than the statistical one. We extrapolate the energy levels of all ensembles to infinite volume and finally to the physical point, shown in

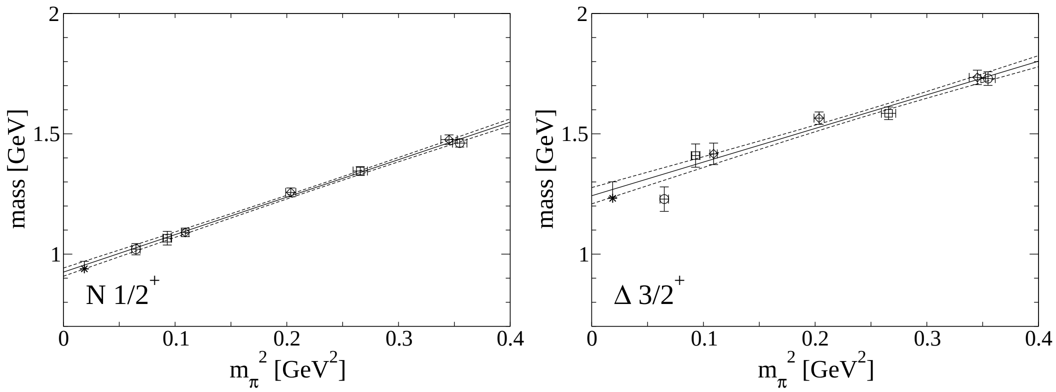

Figure 9.10: Energy levels for the nucleon spin $1/2^+$ (lhs) and Δ spin $3/2^+$ (rhs) in the infinite volume limit. After infinite volume extrapolation ((A,5) of Figure 9.8 resp. Figure 9.11), we extrapolate to physical pion masses. We obtain m_N=954(16) MeV and m_Δ=1268(32) MeV, which both match the experimental values within roughly 1σ.

Figure 9.16, right hand side. We obtain $m_\Omega = 1620(14)$ MeV, which deviates significantly from the experimental $\Omega(1672)^{****}$. Again, the discrepancy may be related to the χ^2/d.o.f. of order two (see Table D.6), and the issue of setting the strange quark mass through identification of m_Ω independently for each finite lattice.

9.6 Summary

In this chapter, we discussed systematic effects which may appear in our simulation. First, possible sources of systematic errors were collected and discussed in a qualitative manner. Then, we investigated quantitatively the volume dependence of the scale setting scheme applied in this work. We found very good agreement of the scale after infinite volume extrapolation with the scale defined in the finite box, using $16^3 \times 32$ lattices only. A bit surprisingly, the pion mass shows no clear volume dependence in our simulations.

For several observables, we discussed the dependence on the choice of interpolators, on the fit range for the eigenvalues and finally also on the volume. In general, the systematic error stemming from the choice of interpolators and the fit range is of the order of the statistical uncertainty, as long as sensible choices are made. The finite volume effects appear to be significant for nucleon, Δ and Σ, moderate for Λ, Ξ and $K^*(1^-)$, and fairly mild for Ω and $K(0^-)$ ground state energy levels in our simulation. We give an overview of the determined energy levels at physical pion masses in the infinite volume limit in Figure 9.18. We find that in particular the results for the nucleon, Δ and Λ ground state energy levels agree nicely with

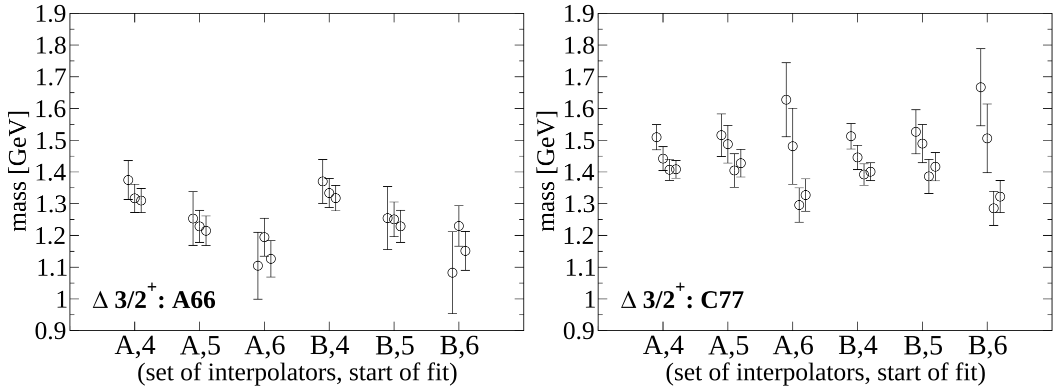

Figure 9.11: Systematic error of the Δ spin $3/2^+$ mass, analogous to Figure 9.2. "A" denotes set of interpolators (1,4,5), "B" denotes (1,5,8). For each set of interpolator and fit range, results for small to large lattices are shown from left to right, the corresponding infinite volume limit rightmost.

experiment within roughly 1σ. In general, the determined energy levels in the infinite volume limit agree well with experiment with only a few percent deviation. However, because of the high statistical accuracy of the considered observables, in several cases this deviation is already significantly larger than the statistical uncertainty. This can be understood by noting that systematic errors become more and more significant with increasing accuracy. We remark that taking into account the systematic error stemming from the choice of interpolators and the fit range for the eigenvalues, also $K\,(0^-)$ and Σ are well compatible with experiment.

A possible origin of the deviation of strange hadron energy levels from experiment lies in the choice of the strange quark mass parameter. This reasoning is appealing in particular considering the energy levels of $K^*(1^-)$, Ξ and Ω, which come out too low in our simulation compared to experiment. However, this conjecture is not supported by our results for Λ, which agrees with experiment, and $K\,(0^-)$, which comes out too high. We stress again that the systematic errors related to the choice of the interpolators and the fit range together with the statistical uncertainty already cover a significant part of the deviation. Further systematic errors, which are not estimated quantitatively, could explain the remaining part. We conclude that in general our results in the infinite volume limit compare nicely with experiment, where occasional small deviations are expected to stem from systematic effects which cannot be identified uniquely.

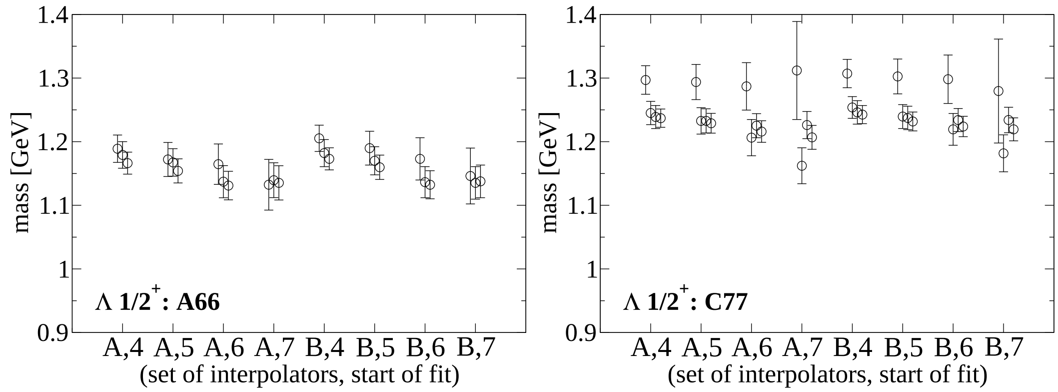

Figure 9.12: Systematic error of the Λ spin $1/2^+$ mass, analogous to Figure 9.2. "A" denotes set of interpolators (2,3,10,18,26,27,34,42), "B" denotes (3,11,18,27,34). For each set of interpolator and fit range, results for small to large lattices are shown from left to right, the corresponding infinite volume limit rightmost.

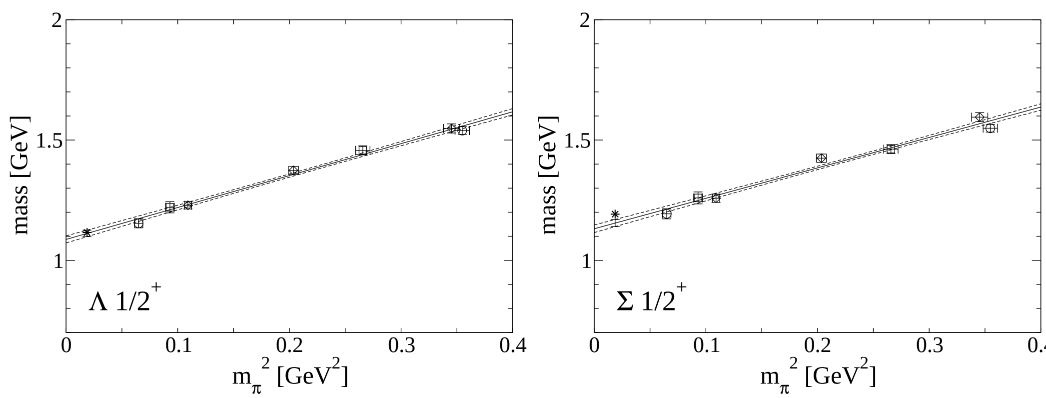

Figure 9.13: Energy levels for the Λ spin $1/2^+$ (lhs) and Σ spin $1/2^+$ (rhs) ground state in the infinite volume limit. After infinite volume extrapolation ((A,5) of Figure 9.12), resp. (A,6) of Figure 9.14), we extrapolate to physical pion masses. We obtain m_Λ=1112(14) MeV, which hits the experimental $\Lambda(1116)^{****}$ nicely, and m_Σ=1156(15) MeV, which is a bit low.

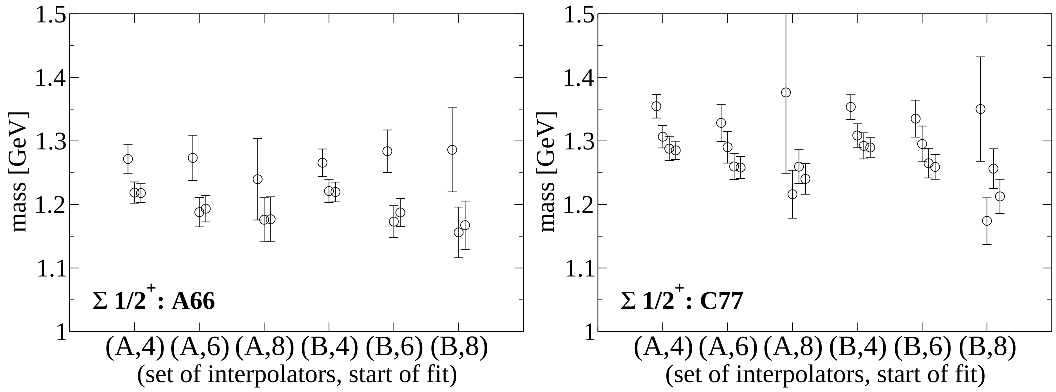

Figure 9.14: Systematic error of the Σ spin $1/2^+$ mass, analogous to Figure 9.2. "A" denotes set of interpolators (1,2,9,10,25,26), "B" denotes (2,3,10,11,19,20,26,27). For each set of interpolator and fit range, results for small to large lattices are shown from left to right, the corresponding infinite volume limit rightmost.

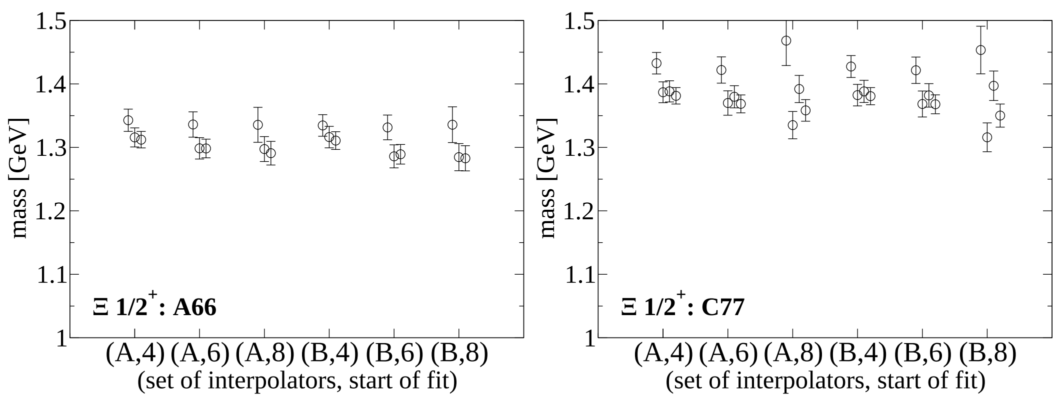

Figure 9.15: Systematic error of the Ξ spin $1/2^+$mass, analogous to Figure 9.2. "A" denotes set of interpolators (1,2,9,10,25,26), "B" denotes (2,3,10,11,19,20,26,27). For each set of interpolator and fit range, results for small to large lattices are shown from left to right, the corresponding infinite volume limit rightmost.

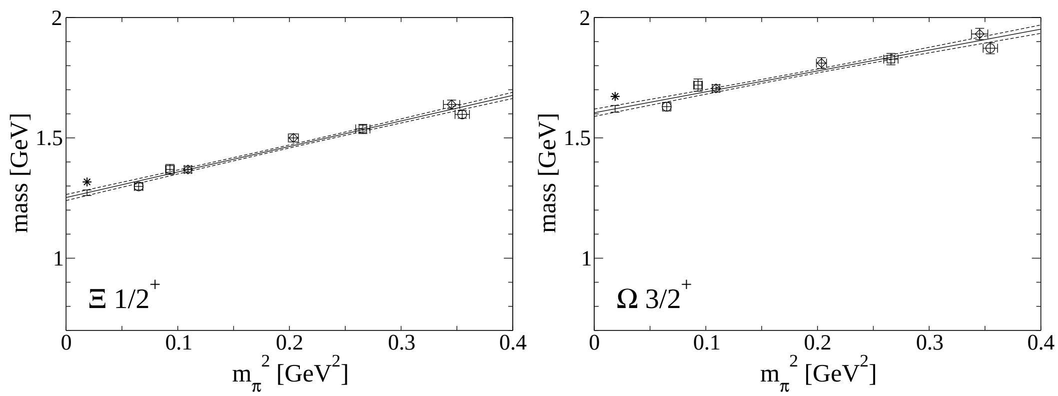

Figure 9.16: Energy levels for Ξ spin $1/2^+$ (lhs) and Ω spin $3/2^+$ (rhs) ground states in the infinite volume limit. After infinite volume extrapolation ((A,6) of Figure 9.15, resp. (B,4) of Figure 9.17), we extrapolate to physical pion masses. We obtain m_Ξ=1273(12) MeV and m_Ω=1620(14) MeV, which both are low compared to experiment.

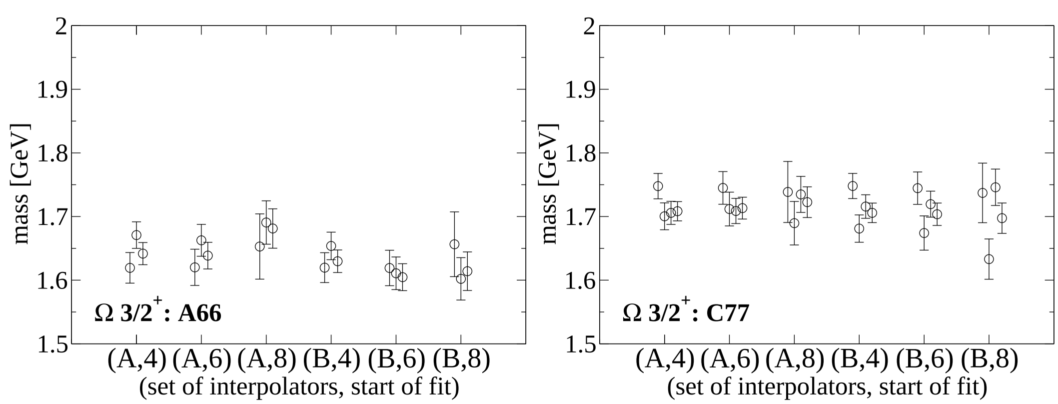

Figure 9.17: Systematic error of the Ω spin $3/2^+$ mass, analogous to Figure 9.2. "A" denotes set of interpolators (1,5,8), "B" denotes (1,3,4). For each set of interpolator and fit range, results for small to large lattices are shown from left to right, the corresponding infinite volume limit rightmost. For definiteness we choose (B,4).

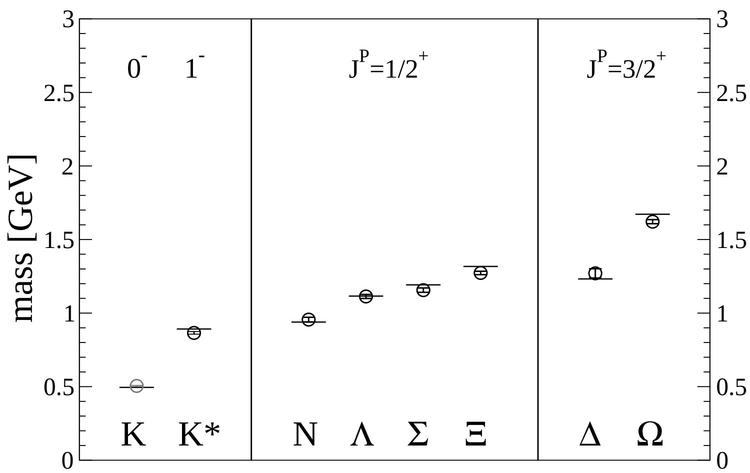

Figure 9.18: Energy levels in the infinite volume limit at the physical point for strange mesons (lhs), spin $1/2^+$ (middle) and $3/2^+$ (rhs) baryons. Horizontal lines represent experimentally known states [7]. The statistical uncertainty of our results is indicated by bands of 1σ. Grey symbols denote a poor χ^2/d.o.f. of the chiral fits (see Table D.6).

Chapter 10

Summary and Conclusion

This thesis provides an ab-initio, non-perturbative determination of the excited meson and baryon spectrum, using the lattice regularization of QCD. The variational method is applied to improve the signal of ground states and also to access excited states. Several interpolators are constructed for each channel, where also derivative operators are included to extend the basis and to have access to spin two and exotic mesons. In case of some specific baryon channels, Fierz identities force point-like interpolators to vanish exactly. We show that interpolators can be constructed nevertheless and propose two strategies, based on quark smearing and the Rarita-Schwinger condition, respectively. Finally, the variational method is used to explore the content of the physical states.

We use a Hybrid Monte Carlo algorithm to generate seven ensembles with two flavors of dynamical Chirally Improved quarks. The improved action is computationally expensive, however, its advantages lie in small discretization effects and frequent tunneling of topological sectors, reducing autocorrelation. The pion masses are in the range of 250 to 600 MeV, the results are extrapolated to the physical pion mass. Three further ensembles on larger and smaller lattices are generated in order to investigate finite volume effects and to perform the infinite volume limit. The strange hadron spectrum is accessed using partial quenching for the strange quark. The scale is set using the Sommer parameter and the pion mass at the physical point.

In general, we find good agreement with experiment for many ground states and also for several excited energy levels. Some of the results deviate from experiment, however, not all systematic effects have been account for. In particular, the excited states still deserve a lot of continuing research. The corresponding statistical errors are often large, and, even worse, some systematic errors are not yet under control. A full systematic treatment of the excited states will need multi-particle interpolators, high statistics for all extrapolations and finally a phase shift analysis for the resonances embedded in the spectral density. Despite these difficulties, already in our limited approach we obtain many interesting results, some of which we want to highlight at this point.

We reproduce and confirm many of the experimentally known resonances, and even predict some new ones. Figures 7.14 and 8.19 show the results for mesons and baryons in a finite box of roughly 2.2 fm after extrapolation to physical pion masses compared to experimental values from [7]. As an example, we determined the ground state in the Λ spin $1/2^-$ channel and find agreement with the experimental $\Lambda(1405)$ within statistical uncertainty. We investigated the singlet/octet content of low-lying Λ states and also the octet/decuplet content of Σ and Ξ observables. In particular, we find that singlet interpolators couple strongly to the low-lying Λ spin 3/2 channels, which is impressive in view of their vanishing for point-like quarks due to Fierz identities. In both the Σ and Ξ spin $1/2^-$ channels, we find a total of three low-lying states, compatible with an approximate threefold degeneracy. Furthermore, in each channel, one of the three states is dominated by decuplet interpolators, which demonstrates that decuplet interpolators are important also for the low-lying spin 1/2 spectrum.

We investigated the strange meson channels 1^-, 1^+ and 2^- with respect to their approximate C-parity. In the 1^- channel, the three lowest states seem to be dominated by negative C-parity. The low-lying 1^+ states show alternating C-parity dominance, and also some mixing of the interpolators. The 2^- channel shows strong mixing towards light pion masses, the ground state being dominated by positive C-parity, the first excitation by negative C-parity.

We discussed finite volume and other systematic effects considering the scale setting scheme and hadron energy levels. The scale as well as the pion mass show a very flat volume dependence in our simulation. In general, the determined hadron energy levels at physical pion masses in the infinite volume limit agree well with experiment with only a few percent deviation, an overview is shown in Figure 9.18. We find that in particular the results for the nucleon, Δ and Λ ground state energy levels agree nicely with experiment within roughly 1σ. Taking into account the systematic error stemming from the choice of interpolators and the fit range for the eigenvalues, also further observables are well compatible with experiment.

The finite volume discussion will be extended to further channels in a forthcoming publication. For further studies we suggest to include a dynamical strange quark in the simulation, and to construct multi-particle interpolators to finally extract the phase shift of the resonances.

Appendix A

The Chirally Improved Dirac Operator

This thesis discusses exclusively dynamical simulations using the Chirally Improved Dirac operator (D_{CI}) [25,26]. We shall now explicitely give the paths and coefficients used in the construction. We repeat the ansatz given in Eq. (4.5),

$$D_{nm} = \sum_{\alpha=1}^{16} \Gamma_\alpha \sum_{p \in \mathcal{P}^\alpha_{m,n}} c_p^\alpha \prod_{l \in p} U_l \, \delta_{n,m+p} \ ,$$

where for each element of the Clifford algebra Γ_α, p is a path connecting the points n, m. $\mathcal{P}^\alpha_{m,n}$ is the set of all considered paths p, and c_p^α are coefficients. Plugging this ansatz into the Ginsparg-Wilson equation leads to a set of algebraic equations, which can be solved numerically after truncation. In our simulation, we restrict the paths to a maximal length of four, all of which are given in Table A.1.

The parameters of the Dirac operator have been tuned following reference [26]. In order to approach physical pion masses and the continuum limit, the bare quark masses and the gauge coupling have to be varied. Following this path in theory space, the parameters of the Dirac operator according to optimum chiral symmetry vary as well. However, a repeated fine-tuning of these parameters for each ensemble would weaken the predictive power significantly. This is why we decided not to repeat the tuning but take the same parameters for the Dirac operator in all ensembles. Note that chiral symmetry is restored in the continuum limit in any case.

Coeff.	Name	Value	Path shape	γ	Multiplicity
1	s_1	1.481599252	$[\,]$	$\mathbb{1}$	1
2	s_2	-0.05218251439	$[i]$	$\mathbb{1}$	8
3	s_3	-0.01473643847	$[i,j]$	$\mathbb{1}$	48
5	s_5	-0.002186103421	$[i,j,k]$	$\mathbb{1}$	192
6	s_6	0.002133989696	$[i,i,j]$	$\mathbb{1}$	96
8	s_8	-0.003997001821	$[i,j,-i]$	$\mathbb{1}$	48
10	s_{10}	-0.0004951673735	$[i,j,k,l]$	$\mathbb{1}$	384
11	s_{11}	-0.0009836500799	$[i,j,-i,k]$	$\mathbb{1}$	384
13	s_{13}	0.007529838581	$[i,j,-i,-j]$	$\mathbb{1}$	48
14	v_1	0.1972229309	$[i]$	γ_i	8
15	v_2	0.008252157565	$[i,j]$	γ_i	96
17	v_4	0.005113056314	$[i,j,k]$	γ_i	384
18	v_5	0.001736609425	$[j,i,k]$	γ_i	192
32	t_1	-0.08792744664	$[i,j]$	$\gamma_i\gamma_\nu$	48
33	t_2	-0.002553055577	$[i,j,k]$	$\gamma_i\gamma_j$	384
34	t_3	0.002093792069	$[i,k,j]$	$\gamma_i\gamma_j$	192
36	t_5	-0.005567377075	$[i,j,-i]$	$\gamma_i\gamma_j$	48
46	t_{15}	-0.003427310798	$[j,i,-j,-i]$	$\gamma_i\gamma_j$	48
51	p_1	-0.008184103136	$[i,j,k,l]$	γ_5	384

Table A.1: Coefficients for the Chirally Improved Dirac operator used in all simulations, taken from [41]. The path shapes are given symbolically, e.g., $[i,j]$ denotes a path in i-direction and then in j-direction ($i \neq j$). The γ-matrices (5-th column) are also permuted as described in more detail in [26].

Appendix B

Meson Interpolators

In this chapter we discuss all meson interpolators used in this work. First, Section B.1 discusses the construction of meson interpolators for good C-parity quantum number. Then, Section B.2 lists all meson interpolators used in this work.

B.1 C-Parity of Meson Interpolators

In this section, we discuss the construction of meson interpolators to obtain good C-parity quantum numbers. Subsection B.1.1 introduces the general setup, next Gaussian interpolators are discussed in Subsection B.1.2. Interpolators including a derivative operator are treated in Subsection B.1.3, finally the case of non-vanishing momentum is investigated in Subsection B.1.4.

B.1.1 General Considerations

C-parity is the symmetry of operators under charge conjugation. Clearly, this symmetry can be rigorously valid only for chargeless operators. For isovector mesons, we thus consider the $I_z = 0$ component. However, a simple calculation shows, that for mass-degenerate quarks the $I_z = 0$ component yields the same correlation functions as the $I_z = \pm 1$ components,

$$\mathrm{tr}\left[O_{I_z=0}(t)O^\dagger_{I_z=0}(0)\right] = \mathrm{tr}\left[O_{I_z=\pm1}(t)O^\dagger_{I_z=\pm1}(0)\right] \ . \tag{B.1}$$

This is because of a cancelation of disconnected diagrams which happens in the case of good isospin symmetry. Because of this identity we use the term "C-parity" loosely also for charged operators. Furthermore, we talk about "approximate C-parity" in the context of non degenerate quark masses. The symmetry transformation is given be the rules

$$\psi(n) \xrightarrow{\mathcal{C}} C^{-1}\overline{\psi}(n)^T \tag{B.2}$$

$$\overline{\psi}(n) \xrightarrow{\mathcal{C}} -\psi(n)^T C \tag{B.3}$$

$$U_\mu(n) \xrightarrow{\mathcal{C}} U_\mu(n)^* = U_\mu(n)^{\dagger T} \ . \tag{B.4}$$

Here and in the following we use matrix/vector notation for Dirac and color indices. The charge conjugation matrix C acts on Dirac indices only and is defined by

$$C\gamma_\mu C^{-1} = -\gamma_\mu^T \; . \tag{B.5}$$

We define c_Γ as

$$C\Gamma_\mu C^{-1} \equiv c_\Gamma \Gamma_\mu^T \; . \tag{B.6}$$

In the chiral representation one finds

$$C = i\gamma_2\gamma_4 \, , \quad C = -C^T \; . \tag{B.7}$$

Now, before going into details of constructing operators, let us discuss a very general property of symmetry transformations $\mathcal{R}$ which square to unity ($\mathcal{R}^2 = \mathbf{1}$). For operators A, B, which transform as

$$A \stackrel{\mathcal{R}}{\longrightarrow} B, \qquad \text{and thus} \quad B \stackrel{\mathcal{R}}{\longrightarrow} A \, , \tag{B.8}$$

we find that $A \pm B$ are eigenstates of $\mathcal{R}$ with quantum numbers $s = \pm 1$. This symmetrization is used for many interpolators, to be discussed in more detail in the following. Note that in case of $A = \pm B$ one of the two symmetrizations yields a vanishing interpolator.

B.1.2 C-Parity at Zero Momentum: Gaussian Interpolators

All analysis performed in this work considers interpolators with vanishing momentum. The case of non-vanishing momentum will be discussed in Subsection B.1.4 for completeness. Here we start with the simplest non-trivial case, given by interpolators involving Gaussian quark smear operators S. First we have to clarify the transformation behavior of the smearing operator under charge conjugation. In this work, Jacobi smearing is used, defined in Eq. (4.20). We find that the effect on the hopping term is transposition,

$$\begin{aligned}
H(n,m) &= \sum_{i=\pm1}^{\pm3} U_i(n)\delta(n+\hat{i},m) && \text{(B.9)}\\
&\xrightarrow{\mathcal{C}} \sum_{i=\pm1}^{\pm3} U_i(n)^{\dagger T}\delta(n+\hat{i},m) && \text{(B.10)}\\
&= \sum_{i=\pm1}^{\pm3} U_{-i}(n+\hat{i})^{T}\delta(n+\hat{i},m) && \text{(B.11)}\\
&= \sum_{i=\pm1}^{\pm3} U_{-i}(m)^{T}\delta(n,m-\hat{i}) && \text{(B.12)}\\
&= \sum_{i=\pm1}^{\pm3} U_{i}(m)^{T}\delta(n,m+\hat{i}) && \text{(B.13)}\\
&= H^T(m,n)\ . && \text{(B.14)}
\end{aligned}$$

And thus also (all indices suppressed)

$$S \xrightarrow{\mathcal{C}} S^T\ . \tag{B.15}$$

For the subsequent calculations we switch to a notation where also the spacetime dependence is expressed using index notation whenever it is convenient. We consider a one flavor meson interpolator with Gaussian quark fields and an arbitrary Dirac structure Γ. Under charge conjugation we find that, using summation convention for all repeated indices,

$$\begin{aligned}
\overline{\psi}_{n'}S^{(1)}_{n',n}\Gamma S^{(2)}_{n,m'}\psi_{m'} &\xrightarrow{\mathcal{C}} \left(-\psi^T_{n'}C\right) S^{(1)T}_{n,n'}\Gamma^T S^{(2)T}_{m',n}\left(C\overline{\psi}^T_{m'}\right) && \text{(B.16)}\\
&= -\psi^T_{n'}S^{(1)T}_{n,n'}\,c_\Gamma\Gamma^T S^{(2)T}_{m',n}\overline{\psi}^T_{m'} && \text{(B.17)}\\
&= c_\Gamma\overline{\psi}_{m'}S^{(2)}_{m',n}\Gamma S^{(1)}_{n,n'}\psi_{n'} && \text{(B.18)}\\
&= c_\Gamma\overline{\psi}_{n'}S^{(2)}_{n',n}\Gamma S^{(1)}_{n,m'}\psi_{m'}\ . && \text{(B.19)}
\end{aligned}$$

In the last line we renamed the summation indices. Obviously, this interpolator has a good quantum number of c_Γ if $S^{(1)} = S^{(2)}$. In general, however, symmetrization is need to construct interpolators with a good C-parity quantum number,

$$\begin{aligned}
O &= \overline{\psi}_{n'}\Gamma\left[S^{(1)}_{n',n}S^{(2)}_{n,m'} \pm c_\Gamma S^{(2)}_{n',n}S^{(1)}_{n,m'}\right]\psi_{m'} && \text{(B.20)}\\
&\xrightarrow{\mathcal{C}} \pm O && \text{(B.21)}
\end{aligned}$$

The generalization to two flavor interpolators is straightforward.

B.1.3 C-Parity at Zero Momentum: Derivatives

The definition of the derivative source smear operator was given in Eq. (4.21). Its behavior under charge conjugation is calculated analogously to the one of the hopping term. One finds transposition and sign flipping,

$$\begin{aligned} P_i(n,m) &= U_i(n)\delta(n+\hat{i},m) - U_{-i}(n)\delta(n-\hat{i},m) &\quad (B.22)\\ &= -P_i^\dagger(m,n) &\quad (B.23)\\ P_i(n,m) &\xrightarrow{\mathcal{C}} -P_i^T(m,n)\ . &\quad (B.24)\end{aligned}$$

In the literature one often finds the convention $\overrightarrow{D} = P$ and $\overleftarrow{D} = P^\dagger$, the difference lying only in normalization. Now, consider charge conjugation for a one flavor meson interpolator including a derivative,

$$\begin{aligned} \overline{\psi}_{n'} S^{(1)}_{n',n} \Gamma P^i_{n,m} S^{(2)}_{m,m'} \psi_{m'} &\xrightarrow{\mathcal{C}} (-\psi^T_{n'} C) S^{(1)T}_{n,n'} \Gamma^T (-P^T)^i_{m,n} S^{(2)T}_{m',m} C^{-1} \overline{\psi}^T_{m'}\\ &= -c_\Gamma \overline{\psi}_n S^{(2)}_{n',n} P^i_{n,m} \Gamma S^{(1)}_{m,m'} \psi_{m'} &\quad (B.25)\\ &= c_\Gamma \overline{\psi}_n S^{(2)}_{n',n} (P^\dagger)^i_{n,m} \Gamma S^{(1)}_{m,m'} \psi_{m'}\ . &\quad (B.26)\end{aligned}$$

The last step uses Eq. (B.23), which corresponds to a partial integration in the continuum formulation. We find that this interpolator has a good quantum number of $-c_\Gamma$ if $S^{(1)} = S^{(2)}$. In general, however, symmetrization is needed again for good C-parity quantum numbers. For clarity we suppress now all indices, obtaining

$$\begin{aligned} O &= \overline{\psi}\Gamma \left[S^1 P S^2 \pm c_\Gamma S^2 P^\dagger S^1 \right] \psi &\quad (B.27)\\ &\xrightarrow{\mathcal{C}} \pm O\ . &\quad (B.28)\end{aligned}$$

In this expression, the derivative operator $P^\dagger$ in the second term can be seen as P "acting to the left". This has advantages in numerics, if the derivative cannot be applied after inverting the Dirac operator.

Note that if $S^{(1)} = S^{(2)}$, no symmetrization is necessary for a good C-parity quantum number, which means that the opposite quantum number cannot be realized with the given interpolator. The corresponding symmetrization yields an interpolator which is identical to zero. This is circumvented in the present work by considering a different order of operators in the definition of the interpolators,

$$O = \overline{\psi}\Gamma \left[S^1 S^2 P \pm c_\Gamma P^\dagger S^2 S^1 \right] \psi\ , \quad (B.29)$$

which remains non-vanishing even if $S^1 = S^2$, since $[P,S] \neq 0$. Obviously, this choice makes a symmetrization mandatory for a good quantum number. This commutator can be seen as introducing additional pieces of paths in the combined smearing operator, which means changed weights of the existing paths and a few new paths. Numerically, we find that the corresponding correlators are of the same magnitude as others and yield consistent signals. Hence, this asymmetric definition enlarges the basis of operators to some extent. In particular some exotic channels can be accessed this way already with fewer derivatives. Numerically, this asymmetric definition of the interpolators is implemented by first applying the Gaussian smearing operator on a point source and only afterwards applying the derivative operator.

B.1.4 C-Parity for Non-Zero Momentum

For non-zero momentum, the space dependence of the momentum projection operator can cause some complications for interpolators including derivative operators. Let us first discuss interpolators in the continuum,

$$\overrightarrow{D}_\mu = \overrightarrow{\partial}_\mu + iA_\mu(x) \tag{B.30}$$

$$\overleftarrow{D}_\mu = \overrightarrow{D}_\mu^\dagger \tag{B.31}$$

$$A_\mu(x) \xrightarrow{\mathcal{C}} -A_\mu^T(x)\ , \tag{B.32}$$

where the overhead arrow denotes the direction in which the derivative has to be applied. Charge conjugation of a simple one flavor interpolator reads, suppressing the space dependence of the fields,

$$\int d^3x \mathrm{e}^{i\vec{p}\cdot\vec{x}}\overline{\psi}\Gamma\left(\overrightarrow{D}_\mu\psi\right) \xrightarrow{\mathcal{C}} c_\Gamma \int d^3x \mathrm{e}^{i\vec{p}\cdot\vec{x}}\left(\overline{\psi}\overleftarrow{D}_\mu\right)\Gamma\psi\ . \tag{B.33}$$

Again, we can construct good quantum numbers by symmetrization. Note that partial integration would yield a term proportional to the momentum.

Now consider the same calculation on the lattice, which is the generalization of Eq. (B.26),

$$\overline{\psi}_{n'}S^{(1)}_{n',n}\mathrm{e}^{i\vec{p}\cdot\vec{n}}\Gamma P^i_{n,m}S^{(2)}_{m,m'}\psi_{m'} \xrightarrow{\mathcal{C}} c_\Gamma\overline{\psi}_{n'}S^{(2)}_{n',n}(P^\dagger)^i_{n,m}\Gamma\mathrm{e}^{i\vec{p}\cdot\vec{m}}S^{(1)}_{m,m'}\psi_{m'} \tag{B.34}$$

$$\overline{\psi}_{n'}S^{(1)}_{n',n}\mathrm{e}^{i\vec{p}\cdot\vec{n}}\Gamma S^{(2)}_{n,m}P^i_{m,m'}\psi_{m'} \xrightarrow{\mathcal{C}} c_\Gamma\overline{\psi}_{n'}(P^\dagger)^i_{n',n}S^{(2)}_{n,m}\Gamma\mathrm{e}^{i\vec{p}\cdot\vec{m}}S^{(1)}_{m,m'}\psi_{m'}\ . \tag{B.35}$$

The second line differs from the first one just by the order of the derivative and the Gaussian smearing operator. The case of $p = 0$ produces the known result. For $p \neq 0$, however, we observe that the momentum projection on the right hand side has a wrong argument (m) compared to the original expression (n). This appears due to a renaming of the indices, which is necessary to match the quark fields of the original expression. To still achieve good C-parity quantum numbers, we have to take into account also the momentum projection operator when symmetrizing. This yields interpolators of the kind (following Eq. (B.35))

$$O = \overline{\psi}_{n'}\Gamma\left[S^{(1)}_{n',n}\mathrm{e}^{i\vec{p}\cdot\vec{n}}S^{(2)}_{n,m}P^i_{m,m'} \pm c_\Gamma(P^\dagger)^i_{n',n}S^{(2)}_{n,m}\mathrm{e}^{i\vec{p}\cdot\vec{m}}S^{(1)}_{m,m'}\right]\psi_{m'}\ . \tag{B.36}$$

Comparing with the discussion in the continuum, one might expect that ignoring the momentum projection operator in the symmetrization leads to discretization errors. This is indeed true and can be verified by applying the Kronecker deltas inside the derivative on the momentum projection operator. Now we follow Eq. (B.34), since Eq. (B.35) would introduce additional factors of $[P, S]$. We find

$$
\begin{aligned}
(P^\dagger)^i_{n,m} \mathrm{e}^{i\vec{p}\cdot\vec{m}} &= \left[\delta_n^{m+\hat{i}} U_m^{\dagger i} - \delta_n^{m-\hat{i}} U_m^{\dagger -i}\right] \mathrm{e}^{i\vec{p}\cdot\vec{m}} && \text{(B.37)}\\
&= \mathrm{e}^{i\vec{p}\cdot\vec{n}} \left[\mathrm{e}^{i\vec{p}\cdot\hat{i}} \delta_n^{m+\hat{i}} U_m^{\dagger i} - \mathrm{e}^{-i\vec{p}\cdot\hat{i}} \delta_n^{m-\hat{i}} U_m^{\dagger -i}\right] && \text{(B.38)}\\
&= \mathrm{e}^{i\vec{p}\cdot\vec{n}} \left[\mathrm{e}^{iap_i} \delta_n^{m+\hat{i}} U_m^{\dagger i} - \mathrm{e}^{-iap_i} \delta_n^{m-\hat{i}} U_m^{\dagger -i}\right] && \text{(B.39)}\\
&= \mathrm{e}^{i\vec{p}\cdot\vec{n}} \left[\delta_n^{m+\hat{i}} U_m^{\dagger i} - \delta_n^{m-\hat{i}} U_m^{\dagger -i}\right] + \mathcal{O}(a) && \text{(B.40)}\\
&= \mathrm{e}^{i\vec{p}\cdot\vec{n}} (P^\dagger)^i_{n,m} + \mathcal{O}(a)\ , && \text{(B.41)}
\end{aligned}
$$

where in the second to the last line we expanded the exponentials inside the brackets to identify the discretization errors. Finally we remark that further symmetrization may be necessary for other quantum numbers.

B.2 Meson Interpolator Tables

The construction of meson interpolators is discussed in Sections 4.3.4 and Appendix B.1. In the tables for meson interpolators (Table B.1 to B.8), the two quark fields are labeled by a and b. These are placeholders for light (u, d) or strange (s) quarks. The indices n, w and ∂_i correspond to the smearings narrow, wide and derivative, respectively. γ_i are the spatial Dirac matrices, γ_t is the Dirac matrix in time direction. ϵ_{ijk} is the Levi-Civita symbol, Q_{ijk} are Clebsch-Gordon coefficients, where all elements are zero except $Q_{111} = \frac{1}{\sqrt{2}}$, $Q_{122} = -\frac{1}{\sqrt{2}}$, $Q_{211} = -\frac{1}{\sqrt{6}}$, $Q_{222} = -\frac{1}{\sqrt{6}}$ and $Q_{233} = \frac{2}{\sqrt{6}}$.

$\#_{0^-}$	Interpolators	C
1	$\overline{a}_n \gamma_5 b_n$	$+$
2	$\overline{a}_n \gamma_5 b_w + \overline{a}_w \gamma_5 b_n$	$+$
3	$\overline{a}_n \gamma_5 b_w - \overline{a}_w \gamma_5 b_n$	$-$
4	$\overline{a}_w \gamma_5 b_w$	$+$
5	$\overline{a}_n \gamma_t \gamma_5 b_n$	$+$
6	$\overline{a}_n \gamma_t \gamma_5 b_w + \overline{a}_w \gamma_t \gamma_5 b_n$	$+$
7	$\overline{a}_n \gamma_t \gamma_5 b_w - \overline{a}_w \gamma_t \gamma_5 b_n$	$-$
8	$\overline{a}_w \gamma_t \gamma_5 b_w$	$+$
9	$\overline{a}_{\partial_i} \gamma_i \gamma_5 b_n + \overline{a}_n \gamma_i \gamma_5 b_{\partial_i}$	$+$
10	$\overline{a}_{\partial_i} \gamma_i \gamma_5 b_n - \overline{a}_n \gamma_i \gamma_5 b_{\partial_i}$	$-$
11	$\overline{a}_{\partial_i} \gamma_i \gamma_5 b_w + \overline{a}_w \gamma_i \gamma_5 b_{\partial_i}$	$+$
12	$\overline{a}_{\partial_i} \gamma_i \gamma_5 b_w - \overline{a}_w \gamma_i \gamma_5 b_{\partial_i}$	$-$
13	$\overline{a}_{\partial_i} \gamma_i \gamma_t \gamma_5 b_n + \overline{a}_n \gamma_i \gamma_t \gamma_5 b_{\partial_i}$	$-$
14	$\overline{a}_{\partial_i} \gamma_i \gamma_t \gamma_5 b_n - \overline{a}_n \gamma_i \gamma_t \gamma_5 b_{\partial_i}$	$+$
15	$\overline{a}_{\partial_i} \gamma_i \gamma_t \gamma_5 b_w + \overline{a}_w \gamma_i \gamma_t \gamma_5 b_{\partial_i}$	$-$
16	$\overline{a}_{\partial_i} \gamma_i \gamma_t \gamma_5 b_w - \overline{a}_w \gamma_i \gamma_t \gamma_5 b_{\partial_i}$	$+$
17	$\overline{a}_{\partial_i} \gamma_5 b_{\partial_i}$	$+$
18	$\overline{a}_{\partial_i} \gamma_t \gamma_5 b_{\partial_i}$	$+$

Table B.1: Meson interpolators for $J^P = 0^-$. The first row shows the number, the second shows the explicit form of the interpolator. In the last column the C parity is given, which is only an approximate quantum number in the case of differing quark masses. Horizontal dashed lines separate different Dirac structures.

$\#_{0^+}$	Interpolators	C parity
1	$\overline{a}_n b_n$	$+$
2	$\overline{a}_n b_w + \overline{a}_w b_n$	$+$
3	$\overline{a}_n b_w - \overline{a}_w b_n$	$-$
4	$\overline{a}_w b_w$	$+$
5	$\overline{a}_{\partial_i} \gamma_i b_n + \overline{a}_n \gamma_i b_{\partial_i}$	$-$
6	$\overline{a}_{\partial_i} \gamma_i b_n - \overline{a}_n \gamma_i b_{\partial_i}$	$+$
7	$\overline{a}_{\partial_i} \gamma_i b_w + \overline{a}_w \gamma_i b_{\partial_i}$	$-$
8	$\overline{a}_{\partial_i} \gamma_i b_w - \overline{a}_w \gamma_i b_{\partial_i}$	$+$
9	$\overline{a}_{\partial_i} \gamma_i \gamma_t b_n + \overline{a}_n \gamma_i \gamma_t b_{\partial_i}$	$-$
10	$\overline{a}_{\partial_i} \gamma_i \gamma_t b_n - \overline{a}_n \gamma_i \gamma_t b_{\partial_i}$	$+$
11	$\overline{a}_{\partial_i} \gamma_i \gamma_t b_w + \overline{a}_w \gamma_i \gamma_t b_{\partial_i}$	$-$
12	$\overline{a}_{\partial_i} \gamma_i \gamma_t b_w - \overline{a}_w \gamma_i \gamma_t b_{\partial_i}$	$+$
13	$\overline{a}_{\partial_i} b_{\partial_i}$	$+$

Table B.2: Same as Table B.1, now for $J^P = 0^+$.

$\#_{1^-}$	Interpolators	C
1	$\overline{a}_n \gamma_k b_n$	$-$
2	$\overline{a}_n \gamma_k b_w + \overline{a}_w \gamma_k b_n$	$-$
3	$\overline{a}_n \gamma_k b_w - \overline{a}_w \gamma_k b_n$	$+$
4	$\overline{a}_w \gamma_k b_w$	$-$
5	$\overline{a}_n \gamma_k \gamma_t b_n$	$-$
6	$\overline{a}_n \gamma_k \gamma_t b_w + \overline{a}_w \gamma_k \gamma_t b_n$	$-$
7	$\overline{a}_n \gamma_k \gamma_t b_w - \overline{a}_w \gamma_k \gamma_t b_n$	$+$
8	$\overline{a}_w \gamma_k \gamma_t b_w$	$-$
9	$\overline{a}_{\partial_k} b_n + \overline{a}_n b_{\partial_k}$	$+$
10	$\overline{a}_{\partial_k} b_n - \overline{a}_n b_{\partial_k}$	$-$
11	$\overline{a}_{\partial_k} b_w + \overline{a}_w b_{\partial_k}$	$+$
12	$\overline{a}_{\partial_k} b_w - \overline{a}_w b_{\partial_k}$	$-$
13	$\overline{a}_{\partial_k} \gamma_t b_n + \overline{a}_n \gamma_t b_{\partial_k}$	$-$
14	$\overline{a}_{\partial_k} \gamma_t b_n - \overline{a}_n \gamma_t b_{\partial_k}$	$+$
15	$\overline{a}_{\partial_k} \gamma_t b_w + \overline{a}_w \gamma_t b_{\partial_k}$	$-$
16	$\overline{a}_{\partial_k} \gamma_t b_w - \overline{a}_w \gamma_t b_{\partial_k}$	$+$
17	$\overline{a}_{\partial_i} \gamma_k b_{\partial_i}$	$-$
18	$\overline{a}_{\partial_i} \gamma_k \gamma_t b_{\partial_i}$	$-$
19	$\overline{a}_{\partial_k} \epsilon_{ijk} \gamma_j \gamma_5 b_n + \overline{a}_n \epsilon_{ijk} \gamma_j \gamma_5 b_{\partial_k}$	$+$
20	$\overline{a}_{\partial_k} \epsilon_{ijk} \gamma_j \gamma_5 b_n - \overline{a}_n \epsilon_{ijk} \gamma_j \gamma_5 b_{\partial_k}$	$-$
21	$\overline{a}_{\partial_k} \epsilon_{ijk} \gamma_j \gamma_5 b_w + \overline{a}_w \epsilon_{ijk} \gamma_j \gamma_5 b_{\partial_k}$	$+$
22	$\overline{a}_{\partial_k} \epsilon_{ijk} \gamma_j \gamma_5 b_w - \overline{a}_w \epsilon_{ijk} \gamma_j \gamma_5 b_{\partial_k}$	$-$
23	$\overline{a}_{\partial_k} \epsilon_{ijk} \gamma_j \gamma_t \gamma_5 b_n + \overline{a}_n \epsilon_{ijk} \gamma_j \gamma_t \gamma_5 b_{\partial_k}$	$-$
24	$\overline{a}_{\partial_k} \epsilon_{ijk} \gamma_j \gamma_t \gamma_5 b_n - \overline{a}_n \epsilon_{ijk} \gamma_j \gamma_t \gamma_5 b_{\partial_k}$	$+$
25	$\overline{a}_{\partial_k} \epsilon_{ijk} \gamma_j \gamma_t \gamma_5 b_w + \overline{a}_w \epsilon_{ijk} \gamma_j \gamma_t \gamma_5 b_{\partial_k}$	$-$
26	$\overline{a}_{\partial_k} \epsilon_{ijk} \gamma_j \gamma_t \gamma_5 b_w - \overline{a}_w \epsilon_{ijk} \gamma_j \gamma_t \gamma_5 b_{\partial_k}$	$+$

Table B.3: Same as Table B.1, now for $J^P = 1^-$.

$\#_{1^+}$	Interpolators	C
1	$\overline{a}_n \gamma_k \gamma_5 b_n$	$+$
2	$\overline{a}_n \gamma_k \gamma_5 b_w + \overline{a}_w \gamma_k \gamma_5 b_n$	$+$
3	$\overline{a}_n \gamma_k \gamma_5 b_w - \overline{a}_w \gamma_k \gamma_5 b_n$	$-$
4	$\overline{a}_w \gamma_k \gamma_5 b_w$	$+$
5	$\overline{a}_{\partial_k} \gamma_5 b_n + \overline{a}_n \gamma_5 b_{\partial_k}$	$+$
6	$\overline{a}_{\partial_k} \gamma_5 b_n - \overline{a}_n \gamma_5 b_{\partial_k}$	$-$
7	$\overline{a}_{\partial_k} \gamma_5 b_w + \overline{a}_w \gamma_5 b_{\partial_k}$	$+$
8	$\overline{a}_{\partial_k} \gamma_5 b_w - \overline{a}_w \gamma_5 b_{\partial_k}$	$-$
9	$\overline{a}_{\partial_k} \gamma_t \gamma_5 b_n + \overline{a}_n \gamma_t \gamma_5 b_{\partial_k}$	$+$
10	$\overline{a}_{\partial_k} \gamma_t \gamma_5 b_n - \overline{a}_n \gamma_t \gamma_5 b_{\partial_k}$	$-$
11	$\overline{a}_{\partial_k} \gamma_t \gamma_5 b_w + \overline{a}_w \gamma_t \gamma_5 b_{\partial_k}$	$+$
12	$\overline{a}_{\partial_k} \gamma_t \gamma_5 b_w - \overline{a}_w \gamma_t \gamma_5 b_{\partial_k}$	$-$
13	$\overline{a}_{\partial_i} \gamma_k \gamma_5 b_{\partial_i}$	$+$
14	$\epsilon_{ijk} \overline{a}_{\partial_k} \gamma_j b_n + \epsilon_{ijk} \overline{a}_n \gamma_j b_{\partial_k}$	$-$
15	$\epsilon_{ijk} \overline{a}_{\partial_k} \gamma_j b_n - \epsilon_{ijk} \overline{a}_n \gamma_j b_{\partial_k}$	$+$
16	$\epsilon_{ijk} \overline{a}_{\partial_k} \gamma_j b_w + \epsilon_{ijk} \overline{a}_w \gamma_j b_{\partial_k}$	$-$
17	$\epsilon_{ijk} \overline{a}_{\partial_k} \gamma_j b_w - \epsilon_{ijk} \overline{a}_w \gamma_j b_{\partial_k}$	$+$
18	$\epsilon_{ijk} \overline{a}_{\partial_k} \gamma_j \gamma_t b_n + \epsilon_{ijk} \overline{a}_n \gamma_j \gamma_t b_{\partial_k}$	$-$
19	$\epsilon_{ijk} \overline{a}_{\partial_k} \gamma_j \gamma_t b_n - \epsilon_{ijk} \overline{a}_n \gamma_j \gamma_t b_{\partial_k}$	$+$
20	$\epsilon_{ijk} \overline{a}_{\partial_k} \gamma_j \gamma_t b_w + \epsilon_{ijk} \overline{a}_w \gamma_j \gamma_t b_{\partial_k}$	$-$
21	$\epsilon_{ijk} \overline{a}_{\partial_k} \gamma_j \gamma_t b_w - \epsilon_{ijk} \overline{a}_w \gamma_j \gamma_t b_{\partial_k}$	$+$
22	$\overline{a}_n \gamma_k \gamma_t \gamma_5 b_n$	$-$
23	$\overline{a}_n \gamma_k \gamma_t \gamma_5 b_w + \overline{a}_w \gamma_k \gamma_t \gamma_5 b_n$	$-$
24	$\overline{a}_n \gamma_k \gamma_t \gamma_5 b_w - \overline{a}_w \gamma_k \gamma_t \gamma_5 b_n$	$+$
25	$\overline{a}_w \gamma_k \gamma_t \gamma_5 b_w$	$-$
26	$\overline{a}_{\partial_i} \gamma_k \gamma_t \gamma_5 b_{\partial_i}$	$-$

Table B.4: Same as Table B.1, now for $J^P = 1^+$.

$\#_{2^-E}$	Interpolators	C
1	$Q_{ijk}\bar{a}_{\partial_k}\gamma_j\gamma_t\gamma_5 b_n + Q_{ijk}\bar{a}_n\gamma_j\gamma_t\gamma_5 b_{\partial_k}$	$-$
2	$Q_{ijk}\bar{a}_{\partial_k}\gamma_j\gamma_t\gamma_5 b_n - Q_{ijk}\bar{a}_n\gamma_j\gamma_t\gamma_5 b_{\partial_k}$	$+$
3	$Q_{ijk}\bar{a}_{\partial_k}\gamma_j\gamma_t\gamma_5 b_w + Q_{ijk}\bar{a}_w\gamma_j\gamma_t\gamma_5 b_{\partial_k}$	$-$
4	$Q_{ijk}\bar{a}_{\partial_k}\gamma_j\gamma_t\gamma_5 b_w - Q_{ijk}\bar{a}_w\gamma_j\gamma_t\gamma_5 b_{\partial_k}$	$+$
5	$Q_{ijk}\bar{a}_{\partial_j}\gamma_5 b_{\partial_k}$	$+$
6	$Q_{ijk}\bar{a}_{\partial_j}\gamma_t\gamma_5 b_{\partial_k}$	$+$
7	$Q_{ijk}\bar{a}_{\partial_k}\gamma_j\gamma_5 b_n + Q_{ijk}\bar{a}_n\gamma_j\gamma_5 b_{\partial_k}$	$+$
8	$Q_{ijk}\bar{a}_{\partial_k}\gamma_j\gamma_5 b_n - Q_{ijk}\bar{a}_n\gamma_j\gamma_5 b_{\partial_k}$	$-$
9	$Q_{ijk}\bar{a}_{\partial_k}\gamma_j\gamma_5 b_w + Q_{ijk}\bar{a}_w\gamma_j\gamma_5 b_{\partial_k}$	$+$
10	$Q_{ijk}\bar{a}_{\partial_k}\gamma_j\gamma_5 b_w - Q_{ijk}\bar{a}_w\gamma_j\gamma_5 b_{\partial_k}$	$-$

Table B.5: Same as Table B.1, now for $J^P = 2^- E$.

$\#_{2^+E}$	Interpolators	C
1	$Q_{ijk}\bar{a}_{\partial_k}\gamma_j b_n + Q_{ijk}\bar{a}_n\gamma_j b_{\partial_k}$	$-$
2	$Q_{ijk}\bar{a}_{\partial_k}\gamma_j b_n - Q_{ijk}\bar{a}_n\gamma_j b_{\partial_k}$	$+$
3	$Q_{ijk}\bar{a}_{\partial_k}\gamma_j b_w + Q_{ijk}\bar{a}_w\gamma_j b_{\partial_k}$	$-$
4	$Q_{ijk}\bar{a}_{\partial_k}\gamma_j b_w - Q_{ijk}\bar{a}_w\gamma_j b_{\partial_k}$	$+$
5	$Q_{ijk}\bar{a}_{\partial_k}\gamma_j\gamma_t b_n + Q_{ijk}\bar{a}_n\gamma_j\gamma_t b_{\partial_k}$	$-$
6	$Q_{ijk}\bar{a}_{\partial_k}\gamma_j\gamma_t b_n - Q_{ijk}\bar{a}_n\gamma_j\gamma_t b_{\partial_k}$	$+$
7	$Q_{ijk}\bar{a}_{\partial_k}\gamma_j\gamma_t b_w + Q_{ijk}\bar{a}_w\gamma_j\gamma_t b_{\partial_k}$	$-$
8	$Q_{ijk}\bar{a}_{\partial_k}\gamma_j\gamma_t b_w - Q_{ijk}\bar{a}_w\gamma_j\gamma_t b_{\partial_k}$	$+$
9	$Q_{ijk}\bar{a}_{\partial_j} b_{\partial_k}$	$+$
10	$Q_{ijk}\bar{a}_{\partial_j}\gamma_t b_{\partial k}$	$-$

Table B.6: Same as Table B.1, now for $J^P = 2^+ E$.

$\#_{2^-T_2}$	Interpolators	C
1	$\lvert\epsilon_{ijk}\rvert\bar{a}_{\partial_k}\gamma_j\gamma_5 b_n + \lvert\epsilon_{ijk}\rvert\bar{a}_n\gamma_j\gamma_5 b_{\partial_k}$	+
2	$\lvert\epsilon_{ijk}\rvert\bar{a}_{\partial_k}\gamma_j\gamma_5 b_n - \lvert\epsilon_{ijk}\rvert\bar{a}_n\gamma_j\gamma_5 b_{\partial_k}$	−
3	$\lvert\epsilon_{ijk}\rvert\bar{a}_{\partial_k}\gamma_j\gamma_5 b_w + \lvert\epsilon_{ijk}\rvert\bar{a}_w\gamma_j\gamma_5 b_{\partial_k}$	+
4	$\lvert\epsilon_{ijk}\rvert\bar{a}_{\partial_k}\gamma_j\gamma_5 b_w - \lvert\epsilon_{ijk}\rvert\bar{a}_w\gamma_j\gamma_5 b_{\partial_k}$	−
5	$\lvert\epsilon_{ijk}\rvert\bar{a}_{\partial_k}\gamma_j\gamma_t\gamma_5 b_n + \lvert\epsilon_{ijk}\rvert\bar{a}_n\gamma_j\gamma_t\gamma_5 b_{\partial_k}$	−
6	$\lvert\epsilon_{ijk}\rvert\bar{a}_{\partial_k}\gamma_j\gamma_t\gamma_5 b_n - \lvert\epsilon_{ijk}\rvert\bar{a}_n\gamma_j\gamma_t\gamma_5 b_{\partial_k}$	+
7	$\lvert\epsilon_{ijk}\rvert\bar{a}_{\partial_k}\gamma_j\gamma_t\gamma_5 b_w + \lvert\epsilon_{ijk}\rvert\bar{a}_w\gamma_j\gamma_t\gamma_5 b_{\partial_k}$	−
8	$\lvert\epsilon_{ijk}\rvert\bar{a}_{\partial_k}\gamma_j\gamma_t\gamma_5 b_w - \lvert\epsilon_{ijk}\rvert\bar{a}_w\gamma_j\gamma_t\gamma_5 b_{\partial_k}$	+

Table B.7: Same as Table B.1, now for $J^P = 2^-T_2$.

$\#_{2^+T_2}$	Interpolators	C
1	$\lvert\epsilon_{ijk}\rvert\bar{a}_{\partial_k}\gamma_j b_n + \lvert\epsilon_{ijk}\rvert\bar{a}_n\gamma_j b_{\partial_k}$	−
2	$\lvert\epsilon_{ijk}\rvert\bar{a}_{\partial_k}\gamma_j b_n - \lvert\epsilon_{ijk}\rvert\bar{a}_n\gamma_j b_{\partial_k}$	+
3	$\lvert\epsilon_{ijk}\rvert\bar{a}_{\partial_k}\gamma_j b_w + \lvert\epsilon_{ijk}\rvert\bar{a}_w\gamma_j b_{\partial_k}$	−
4	$\lvert\epsilon_{ijk}\rvert\bar{a}_{\partial_k}\gamma_j b_w - \lvert\epsilon_{ijk}\rvert\bar{a}_w\gamma_j b_{\partial_k}$	+
5	$\lvert\epsilon_{ijk}\rvert\bar{a}_{\partial_k}\gamma_j\gamma_t b_n + \lvert\epsilon_{ijk}\rvert\bar{a}_n\gamma_j\gamma_t b_{\partial_k}$	−
6	$\lvert\epsilon_{ijk}\rvert\bar{a}_{\partial_k}\gamma_j\gamma_t b_n - \lvert\epsilon_{ijk}\rvert\bar{a}_n\gamma_j\gamma_t b_{\partial_k}$	+
7	$\lvert\epsilon_{ijk}\rvert\bar{a}_{\partial_k}\gamma_j\gamma_t b_w + \lvert\epsilon_{ijk}\rvert\bar{a}_w\gamma_j\gamma_t b_{\partial_k}$	−
8	$\lvert\epsilon_{ijk}\rvert\bar{a}_{\partial_k}\gamma_j\gamma_t b_w - \lvert\epsilon_{ijk}\rvert\bar{a}_w\gamma_j\gamma_t b_{\partial_k}$	+

Table B.8: Same as Table B.1, now for $J^P = 2^+T_2$.

Appendix C

Baryon Interpolators

In this Chapter, we discuss all baryon interpolators used in this work. In Section C.1 we briefly review the construction of baryon correlation functions with respect to parity and the projection of Rarita-Schwinger fields to definite spin. Finally, all baryon interpolators used in this work are listed in the tables of Section C.2.

C.1 Generalities

All interpolators are projected to definite parity using the projector

$$P^{\pm} = \frac{1}{2}(\mathbb{1} \pm \gamma_t) \; . \tag{C.1}$$

The resulting correlation matrices of positive and negative parity ($\pm$),

$$C^{\pm}_{ij}(t) = \pm Z^{\pm}_{ij} \mathrm{e}^{-tE^{\pm}} \pm Z^{\mp}_{ij} \mathrm{e}^{-(T-t)E^{\mp}} , \tag{C.2}$$

are combined to the correlation matrices

$$C(t) = \frac{1}{2}\left(C^{+}(t) - C^{-}(T-t)\right) \; , \tag{C.3}$$

which are then used in the variational method.

All Rarita-Schwinger fields (spin 3/2 interpolators of Table C.1) are projected to definite spin 3/2 using the continuum formulation of the Rarita-Schwinger projector [172]

$$P^{3/2}_{\mu\nu}(\vec{p}) = \delta_{\mu\nu} - \frac{1}{3}\gamma_\mu\gamma_\nu - \frac{1}{3p^2}(\gamma \cdot p \, \gamma_\mu p_\nu + p_\mu \gamma_\nu \gamma \cdot p) \; . \tag{C.4}$$

C.2 Baryon Interpolator Tables

The construction of baryon interpolators is discussed in Section 4.3.4. The resulting baryon interpolators, used in this work, are detailed in Tables C.1, C.2 and C.3. Table C.1 shows the flavor structure for all interpolators. For the spin 1/2 channels of nucleon, Σ, Ξ and Λ, we use three different Dirac structures $\chi^{(i)} = (\Gamma_1^{(i)}, \Gamma_2^{(i)}), (i = 1, 2, 3)$, listed in Table C.2. Details about the quark smearings in the interpolators are found in Table C.3. The naming convention of all baryon interpolators is determined by Tables C.2 and C.3. In the Λ channels, singlet and octet interpolators are collected in one set. We assign to the first octet interpolator the number after the last singlet interpolator, and continue to count for the remaining octet interpolators. In the Σ and Ξ channels, the same holds for octet and decuplet interpolators.

Spin	Flavor channel	Name	Interpolator
$\frac{1}{2}$	Nucleon	$N^{(i)}_{1/2}$	$\epsilon_{abc}\,\Gamma^{(i)}_1\,u_a\left(u_b^T\,\Gamma^{(i)}_2\,d_c - d_b^T\,\Gamma^{(i)}_2\,u_c\right)$
$\frac{1}{2}$	Delta	$\Delta_{1/2}$	$\epsilon_{abc}\,\gamma_i\gamma_5 u_a\left(u_b^T\,C\,\gamma_i\,u_c\right)$
$\frac{1}{2}$	Sigma octet	$\Sigma^{(8,i)}_{1/2}$	$\epsilon_{abc}\,\Gamma^{(i)}_1\,u_a\left(u_b^T\,\Gamma^{(i)}_2\,s_c - s_b^T\,\Gamma^{(i)}_2\,u_c\right)$
$\frac{1}{2}$	Sigma decuplet	$\Sigma^{(10,i)}_{1/2}$	$\epsilon_{abc}\,\gamma_i\gamma_5 u_a\left(u_b^T\,C\,\gamma_i\,s_c - s_b^T\,C\,\gamma_i\,u_c\right)$
$\frac{1}{2}$	Xi octet	$\Xi^{(8,i)}_{1/2}$	$\epsilon_{abc}\,\Gamma^{(i)}_1\,s_a\left(s_b^T\,\Gamma^{(i)}_2\,u_c - u_b^T\,\Gamma^{(i)}_2\,s_c\right)$
$\frac{1}{2}$	Xi decuplet	$\Xi^{(10,i)}_{1/2}$	$\epsilon_{abc}\,\gamma_i\gamma_5 s_a\left(s_b^T\,C\,\gamma_i\,u_c - u_b^T\,C\,\Gamma_i\,s_c\right)$
$\frac{1}{2}$	Lambda singlet	$\Lambda^{(1,i)}_{1/2}$	$\epsilon_{abc}\Gamma^{(i)}_1 u_a(d_b^T\Gamma^{(i)}_2 s_c - s_b^T\Gamma^{(i)}_2 d_c)$
			$+$ cyclic permutations of u, d, s
$\frac{1}{2}$	Lambda octet	$\Lambda^{(8,i)}_{1/2}$	$\epsilon_{abc}\Big[\Gamma^{(i)}_1 s_a(u_b^T\Gamma^{(i)}_2 d_c - d_b^T\Gamma^{(i)}_2 u_c)$
			$+\,\Gamma^{(i)}_1 u_a(s_b^T\Gamma^{(i)}_2 d_c) - \Gamma^{(i)}_1 d_a(s_b^T\Gamma^{(i)}_2 u_c)\Big]$
$\frac{1}{2}$	Omega	$\Omega_{1/2}$	$\epsilon_{abc}\,\gamma_i\gamma_5 s_a\left(s_b^T\,C\,\gamma_i\,s_c\right)$
$\frac{3}{2}$	Nucleon	$N^{(i)}_{3/2}$	$\epsilon_{abc}\,\gamma_5\,u_a\left(u_b^T\,C\gamma_5\gamma_i\,d_c - d_b^T\,C\gamma_5\gamma_i\,u_c\right)$
$\frac{3}{2}$	Delta	$\Delta^{(i)}_{3/2}$	$\epsilon_{abc}\,u_a\left(u_b^T\,C\,\gamma_i\,u_c\right)$
$\frac{3}{2}$	Sigma octet	$\Sigma^{(8,i)}_{3/2}$	$\epsilon_{abc}\,\gamma_5\,u_a\left(u_b^T\,C\gamma_5\gamma_i\,s_c - s_b^T\,C\gamma_5\gamma_i\,u_c\right)$
$\frac{3}{2}$	Sigma decuplet	$\Sigma^{(10,i)}_{3/2}$	$\epsilon_{abc}\,u_a\left(u_b^T\,C\gamma_i\,s_c - s_b^T\,C\gamma_i\,u_c\right)$
$\frac{3}{2}$	Xi octet	$\Xi^{(8,i)}_{3/2}$	$\epsilon_{abc}\,\gamma_5\,s_a\left(s_b^T\,C\gamma_5\gamma_i\,u_c - u_b^T\,C\gamma_5\gamma_i\,s_c\right)$
$\frac{3}{2}$	Xi decuplet	$\Xi^{(10,i)}_{3/2}$	$\epsilon_{abc}\,s_a\left(s_b^T\,C\gamma_i\,u_c - u_b^T\,C\gamma_i\,s_c\right)$
$\frac{3}{2}$	Lambda singlet	$\Lambda^{(1,i)}_{3/2}$	$\epsilon_{abc}\gamma_5 u_a(d_b^T C\gamma_5\gamma_i s_c - s_b^T C\gamma_5\gamma_i d_c)$
			$+$ cyclic permutations of u, d, s
$\frac{3}{2}$	Lambda octet	$\Lambda^{(8,i)}_{3/2}$	$\epsilon_{abc}\Big[\gamma_5 s_a(u_b^T C\gamma_5\gamma_i d_c - d_b^T C\gamma_5\gamma_i u_c)$
			$+\,\gamma_5 u_a(s_b^T C\gamma_5\gamma_i d_c) - \gamma_5 d_a(s_b^T C\gamma_5\gamma_i u_c\Big]$
$\frac{3}{2}$	Omega	$\Omega^{(i)}_{3/2}$	$\epsilon_{abc}\,s_a\left(s_b^T\,C\,\gamma_i\,s_c\right)$

Table C.1: Baryon interpolators: Flavor structure. The possible choices for the Dirac matrices $\Gamma^{(i)}_{1,2}$ in the spin 1/2 channels are listed in Table C.2. All interpolators are projected to definite parity according to Eq. (C.1). All spin 3/2 interpolators include the Rarita-Schwinger projector, according to Eq. (C.4), which is suppressed for clarity in the table. C denotes the charge conjugation matrix, γ_i the spatial Dirac matrices and γ_t the Dirac matrix in time direction. Spin 1/2 and spin 3/2 channels are separated by a dashed line. Summation convention applies for repeated indices, and in the case of spin 3/2 observables, the open Lorentz index (after spin projection) is summed after taking the expectation value of correlation functions.

i	$\Gamma_1^{(i)}$	$\Gamma_2^{(i)}$	Numbering of associated interpolators	
			$N_{1/2}, \Lambda^1_{1/2}, \Sigma^8_{1/2}, \Xi^8_{1/2}$	$\Lambda^8_{1/2}, \Sigma^{10}_{1/2}, \Xi^{10}_{1/2}$
1	$\mathbb{1}$	$C\gamma_5$	1-8	25-32
2	γ_5	C	9-16	33-40
3	$i\mathbb{1}$	$C\gamma_t\gamma_5$	17-24	41-48

Table C.2: Baryon interpolators: Dirac structures used for the spin 1/2 nucleon, Λ, Σ and Ξ interpolators, according to Table C.1. The naming convention for associated interpolators in the different channels is given as well. The subscripts denotes the spin, the superscripts the flavor irreducible representation.

quark smearing types	Numbering of associated interpolators			
	$\Delta_{1/2}, \Delta_{3/2}, \Omega_{1/2}, \Omega_{3/2}$, $N_{3/2}, \Lambda^1_{3/2}, \Sigma^8_{3/2}, \Xi^8_{3/2}$	$\Lambda^8_{3/2}$, $\Sigma^{10}_{3/2}, \Xi^{10}_{3/2}$	$N_{1/2}, \Lambda^1_{1/2}$, $\Sigma^8_{1/2}, \Xi^8_{1/2}$	$\Lambda^8_{1/2}$, $\Sigma^{10}_{1/2}, \Xi^{10}_{1/2}$
(nn)n	1	9	1,9,17	25,33,41
(nn)w	2	10	2,10,18	26,34,42
(nw)n	3	11	3,11,19	27,35,43
(nw)w	4	12	4,12,20	28,36,44
(wn)n	5	13	5,13,21	29,37,45
(wn)w	6	14	6,14,22	30,38,46
(ww)n	7	15	7,15,23	31,39,47
(ww)w	8	16	8,16,24	32,40,48

Table C.3: Baryon interpolators: Quark smearing types and naming convention for the interpolators in the different channels. The subscripts denotes the spin, the superscripts the flavor irreducible representation. The brackets in the first row symbolize the diquark. Due to Fierz identities, some of the interpolators may be linearly dependent.

Appendix D

Details of Fits and Results

In this chapter we collect further details concerning fits and results. The enegy levels and the χ^2/d.o.f. of the fits in m_π^2 of light isovector, strange and isoscalar mesons are listed in Tables D.1, D.2 and D.3, respectively. The enegy levels and the χ^2/d.o.f of the fits in m_π^2 of positive and negative parity baryons are found in Tables D.4 and D.5, respectively. The enegy levels and the χ^2/d.o.f of the fits in m_π^2 after extrapolation to infinite volume are found in Table D.6. Possible origins of poor χ^2/d.o.f. larger than three are discussed in the main text.

Light meson	Energy level [MeV]	χ^2/d.o.f.
0^{-+}	1407(103)	8.25/5
0^{++}	976(70)	12.38/5
0^{++}	1689(103)	6.70/4
1^{--}	772(13)	4.65/5
1^{--}	1528(115)	2.79/5
1^{--}	1733(143)	2.51/4
1^{-+}	1370(260)	3.78/5
1^{+-}	1347(26)	8.12/5
1^{++}	1238(33)	9.62/5
1^{++}	1754(103)	4.91/5
$2^{--}(T_2)$	1849(222)	3.77/2
$2^{--}(E)$	1965(183)	2.16/3
$2^{-+}(T_2)$	1745(96)	5.06/5
$2^{-+}(E)$	1889(139)	8.96/4
$2^{++}(T_2)$	1399(66)	16.51/5
$2^{++}(E)$	1379(60)	6.03/5

Table D.1: Energy levels at the physical point and corresponding χ^2/d.o.f. for the chiral fits of the isovector light meson energy levels reported in this work. Sources of large χ^2/d.o.f. (≥ 3) are discussed in the text.

Strange meson	Energy level [MeV]	χ^2/d.o.f.
0^-	509(4)	20.83/5
0^-	1434(64)	6.94/5
0^+	884(36)	41.53/5
0^+	1323(81)	6.92/5
1^-	896(9)	7.20/5
1^-	1633(89)	1.57/3
1^-	1919(69)	1.05/3
1^+	1339(20)	3.90/5
1^+	1409(17)	6.76/5
1^+	1709(109)	2.56/5
$2^-(T_2)$	1750(54)	5.31/5
$2^-(T_2)$	1909(52)	2.21/5
$2^-(E)$	1870(75)	1.51/4
$2^-(E)$	1956(71)	1.17/4
$2^+(T_2)$	1452(51)	7.28/5
$2^+(E)$	1392(58)	5.68/5

Table D.2: Same as Table D.1, but for strange mesons.

Isoscalar meson	Energy level [MeV]	χ^2/d.o.f.
1^{--}	994(8)	6.51/5
1^{--}	1857(53)	7.30/5
1^{--}	1987(40)	1.41/5
$2^{++}(T_2)$	1581(29)	12.89/5
$2^{++}(E)$	1578(24)	7.28/5

Table D.3: Same as Table D.1, but for isoscalar mesons.

Baryon: $I(J^P)$	Energy level [MeV]	χ^2/d.o.f.
$N:\ 1/2(1/2^+)$	1000(18)	2.16/5
$N:\ 1/2(1/2^+)$	1848(120)	3.61/5
$N:\ 1/2(1/2^+)$	1998(59)	18.31/5
$N:\ 1/2(1/2^+)$	2543(280)	1.96/3
$\Delta:\ 3/2(1/2^+)$	1751(190)	1.58/5
$\Delta:\ 3/2(1/2^+)$	2211(126)	1.15/5
$\Lambda:\ 0(1/2^+)$	1140(14)	3.30/5
$\Lambda:\ 0(1/2^+)$	1809(94)	4.63/5
$\Lambda:\ 0(1/2^+)$	2113(54)	20.07/6
$\Lambda:\ 0(1/2^+)$	2139(68)	1.50/5
$\Sigma:\ 1(1/2^+)$	1216(15)	6.94/5
$\Sigma:\ 1(1/2^+)$	2069(74)	3.41/5
$\Sigma:\ 1(1/2^+)$	2149(66)	20.37/5
$\Sigma:\ 1(1/2^+)$	2335(63)	2.09/5
$\Xi:\ 1/2(1/2^+)$	1303(13)	8.31/5
$\Xi:\ 1/2(1/2^+)$	2178(48)	7.51/5
$\Xi:\ 1/2(1/2^+)$	2231(44)	26.53/5
$\Xi:\ 1/2(1/2^+)$	2408(45)	10.37/5
$\Omega:\ 0(1/2^+)$	2350(63)	4.14/5
$\Omega:\ 0(1/2^+)$	2481(51)	4.35/5
$N:\ 1/2(3/2^+)$	1773(91)	8.35/5
$N:\ 1/2(3/2^+)$	2298(191)	3.79/5
$\Delta:\ 3/2(3/2^+)$	1344(27)	6.13/5
$\Delta:\ 3/2(3/2^+)$	2204(82)	6.23/5
$\Lambda:\ 0(3/2^+)$	1914(72)	5.80/5
$\Lambda:\ 0(3/2^+)$	2061(138)	23.04/5
$\Lambda:\ 0(3/2^+)$	2483(111)	4.26/5
$\Sigma:\ 1(3/2^+)$	1471(23)	2.52/5
$\Sigma:\ 1(3/2^+)$	2194(81)	4.78/5
$\Sigma:\ 1(3/2^+)$	2250(79)	7.05/5
$\Sigma:\ 1(3/2^+)$	2468(67)	4.22/5
$\Xi:\ 1/2(3/2^+)$	1553(18)	3.78/5
$\Xi:\ 1/2(3/2^+)$	2228(40)	6.99/5
$\Xi:\ 1/2(3/2^+)$	2398(52)	7.03/5
$\Xi:\ 1/2(3/2^+)$	2574(52)	4.26/5
$\Omega:\ 0(3/2^+)$	1642(17)	10.86/5
$\Omega:\ 0(3/2^+)$	2470(49)	8.14/5

Table D.4: Same as Table D.1, but for positive parity baryons. The horizontal dashed line separates spin 1/2 and spin 3/2 baryons.

Baryon: $I(J^P)$	Energy level [MeV]	χ^2/d.o.f.
$N:\ 1/2(1/2^-)$	1406(49)	6.51/5
$N:\ 1/2(1/2^-)$	1539(69)	8.72/5
$N:\ 1/2(1/2^-)$	1895(128)	6.35/5
$N:\ 1/2(1/2^-)$	1918(211)	5.94/5
$\Delta:\ 3/2(1/2^-)$	1454(140)	11.16/5
$\Delta:\ 3/2(1/2^-)$	1914(322)	3.24/5
$\Lambda:\ 0(1/2^-)$	1447(46)	6.55/5
$\Lambda:\ 0(1/2^-)$	1611(53)	22.93/5
$\Lambda:\ 0(1/2^-)$	1767(41)	31.18/5
$\Lambda:\ 0(1/2^-)$	2473(182)	13.56/5
$\Sigma:\ 1(1/2^-)$	1603(38)	7.45/5
$\Sigma:\ 1(1/2^-)$	1718(58)	12.78/5
$\Sigma:\ 1(1/2^-)$	1730(34)	10.79/5
$\Sigma:\ 1(1/2^-)$	2478(104)	11.94/5
$\Xi:\ 1/2(1/2^-)$	1716(43)	19.10/5
$\Xi:\ 1/2(1/2^-)$	1837(28)	20.25/5
$\Xi:\ 1/2(1/2^-)$	1844(43)	15.75/5
$\Xi:\ 1/2(1/2^-)$	2758(78)	5.61/5
$\Omega:\ 0(1/2^-)$	1944(56)	20.48/5
$\Omega:\ 0(1/2^-)$	2716(118)	8.58/5
$N:\ 1/2(3/2^-)$	1634(44)	14.75/5
$N:\ 1/2(3/2^-)$	1982(128)	7.40/5
$N:\ 1/2(3/2^-)$	2296(129)	9.59/5
$\Delta:\ 3/2(3/2^-)$	1570(67)	4.01/5
$\Delta:\ 3/2(3/2^-)$	2373(140)	17.97/5
$\Lambda:\ 0(3/2^-)$	1729(32)	2.39/5
$\Lambda:\ 0(3/2^-)$	2205(106)	3.97/5
$\Lambda:\ 0(3/2^-)$	2382(86)	6.48/5
$\Sigma:\ 1(3/2^-)$	1861(26)	6.33/5
$\Sigma:\ 1(3/2^-)$	1736(40)	2.25/5
$\Sigma:\ 1(3/2^-)$	2394(74)	9.73/5
$\Sigma:\ 1(3/2^-)$	2297(122)	3.90/5
$\Xi:\ 1/2(3/2^-)$	1906(29)	3.12/5
$\Xi:\ 1/2(3/2^-)$	1894(38)	3.19/5
$\Xi:\ 1/2(3/2^-)$	2497(61)	8.53/5
$\Xi:\ 1/2(3/2^-)$	2426(73)	7.60/5
$\Omega:\ 0(3/2^-)$	2049(32)	7.32/5
$\Omega:\ 0(3/2^-)$	2755(67)	5.68/5

Table D.5: Same as Table D.1, but for negative parity baryons. The horizontal dashed line separates spin 1/2 and spin 3/2 baryons.

Hadron	$I(J^P)$	Energy level [MeV]	χ^2/d.o.f.
K	$1/2(0^-)$	504(4)	23.26/5
K^*	$1/2(1^-)$	865(9)	5.31/5
N	$1/2(1/2^+)$	954(16)	2.26/5
Λ	$0(1/2^+)$	1112(14)	4.44/5
Σ	$1(1/2^+)$	1156(15)	11.78/5
Ξ	$1/2(1/2^+)$	1273(12)	11.93/5
Δ	$3/2(3/2^+)$	1268(32)	8.67/5
Ω	$0(3/2^+)$	1620(14)	11.26/5

Table D.6: Same as Table D.1, but for hadrons after the infinite volume extrapolation. The horizontal dashed line separates mesons and baryons.

Bibliography

[1] **BGR [Bern-Graz-Regensburg]** Collaboration, G. P. Engel, C. Gattringer, C. Lang, M. Limmer, D. Mohler, and A. Schäfer, *Excited hadrons in n_f=2 QCD*, *PoS* **LAT2009** (2009) 088, [`arXiv:0910.2802`].

[2] **BGR [Bern-Graz-Regensburg]** Collaboration, G. P. Engel, C. Gattringer, L. Y. Glozman, C. Lang, M. Limmer, D. Mohler, and A. Schäfer, *Baryon axial charges from Chirally Improved fermions - first results*, *PoS* **LAT2009** (2009) 135, [`arXiv:0910.4190`].

[3] **BGR [Bern-Graz-Regensburg]** Collaboration, G. P. Engel, C. B. Lang, M. Limmer, D. Mohler, and A. Schäfer, *Some results on excited hadrons in 2-flavor QCD*, *PoS* **LATTICE2010** (2010) 103, [`arXiv:1010.2366`].

[4] **BGR [Bern-Graz-Regensburg]** Collaboration, G. P. Engel, C. B. Lang, M. Limmer, D. Mohler, and A. Schäfer, *Meson and baryon spectrum for QCD with two light dynamical quarks*, *Phys. Rev.* **D82** (2010) 034505, [`arXiv:1005.1748`].

[5] **BGR [Bern-Graz-Regensburg]** Collaboration, G. P. Engel, C. B. Lang, M. Limmer, D. Mohler, and A. Schäfer, *QCD with two light dynamical chirally improved quarks: Mesons*, *Phys. Rev.* **D85** (2012) 034508, [`arXiv:1112.1601`].

[6] **BGR [Bern-Graz-Regensburg]** Collaboration, G. P. Engel, C. B. Lang, M. Limmer, D. Mohler, and A. Schäfer, *Excited meson spectroscopy with two chirally improved quarks*, *PoS* **LATTICE2011** (2011) 119, [`arXiv:1112.1198`].

[7] **Particle Data Group** Collaboration, K. Nakamura *et al.*, *Review of particle physics*, *J. Phys.* **G37** (2010) 075021.

[8] M. Gell-Mann, *A Schematic Model of Baryons and Mesons*, *Phys.Lett.* **8** (1964) 214–215.

[9] G. Zweig, *An SU(3) model for strong interaction symmetry and its breaking*, .

[10] H. Fritzsch, M. Gell-Mann, and H. Leutwyler, *Advantages of the Color Octet Gluon Picture*, *Phys. Lett.* **B47** (1973) 365–368.

[11] S. Weinberg, *Phenomenological Lagrangians*, *Physica* **A96** (1979) 327.

[12] J. Gasser and H. Leutwyler, *Chiral Perturbation Theory: Expansions in the Mass of the Strange Quark*, *Nucl. Phys.* **B250** (1985) 465.

[13] Y. Nambu and G. Jona-Lasinio, *Dynamical model of elementary particles based on an analogy with superconductivity. I*, *Phys. Rev.* **122** (1961) 345–358.

[14] Y. Nambu and G. Jona-Lasinio, *Dynamical model of elementary particles based on an analogy with superconductivity. II*, *Phys. Rev.* **124** (1961) 246–254.

[15] K. G. Wilson, *Confinement of quarks*, *Phys. Rev.* **D10** (1974) 2445–2459.

[16] H. B. Nielsen and M. Ninomiya, *No Go Theorem for Regularizing Chiral Fermions*, *Phys. Lett.* **B105** (1981) 219.

[17] P. H. Ginsparg and K. G. Wilson, *A Remnant of Chiral Symmetry on the Lattice*, *Phys. Rev.* **D25** (1982) 2649.

[18] H. Neuberger, *Exactly massless quarks on the lattice*, *Phys. Lett.* **B417** (1998) 141–144, [`hep-lat/9707022`].

[19] H. Neuberger, *More about exactly massless quarks on the lattice*, *Phys. Lett.* **B427** (1998) 353–355, [`hep-lat/9801031`].

[20] D. B. Kaplan, *A Method for simulating chiral fermions on the lattice*, *Phys. Lett.* **B288** (1992) 342–347, [`hep-lat/9206013`].

[21] V. Furman and Y. Shamir, *Axial symmetries in lattice QCD with Kaplan fermions*, *Nucl. Phys.* **B439** (1995) 54–78, [`hep-lat/9405004`].

[22] P. Hasenfratz and F. Niedermayer, *Perfect lattice action for asymptotically free theories*, *Nucl. Phys.* **B414** (1994) 785–814, [`hep-lat/9308004`].

[23] A. Hasenfratz, P. Hasenfratz, and F. Niedermayer, *Simulating full QCD with the fixed point action*, *Phys. Rev.* **D72** (2005) 114508, [`hep-lat/0506024`].

[24] M. Lüscher, *Exact chiral symmetry on the lattice and the Ginsparg- Wilson relation*, *Phys. Lett.* **B428** (1998) 342–345, [`hep-lat/9802011`].

[25] C. Gattringer, *A new approach to Ginsparg-Wilson fermions*, *Phys. Rev.* **D63** (2001) 114501, [`hep-lat/0003005`].

[26] C. Gattringer, I. Hip, and C. B. Lang, *Approximate Ginsparg-Wilson fermions: A first test*, *Nucl. Phys.* **B597** (2001) 451–474, [`hep-lat/0007042`].

[27] C. Gattringer and I. Hip, *New approximate solutions of the Ginsparg-Wilson equation: Tests in 2-d*, *Phys. Lett.* **B480** (2000) 112–118, [`hep-lat/0002002`].

[28] C. Gattringer and C. B. Lang, *Improving the Dirac operator in lattice QCD*, *Comput. Phys. Commun.* **147** (2002) 398–401, [hep-lat/0111043].

[29] **BGR** Collaboration, C. Gattringer *et al.*, *Quenched spectroscopy with fixed-point and chirally improved fermions*, *Nucl. Phys.* **B677** (2004) 3–51, [hep-lat/0307013].

[30] **BGR(Bern-Graz-Regensburg)** Collaboration, T. Burch *et al.*, *Excited hadrons from improved interpolating fields*, *Nucl. Phys. Proc. Suppl.* **140** (2005) 284–286, [hep-lat/0409014].

[31] T. Burch *et al.*, *Masses of excited baryons from chirally improved quenched lattice QCD*, *Nucl. Phys.* **A755** (2005) 481–484, [nucl-th/0501025].

[32] T. Burch, C. Gattringer, L. Y. Glozman, C. Hagen, and C. B. Lang, *Variational method for lattice spectroscopy with ghosts*, *Phys. Rev.* **D73** (2006) 017502, [hep-lat/0511054].

[33] **Bern-Graz-Regensburg (BGR)** Collaboration, C. Gattringer, P. Huber, and C. B. Lang, *Lattice calculation of low energy constants with Ginsparg-Wilson type fermions*, *Phys. Rev.* **D72** (2005) 094510, [hep-lat/0509003].

[34] C. B. Lang, P. Majumdar, and W. Ortner, *QCD with two dynamical flavors of chirally improved quarks*, *Phys. Rev.* **D73** (2006) 034507, [hep-lat/0512014].

[35] T. Burch *et al.*, *Excited hadrons on the lattice: Baryons*, *Phys. Rev.* **D74** (2006) 014504, [hep-lat/0604019].

[36] T. Burch *et al.*, *Excited hadrons on the lattice: Mesons*, *Phys. Rev.* **D73** (2006) 094505, [hep-lat/0601026].

[37] W. Ortner, *Dynamical Chirally Improved fermions in lattice QCD*. PhD thesis, Karl-Franzens-Universität Graz, 2006. PhD thesis.

[38] T. Burch *et al.*, *B meson excitations with chirally improved light quarks*, *PoS* **LAT2007** (2007) 091, [arXiv:0709.3708].

[39] R. Frigori *et al.*, *Dynamical Chirally Improved Quarks: First Results for Hadron Masses*, *PoS* **LAT2007** (2007) 114, [arXiv:0709.4582].

[40] C. Gattringer, L. Y. Glozman, C. B. Lang, D. Mohler, and S. Prelovsek, *Derivative sources in lattice spectroscopy of excited mesons*, *Phys. Rev.* **D78** (2008) 034501, [arXiv:0802.2020].

[41] C. Gattringer *et al.*, *Hadron Spectroscopy with Dynamical Chirally Improved Fermions*, *Phys. Rev.* **D79** (2009) 054501, [arXiv:0812.1681].

[42] L. Y. Glozman, C. B. Lang, and M. Limmer, *The chiral and angular momentum content of the ρ- mesons in lattice QCD*, *PoS* **LATTICE2010** (2010) 149, [arXiv:1010.5660].

[43] L. Y. Glozman, C. B. Lang, and M. Limmer, *Effective chiral restoration in the rho'-meson in lattice QCD*, *Phys. Rev.* **D82** (2010) 097501, [arXiv:1007.1346].

[44] L. Y. Glozman, C. B. Lang, and M. Limmer, *Chiral symmetry breaking and the spin content of the rho and rho' mesons*, *Phys. Lett.* **B705** (2011) 129–133, [arXiv:1106.1010].

[45] L. Y. Glozman, C. B. Lang, and M. Limmer, *Chiral symmetry breaking and the spin content of hadrons*, arXiv:1111.2562.

[46] C. B. Lang and M. Schröck, *Effects of the low lying Dirac modes on the spectrum of ground state mesons*, *PoS* **LATTICE2011** (2011) 111, [arXiv:1110.6149].

[47] C. B. Lang and M. Schröck, *Unbreaking chiral symmetry*, *Phys. Rev.* **D84** (2011) 087704, [arXiv:1107.5195].

[48] M. E. Limmer, *Hadron properties in full QCD.* PhD thesis, Karl-Franzens Universität Graz, 2011.

[49] C. Michael, *Adjoint Sources in Lattice Gauge Theory*, *Nucl. Phys.* **B259** (1985) 58.

[50] M. Lüscher and U. Wolff, *How to calculate the elastic scattering matrix in two- dimensional quantum field theories by numerical simulation*, *Nucl. Phys.* **B339** (1990) 222–252.

[51] C. Morningstar, *Exploring Excited Hadrons*, *PoS* **LATTICE2008** (2008) 009, [arXiv:0810.4448].

[52] C. Alexandrou, C. N. Papanicolas, and E. Stiliaris, *A novel method for the determination of hadron excited states in Lattice QCD applied to the nucleon*, *PoS* **LATTICE2008** (2008) 099, [arXiv:0810.3982].

[53] **ETM** Collaboration, C. Alexandrou *et al.*, *The low-lying baryon spectrum with two dynamical twisted mass fermions*, *Phys. Rev.* **D80** (2009) 114503, [arXiv:0910.2419].

[54] T. Burch, C. Hagen, M. Hetzenegger, and A. Schafer, *Low and high spin mesons from $N_f = 2$ Clover-Wilson lattices*, *Phys. Rev.* **D79** (2009) 114503, [arXiv:0903.2358].

[55] J. M. Bulava *et al.*, *Excited State Nucleon Spectrum with Two Flavors of Dynamical Fermions*, *Phys. Rev.* **D79** (2009) 034505, [arXiv:0901.0027].

[56] G. T. Fleming, S. D. Cohen, H.-W. Lin, and V. Pereyra, *Excited-State Effective Masses in Lattice QCD*, *Phys. Rev.* **D80** (2009) 074506, [arXiv:0903.2314].

[57] S. Cohen *et al.*, *Excited-Nucleon Spectroscopy with 2+1 Fermion Flavors*, *PoS* **LAT2009** (2009) 112, [arXiv:0911.3373].

[58] M. S. Mahbub *et al.*, *Isolating Excited States of the Nucleon in Lattice QCD*, *Phys. Rev.* **D80** (2009) 054507, [arXiv:0905.3616].

[59] M. S. Mahbub *et al.*, *Low-lying positive-parity excited states of the nucleon*, *PoS* **LAT2009** (2009) 118, [arXiv:0910.2789].

[60] T. T. Takahashi and M. Oka, *Low-lying Λ Baryons with spin 1/2 in Two-flavor Lattice QCD*, *Phys. Rev.* **D81** (2010) 034505, [arXiv:0910.0686].

[61] J. Bulava *et al.*, *Nucleon, Δ and Ω excited states in $N_f = 2 + 1$ lattice QCD*, *Phys. Rev.* **D82** (2010) 014507, [arXiv:1004.5072].

[62] **CSSM Lattice** Collaboration, M. S. Mahbub, W. Kamleh, D. B. Leinweber, P. J. Moran, and A. G. Williams, *Roper Resonance in 2+1 Flavor QCD*, *Phys. Lett.* **B707** (2012) 389–393, [arXiv:1011.5724].

[63] M. S. Mahbub, A. O. Cais, W. Kamleh, D. B. Leinweber, and A. G. Williams, *Positive-parity Excited-states of the Nucleon in Quenched Lattice QCD*, *Phys. Rev.* **D82** (2010) 094504, [arXiv:1004.5455].

[64] J. J. Dudek, R. G. Edwards, M. J. Peardon, D. G. Richards, and C. E. Thomas, *Highly excited and exotic meson spectrum from dynamical lattice QCD*, *Phys. Rev. Lett.* **103** (2009) 262001, [arXiv:0909.0200].

[65] V. Drach, K. Jansen, J. Carbonell, M. Papinutto, and C. Alexandrou, *Low lying baryon spectrum with $N_f = 2 + 1 + 1$ dynamical twisted quarks*, *PoS* **LATTICE2010** (2010) 101, [arXiv:1012.3861].

[66] J. J. Dudek, R. G. Edwards, M. J. Peardon, D. G. Richards, and C. E. Thomas, *Toward the excited meson spectrum of dynamical QCD*, *Phys. Rev.* **D82** (2010) 034508, [arXiv:1004.4930].

[67] C. Morningstar *et al.*, *The excited hadron spectrum in lattice QCD using a new method of estimating quark propagation*, *AIP Conf. Proc.* **1257** (2010) 779–783, [arXiv:1002.0818].

[68] J. J. Dudek, *The lightest hybrid meson supermultiplet in QCD*, *Phys.Rev.* **D84** (2011) 074023, [arXiv:1106.5515].

[69] J. J. Dudek *et al.*, *Isoscalar meson spectroscopy from lattice QCD*, *Phys. Rev.* **D83** (2011) 111502, [arXiv:1102.4299].

[70] R. G. Edwards, J. J. Dudek, D. G. Richards, and S. J. Wallace, *Excited state baryon spectroscopy from lattice QCD*, arXiv:1104.5152.

[71] C. Morningstar *et al.*, *Improved stochastic estimation of quark propagation with Laplacian Heaviside smearing in lattice QCD*, *Phys. Rev.* **D83** (2011) 114505, [arXiv:1104.3870].

[72] C. Hoelbling, *Light hadron spectroscopy and pseudoscalar decay constants*, *PoS* **LATTICE2010** (2010) 011, [arXiv:1102.0410].

[73] J. Bulava, *Progress on Excited Hadrons in Lattice QCD*, arXiv:1112.0212.

[74] D. Nicmorus, G. Eichmann, A. Krassnigg, and R. Alkofer, *Delta-baryon mass in a covariant Faddeev approach*, *Phys. Rev.* **D80** (2009) 054028, [arXiv:0812.1665].

[75] G. Eichmann, R. Alkofer, A. Krassnigg, and D. Nicmorus, *Nucleon mass from a covariant three-quark Faddeev equation*, *Phys. Rev. Lett.* **104** (2010) 201601, [arXiv:0912.2246].

[76] A. Krassnigg, *Survey of J=0,1 mesons in a Bethe-Salpeter approach*, *Phys. Rev.* **D80** (2009) 114010, [arXiv:0909.4016].

[77] M. Blank, A. Krassnigg, and A. Maas, *Rho-meson, Bethe-Salpeter equation, and the far infrared*, *Phys. Rev.* **D83** (2011) 034020, [arXiv:1007.3901].

[78] A. Krassnigg and M. Blank, *A covariant study of tensor mesons*, *Phys. Rev.* **D83** (2011) 096006, [arXiv:1011.6650].

[79] V. Bernard, M. Lage, U. G. Meissner, and A. Rusetsky, *Scalar mesons in a finite volume*, *JHEP* **01** (2011) 019, [arXiv:1010.6018].

[80] J. R. Pelaez and G. Rios, *Chiral extrapolation of light resonances from one and two- loop unitarized Chiral Perturbation Theory versus lattice results*, *Phys. Rev.* **D82** (2010) 114002, [arXiv:1010.6008].

[81] M. Döring, U.-G. Meissner, E. Oset, and A. Rusetsky, *Unitarized Chiral Perturbation Theory in a finite volume: scalar meson sector*, *Eur. Phys. J.* **A47** (2011) 139, [arXiv:1107.3988].

[82] M. Döring and U. G. Meissner, *Finite volume effects in pion-kaon scattering and reconstruction of the kappa(800) resonance*, `arXiv:1111.0616`.

[83] H. L. L. Roberts, L. Chang, I. C. Cloet, and C. D. Roberts, *Masses of ground and excited-state hadrons*, *Few Body Syst.* **51** (2011) 1–25, [`arXiv:1101.4244`].

[84] H. Sanchis-Alepuz, G. Eichmann, S. Villalba-Chavez, and R. Alkofer, *Delta and Omega masses in a three-quark covariant Faddeev approach*, *Phys. Rev.* **D84** (2011) 096003, [`arXiv:1109.0199`].

[85] **CP-PACS** Collaboration, S. Aoki *et al.*, *Lattice QCD Calculation of the ρ Meson Decay Width*, *Phys. Rev.* **D76** (2007) 094506, [`arXiv:0708.3705`].

[86] K. Sasaki and N. Ishizuka, *I=2 Two-Pion Wave Function and Scattering Phase Shift*, *Phys. Rev.* **D78** (2008) 014511, [`arXiv:0804.2941`].

[87] **QCDSF** Collaboration, M. Göckeler *et al.*, *Extracting the rho resonance from lattice QCD simulations at small quark masses*, *PoS* **LATTICE2008** (2008) 136, [`arXiv:0810.5337`].

[88] X. Feng, K. Jansen, and D. B. Renner, *The pi+ pi+ scattering length from maximally twisted mass lattice QCD*, *Phys. Lett.* **B684** (2010) 268–274, [`arXiv:0909.3255`].

[89] X. Feng, K. Jansen, and D. B. Renner, *Resonance Parameters of the rho-Meson from Lattice QCD*, *Phys. Rev.* **D83** (2011) 094505, [`arXiv:1011.5288`].

[90] **CS** Collaboration, S. Aoki *et al.*, *ρ Meson Decay in 2+1 Flavor Lattice QCD*, *Phys. Rev.* **D84** (2011) 094505, [`arXiv:1106.5365`].

[91] **NPLQCD** Collaboration, S. R. Beane *et al.*, *The I=2 pipi S-wave Scattering Phase Shift from Lattice QCD*, *Phys. Rev.* **D85** (2012) 034505, [`arXiv:1107.5023`].

[92] Z. Fu, *Lattice QCD calculation of $\pi\pi$ scattering length*, *Commun. Theor. Phys.* **57** (2012) 78–84, [`arXiv:1110.3918`].

[93] C. B. Lang, D. Mohler, S. Prelovsek, and M. Vidmar, *Coupled channel analysis of the rho meson decay in lattice QCD*, *Phys. Rev.* **D84** (2011) 054503, [`arXiv:1105.5636`].

[94] C. Pelissier, A. Alexandru, and F. X. Lee, *ρ meson decay on asymmetrical lattices*, `arXiv:1111.2314`.

[95] S. Prelovsek, C. B. Lang, D. Mohler, and M. Vidmar, *Decay of rho and a1 mesons on the lattice using distillation*, *PoS* **LATTICE2011** (2011) 137, [arXiv:1111.0409].

[96] T. Yagi, S. Hashimoto, O. Morimatsu, and M. Ohtani, *I=2 π-π scattering length with dynamical overlap fermion*, arXiv:1108.2970.

[97] M. Lüscher, *Volume Dependence of the Energy Spectrum in Massive Quantum Field Theories. 2. Scattering States*, *Commun. Math. Phys.* **105** (1986) 153–188.

[98] M. Lüscher, *Two particle states on a torus and their relation to the scattering matrix*, *Nucl. Phys.* **B354** (1991) 531–578.

[99] M. Lüscher, *Signatures of unstable particles in finite volume*, *Nucl. Phys.* **B364** (1991) 237–254.

[100] K. Rummukainen and S. A. Gottlieb, *Resonance scattering phase shifts on a nonrest frame lattice*, *Nucl. Phys.* **B450** (1995) 397–436, [hep-lat/9503028].

[101] C. h. Kim, C. T. Sachrajda, and S. R. Sharpe, *Finite-volume effects for two-hadron states in moving frames*, *Nucl. Phys.* **B727** (2005) 218–243, [hep-lat/0507006].

[102] V. Bernard, M. Lage, U.-G. Meissner, and A. Rusetsky, *Resonance properties from the finite-volume energy spectrum*, *JHEP* **08** (2008) 024, [arXiv:0806.4495].

[103] P. Giudice, D. McManus, and M. Peardon, *Extracting resonance parameters from lattice data*, *PoS* **LATTICE2010** (2010) 105, [arXiv:1009.6192].

[104] U.-G. Meissner, K. Polejaeva, and A. Rusetsky, *Extraction of the resonance parameters at finite times*, *Nucl. Phys.* **B846** (2011) 1–20, [arXiv:1007.0860].

[105] **ETM** Collaboration, X. Feng, K. Jansen, and D. B. Renner, *A new moving frame to extract scattering phases in lattice QCD*, *PoS* **LAT2010** (2010) 104, [arXiv:1104.0058].

[106] T. Luu and M. J. Savage, *Extracting Scattering Phase-Shifts in Higher Partial-Waves from Lattice QCD Calculations*, *Phys. Rev.* **D83** (2011) 114508, [arXiv:1101.3347].

[107] L. Leskovec and S. Prelovsek, *Scattering phase shifts for two particles of different mass and non-zero total momentum in lattice QCD*, arXiv:1202.2145.

[108] J. Goldstone, *Field Theories with Superconductor Solutions*, *Nuovo Cim.* **19** (1961) 154–164.

[109] J. Goldstone, A. Salam, and S. Weinberg, *Broken Symmetries*, *Phys. Rev.* **127** (1962) 965–970.

[110] E. Seiler, *Gauge Theories as a Problem of Constructive Quantum Field Theory and Statistical Mechanics*, vol. 159. Springer Lecture Notes in Physics, 1982.

[111] C. Rebbi, *Lattice Gauge Theories and Monte Carlo Simulations*. World Scientific, Singapor, 1983.

[112] M. Creutz, *Quarks, Gluons and Lattices*. Cambridge University Press, Cambrigdge UK, 1983.

[113] M. Creutz, *Quantum Fields on the Computer*. World Scientific, Singapore, 1992.

[114] I. Montvay and G. Münster, *Quantum Fields on a Lattice*. Cambridge University Press, Cambridge UK, 1994.

[115] J. Smit, *Introduction to Quantum Fields on a Lattice*. Cambridge University Press, Cambridge, 2002.

[116] H. J. Rothe, *Lattice gauge theories: An Introduction*, vol. 74. World Sci. Lect. Notes Phys., 2005.

[117] T. DeGrand and C. E. DeTar, *Lattice methods for quantum chromodynamics*. World Scientific, New Jersey, 2006.

[118] C. Gattringer and C. B. Lang, *Quantum chromodynamics on the lattice*, vol. 788. Springer Lecture Notes in Physics, 2010.

[119] K. Symanzik, *Continuum Limit and Improved Action in Lattice Theories. 1. Principles and phi**4 Theory*, *Nucl. Phys.* **B226** (1983) 187.

[120] K. Symanzik, *Continuum Limit and Improved Action in Lattice Theories. 2. O(N) Nonlinear Sigma Model in Perturbation Theory*, *Nucl. Phys.* **B226** (1983) 205.

[121] R. C. Johnson, *Angular momentum on a lattice*, *Phys. Lett.* **B114** (1982) 147.

[122] J. J. Dudek, R. G. Edwards, N. Mathur, and D. G. Richards, *Charmonium excited state spectrum in lattice QCD*, *Phys. Rev.* **D77** (2008) 034501, [arXiv:0707.4162].

[123] M. Lüscher and P. Weisz, *On-Shell Improved Lattice Gauge Theories*, *Commun. Math. Phys.* **97** (1985) 59.

[124] M. Lüscher and P. Weisz, *Computation of the Action for On-Shell Improved Lattice Gauge Theories at Weak Coupling*, *Phys. Lett.* **B158** (1985) 250.

[125] M. G. Alford, W. Dimm, G. P. Lepage, G. Hockney, and P. B. Mackenzie, *Lattice QCD on small computers*, *Phys. Lett.* **B361** (1995) 87–94, [hep-lat/9507010].

[126] C. Morningstar and M. J. Peardon, *Analytic smearing of SU(3) link variables in lattice QCD*, *Phys. Rev.* **D69** (2004) 054501, [hep-lat/0311018].

[127] M. Creutz, *Monte Carlo Study of Quantized SU(2) Gauge Theory*, *Phys. Rev.* **D21** (1980) 2308–2315.

[128] S. L. Adler, *An overrelaxation method for the monte carlo evaluation of the partition function for multiquadratic actions*, *Phys. Rev.* **D23** (1981) 2901.

[129] C. Whitmer, *Overrelaxation methods for monte carlo simulations of quadratic and multiquadratic actions*, *Phys. Rev.* **D29** (1984) 306–311.

[130] D. H. Weingarten and D. N. Petcher, *Monte Carlo Integration for Lattice Gauge Theories with Fermions*, *Phys. Lett.* **B99** (1981) 333.

[131] S. Duane, A. D. Kennedy, B. J. Pendleton, and D. Roweth, *Hybrid Monte Carlo*, *Phys. Lett.* **B195** (1987) 216–222.

[132] S. A. Gottlieb, W. Liu, D. Toussaint, R. L. Renken, and R. L. Sugar, *Hybrid Molecular Dynamics Algorithms for the Numerical Simulation of Quantum Chromodynamics*, *Phys. Rev.* **D35** (1987) 2531–2542.

[133] L. Lellouch, R. Sommer, B. Svetitsky, A. Vladikas, and L. F. Cugliandolo, *Modern perspectives in lattice QCD: Quantum field theory and high performance computing. Proceedings, International School, 93rd Session, Les Houches, France, August 3-28, 2009*, .

[134] **ALPHA** Collaboration, S. Schaefer, R. Sommer, and F. Virotta, *Critical slowing down and error analysis in lattice QCD simulations*, *Nucl. Phys.* **B845** (2011) 93–119, [arXiv:1009.5228].

[135] M. Lüscher and S. Schaefer, *Non-renormalizability of the HMC algorithm*, *JHEP* **04** (2011) 104, [arXiv:1103.1810].

[136] M. Lüscher, *Schwarz-preconditioned HMC algorithm for two-flavour lattice QCD*, *Comput. Phys. Commun.* **165** (2005) 199–220, [hep-lat/0409106].

[137] M. Lüscher, *Trivializing maps, the Wilson flow and the HMC algorithm*, *Commun. Math. Phys.* **293** (2010) 899–919, [arXiv:0907.5491].

[138] G. P. Engel and S. Schaefer, *Testing trivializing maps in the Hybrid Monte Carlo algorithm*, arXiv:1102.1852.

[139] M. Lüscher and S. Schaefer, *Lattice QCD without topology barriers*, *JHEP* **07** (2011) 036, [arXiv:1105.4749].

[140] M. Hasenbusch, *Speeding up the Hybrid-Monte-Carlo algorithm for dynamical fermions*, *Phys. Lett.* **B519** (2001) 177–182, [hep-lat/0107019].

[141] R. C. Brower, T. Ivanenko, A. R. Levi, and K. N. Orginos, *Chronological inversion method for the Dirac matrix in hybrid Monte Carlo*, *Nucl. Phys.* **B484** (1997) 353–374, [hep-lat/9509012].

[142] S. Dürr *et al.*, *Scaling study of dynamical smeared-link clover fermions*, *Phys. Rev.* **D79** (2009) 014501, [arXiv:0802.2706].

[143] I. P. Omelyan, I. M. Mryglod, and R. F. C *Comput. Phys. Commun.* **151** (2003) 272.

[144] J. C. Sexton and D. H. Weingarten, *Hamiltonian evolution for the hybrid Monte Carlo algorithm*, *Nucl. Phys.* **B380** (1992) 665–678.

[145] C. Urbach, K. Jansen, A. Shindler, and U. Wenger, *HMC algorithm with multiple time scale integration and mass preconditioning*, *Comput. Phys. Commun.* **174** (2006) 87–98, [hep-lat/0506011].

[146] **APE** Collaboration, M. Albanese *et al.*, *Glueball Masses and String Tension in Lattice QCD*, *Phys. Lett.* **B192** (1987) 163.

[147] A. Hasenfratz and F. Knechtli, *Flavor symmetry and the static potential with hypercubic blocking*, *Phys. Rev.* **D64** (2001) 034504, [hep-lat/0103029].

[148] T. Blum *et al.*, *Improving flavor symmetry in the Kogut-Susskind hadron spectrum*, *Phys. Rev.* **D55** (1997) 1133–1137, [hep-lat/9609036].

[149] **MILC** Collaboration, K. Orginos, D. Toussaint, and R. L. Sugar, *Variants of fattening and flavor symmetry restoration*, *Phys. Rev.* **D60** (1999) 054503, [hep-lat/9903032].

[150] S. Dürr, *Gauge action improvement and smearing*, *Comput. Phys. Commun.* **172** (2005) 163–186, [hep-lat/0409141].

[151] A. Hasenfratz, R. Hoffmann, and S. Schaefer, *Hypercubic Smeared Links for Dynamical Fermions*, *JHEP* **05** (2007) 029, [hep-lat/0702028].

[152] S. Schaefer, A. Hasenfratz, and R. Hoffmann, *Dynamical simulations with HYP-link Wilson fermions*, *PoS* **LAT2007** (2007) 132, [arXiv:0709.4130].

[153] S. Dürr, *Logarithmic link smearing for full QCD*, arXiv:0709.4110.

[154] P. J. Moran, P. O. Bowman, D. B. Leinweber, A. G. Williams, and J. B. Zhang, *Impact of stout-link smearing in lattice fermion actions*, arXiv:0910.2781.

[155] S. Gusken *et al.*, *Nonsinglet axial vector couplings of the baryon octet in lattice QCD*, *Phys. Lett.* **B227** (1989) 266.

[156] C. Best *et al.*, *Pion and rho structure functions from lattice QCD*, *Phys. Rev.* **D56** (1997) 2743–2754, [hep-lat/9703014].

[157] J. Foley *et al.*, *Practical all-to-all propagators for lattice QCD*, *Comput. Phys. Commun.* **172** (2005) 145–162, [hep-lat/0505023].

[158] **Hadron Spectrum** Collaboration, M. Peardon *et al.*, *A novel quark-field creation operator construction for hadronic physics in lattice QCD*, *Phys. Rev.* **D80** (2009) 054506, [arXiv:0905.2160].

[159] J. Bulava, *An Improved Variance Reduction Technique for Stochastic All-to-All Quark Propagators in Lattice QCD Spectrum Computations*. PhD thesis, Mellon College of Science at Carnegie Mellon University, 2009.

[160] R. Barrett *et al.*, *Templates for the Solution of Linear Systems: Building Blocks for Iterative Methods*. SIAM, Philadelphia, 1994.

[161] W. Press, S.A.Teukolsky, W.T.Vetterling, and B.P.Flannery, *Numerical Recipes in C, 2nd Ed.* Cambridge University Press, Cambridge New York, 1999.

[162] A. Stathopoulos and K. Orginos, *Computing and deflating eigenvalues while solving multiple right hand side linear systems in Quantum Chromodynamics*, arXiv:0707.0131.

[163] M. Lüscher, *Local coherence and deflation of the low quark modes in lattice QCD*, *JHEP* **07** (2007) 081, [arXiv:0706.2298].

[164] **UKQCD** Collaboration, P. Lacock, C. Michael, P. Boyle, and P. Rowland, *Orbitally excited and hybrid mesons from the lattice*, *Phys. Rev.* **D54** (1996) 6997–7009, [hep-lat/9605025].

[165] X. Liao and T. Manke, *Excited charmonium spectrum from anisotropic lattices*, hep-lat/0210030.

[166] S. Basak *et al.*, *Group-theoretical construction of extended baryon operators in lattice QCD*, *Phys. Rev.* **D72** (2005) 094506, [hep-lat/0506029].

[167] R. G. Petry, D. Harnett, R. Lewis, and R. M. Woloshyn, *Exploring the meson spectrum with twisted mass lattice QCD*, *Phys. Rev.* **D78** (2008) 074502, [arXiv:0803.4141].

[168] S. Prelovsek *et al.*, *Spectroscopy of light tetraquark states*, *PoS* **LAT2009** (2009) 103, [arXiv:0910.2749].

[169] H.-X. Chen, V. Dmitrasinovic, A. Hosaka, K. Nagata, and S.-L. Zhu, *Chiral Properties of Baryon Fields with Flavor SU(3) Symmetry*, *Phys. Rev.* **D78** (2008) 054021, [arXiv:0806.1997].

[170] K. Nagata, A. Hosaka, and V. Dmitrasinovic, *Chiral properties of baryon interpolating fields*, *Eur. Phys. J.* **C57** (2008) 557–567.

[171] L. Okun, *Leptons and quarks*. Elsevier Science Ltd, 1982.

[172] D. Lurié, *Particles and Fields*. Interscience Publishers, 1968.

[173] M. Lüscher, *Volume Dependence of the Energy Spectrum in Massive Quantum Field Theories. 1. Stable Particle States*, *Commun. Math. Phys.* **104** (1986) 177.

[174] S. Ciulli, C. Pomponiu, and I. Sabba-Stefanescu, *Analytic Extrapolation Techniques and Stability Problems in Dispersion Relation Theory*, . Presented at 14th Internationale Universitatswochen fur Kernphysik, Schladming, Austria, Feb 24 - Mar 7, 1975.

[175] Y. Chen, S.-J. Dong, T. Draper, I. Horvath, K.-F. Liu, N. Mathur, S. Tamhankar, C. Srinivasan, F. X. Lee, and J. Zhang, *The sequential empirical bayes method: An adaptive constrained-curve fitting algorithm for lattice qcd*, hep-lat/0405001.

[176] G. P. Lepage *et al.*, *Constrained curve fitting*, *Nucl. Phys. Proc. Suppl.* **106** (2002) 12–20, [hep-lat/0110175].

[177] K. G. Wilson, *Talk at the abingdon meeting on lattice gauge theories*, .

[178] B. Blossier, M. Della Morte, G. von Hippel, T. Mendes, and R. Sommer, *On the generalized eigenvalue method for energies and matrix elements in lattice field theory*, *JHEP* **04** (2009) 094, [arXiv:0902.1265].

[179] L. Y. Glozman, C. B. Lang, and M. Limmer, *Angular momentum content of the rho-meson in lattice QCD*, *Phys. Rev. Lett.* **103** (2009) 121601, [arXiv:0905.0811].

[180] L. Y. Glozman, C. B. Lang, and M. Limmer, *The chiral and angular momentum content of the rho- meson*, *Few Body Syst.* **47** (2010) 91–103, [arXiv:0909.2939].

[181] G. Colangelo, S. Dürr, and C. Haefeli, *Finite volume effects for meson masses and decay constants*, *Nucl. Phys.* **B721** (2005) 136–174, [hep-lat/0503014].

[182] G. Colangelo, A. Fuhrer, and C. Haefeli, *The pion and proton mass in finite volume*, *Nucl. Phys. Proc. Suppl.* **153** (2006) 41–48, [hep-lat/0512002].

[183] H. Wittig, *Low-energy particle physics and chiral extrapolations*, arXiv:1201.4774.

[184] E. Oset, M. Döring, U. G. Meissner, and A. Rusetsky, *Chiral unitary theory of scalar mesons in a finite volume*, arXiv:1108.3923.

[185] A. M. Torres, L. R. Dai, C. Koren, D. Jido, and E. Oset, *The KD, ηD_s interaction in finite volume and the $D_{s^*0}(2317)$ resonance*, arXiv:1109.0396.

[186] A. Martinez Torres, M. Bayar, D. Jido, and E. Oset, *Strategy to find the two $\Lambda(1405)$ states from lattice QCD simulations*, arXiv:1202.4297.

[187] A. Walker-Loud, *Evidence for non-analytic light quark mass dependence in the baryon spectrum*, arXiv:1112.2658.

[188] S. Weinberg, *The Quantum theory of fields. Vol. 1: Foundations*, . Cambridge, UK: Univ. Pr. (1995) 609 p.

[189] G. Breit and E. Wigner, *Capture of Slow Neutrons*, *Phys. Rev.* **49** (1936) 519–531.

[190] N. Mathur *et al.*, *Scalar mesons a0(1450) and sigma(600) from lattice QCD*, *Phys. Rev.* **D76** (2007) 114505, [hep-ph/0607110].

[191] S. Prelovsek and D. Mohler, *A lattice study of light scalar tetraquarks*, *Phys. Rev.* **D79** (2009) 014503, [arXiv:0810.1759].

[192] D. C. Moore and G. T. Fleming, *Multiparticle states and the hadron spectrum on the lattice*, *Phys. Rev.* **D74** (2006) 054504, [hep-lat/0607004].

[193] J. Bulava, K. J. Juge, C. J. Morningstar, M. J. Peardon, and C. H. Wong, *Two-particle Correlation Functions with Distilled Propagators*, *PoS* **LAT2009** (2009) 097, [arXiv:0911.2044].

[194] G. Bali and C. Ehmann, *Mixing of S-Wave Charmonia with $\mathrm{D}\overline{\mathrm{D}}$ Molecule States*, *PoS* **LAT2009** (2009) 113, [arXiv:0911.1238].

[195] S. Prelovsek *et al.*, *Lattice study of light scalar tetraquarks with I=0,2,1/2,3/2: are sigma and kappa tetraquarks?*, *Phys. Rev.* **D82** (2010) 094507, [arXiv:1005.0948].

[196] L. Del Debbio, L. Giusti, M. Lüscher, R. Petronzio, and N. Tantalo, *Stability of lattice QCD simulations and the thermodynamic limit*, *JHEP* **02** (2006) 011, [hep-lat/0512021].

[197] R. Sommer, *A New way to set the energy scale in lattice gauge theories and its applications to the static force and alpha-s in SU(2) Yang-Mills theory*, *Nucl. Phys.* **B411** (1994) 839–854, [hep-lat/9310022].

[198] S. Dürr *et al.*, *Ab-Initio Determination of Light Hadron Masses*, *Science* **322** (2008) 1224–1227, [arXiv:0906.3599].

[199] P. Huber, *Renormalization factors of quark bilinears using the DCI operator with dynamical quarks*, *JHEP* **11** (2010) 107, [arXiv:1003.3496].

[200] T. Maurer, *The QPACE Supercomputer and Restauration of Chiral Symmetry in Excited Baryons.* PhD thesis, University of Regensburg, Germany, 2011.

[201] J. Gasser and H. Leutwyler, *Chiral Perturbation Theory to One Loop*, *Ann. Phys.* **158** (1984) 142.

[202] G. Colangelo, J. Gasser, and H. Leutwyler, *pi pi scattering*, *Nucl. Phys.* **B603** (2001) 125–179, [hep-ph/0103088].

[203] J. Bijnens, *Quark Mass dependence at Two Loops for Meson Properties*, *PoS* **LAT2007** (2007) 004, [arXiv:0708.1377].

[204] N. Isgur and G. Karl, *Hyperfine Interactions in Negative Parity Baryons*, *Phys.Lett.* **B72** (1977) 109.

[205] N. Isgur and G. Karl, *Positive Parity Excited Baryons in a Quark Model with Hyperfine Interactions*, *Phys.Rev.* **D19** (1979) 2653.

[206] T. Melde, W. Plessas, and B. Sengl, *Quark-Model Identification of Baryon Ground and Resonant States*, *Phys.Rev.* **D77** (2008) 114002, [arXiv:0806.1454].

[207] B. J. Menadue, W. Kamleh, D. B. Leinweber, and M. S. Mahbub, *Isolating the Lambda(1405) in Lattice QCD*, *Phys. Rev. Lett.* **108** (2012) 112001, [arXiv:1109.6716].

Danksagung

An dieser Stelle möchte ich mich ganz herzlich bei allen Personen bedanken, die in irgendeiner Weise an der Erstellung meiner Dissertation beteiligt waren.
Als Erster sei mein Betreuer Christian B. Lang hervorgehoben, der mir mit seiner langjährigen Erfahrung immer zur Seite stand und mir zugleich den Freiraum gab, mich zu einem selbstständigem Forscher zu entwickeln. Ein herzlicher Dank auch an meine Kollegen Markus Limmer und Daniel Mohler, die Arbeit mit Euch wird mir immer wohl in Erinnerung bleiben! Besonderer Dank gebührt Andreas Schäfer, der mir für über drei Jahre eine Finanzierung aus dem Projekt SFB-TR55 ermöglichte.
Special thanks go to Sasa Prelovsek for giving me the honor of joining my PhD committee. Besonderer Dank auch an Stefan Schaefer, der in der Zeit meiner Dissertation bereitwillig ein neues Projekt mit mir begann und mich zur Humboldt-Universität zu Berlin einlud.
Ich freue mich und bedanke mich dafür, Mitglied der Gittergruppe der Universität Graz gewesen sein zu dürfen, welche sich insbesondere durch weitreichende Expertise und eine familiäre Atmosphäre auszeichnet. Sincere thanks also go to my officemates Julia Danzer, Selym Villalba-Chavez, Helios Sanchis-Alepuz and Valentina Verduci. I will definitely miss to talk to you during working day!
Furthermore, I would like to thank all collegues working in Mozartgasse, all members of the Doktoratskolleg and all other members of the Fachbereich Theoretische Physik at Institut für Physik, Universität Graz. I could not imagine a better environment for the period of my PhD study.
Ein besonders herzliches Dankeschön geht an meine guten Freunde Beate, Gernot, Holger, Paul und Vid. Unsere Band ist ein Teil von mir und wird es immer bleiben.
Von ganzem Herzen bedanke ich mich bei meinen Eltern, Erika und Günter. Eure Unterstützung war und ist mir in jeglicher Hinsicht immer von großer Bedeutung!
Der größte Dank geht an meine liebe Frau Anna, der ich meine Dissertation widmen möchte. Ohne Dein Verständnis und Deine Unterstützung wäre diese Arbeit nicht möglich gewesen. Auch möchte mich für die wundervolle Zeit bedanken, die mir von Dir und unseren Kindern geschenkt wurde!